Technische Universität München
TUM School of Medicine and Health

RIPK3 acts tumor suppressive in lung adenocarcinoma by restructuring the tumor immune microenvironment and offers a new chemotherapeutic target

Fabian J. K. Allmendinger

Vollständiger Abdruck der von der TUM School of Medicine and Health der Technischen Universität München zur Erlangung eines

Doktors der Medizin (Dr. med.)

genehmigten Dissertation.

Vorsitz: apl. Prof. Dr. Bernhard Haslinger

Prüfende der Dissertation:

1. apl. Prof. Dr. Philipp J. Jost
2. Priv.-Doz. Dr. Dirk Wohlleber

Die Dissertation wurde am 04.12.2023 bei der Technischen Universität München eingereicht und durch die TUM School of Medicine and Health am 05.06.2024 angenommen.

This dissertation was kindly supported by the Mildred Scheel Program of the German Cancer Aid.

Index

Figures

Tables

1 Introduction

1.1 Lung cancer

Lung cancer is the leading killer regarding cancer-related mortality, which demands for improvement in therapeutic strategies. In the last decades efforts of renewing therapy approaches did not yet overcome the high lung cancer death rates of the last years. Increasing efforts in understanding the aberrational landscape of oncogenic transformed lung cells revealed targetable tumor driving mutations and repressed cell death cascades to preserve tumor surveillance during outgrowth. This improvement in the understanding of lung cancer biology opened the door for efficient personalized medicine. The following doctoral thesis aims to show that receptor-interacting serine/threonine-protein kinase 3 (RIPK3) dependent necroptosis is an immunogenic, tumor suppressive cell death pathway in lung adenocarcinoma (LUAD), which further can be activated by the chemotherapeutics Paclitaxel and Pemetrexed. The role of RIPK3 in LUAD was investigated *in silico* with human lung cancer databases, *in vivo* with two LUAD mouse models and *in vitro* with human LUAD cell lines.

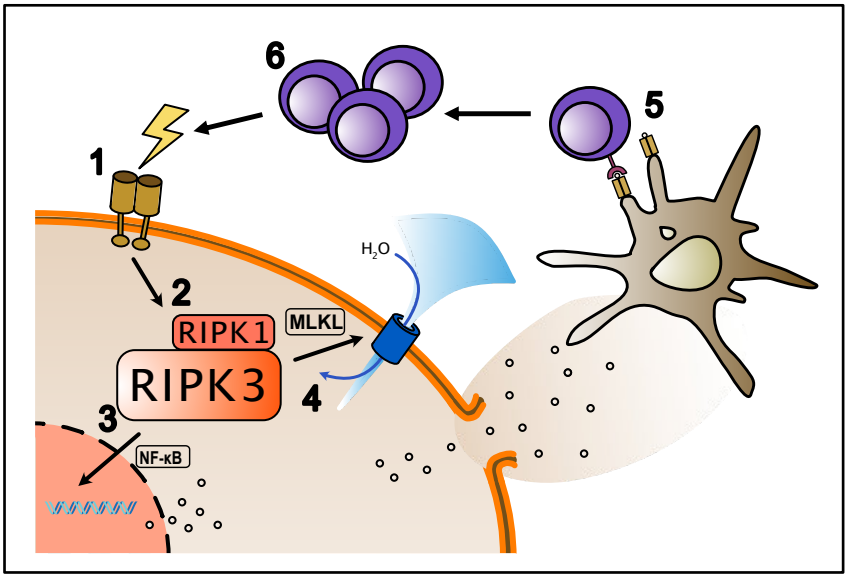

Figure 1: Necroptosis in cancer. 1: Necroptosis induction by cell death receptors, 2: Necrosome formation, 3: NF-κB induced cytokine production, 4: MLKL mediated transmembrane pore formation, hydrogen influx and membrane rupture, 5: Antigen-presenting cells prime effector immune cells to released tumor antigens, 6: Antitumoral immune reaction mediated by effector immune cells against tumor cells

1.1.1 Epidemiology

Global studies outline that lung cancer leads the cancer-related death rates both in men and women. Additionally, out of all cancer entities, lung cancer is associated with the highest incidence and prevalence rates in the world (Ferlay et al., 2019; Ferlay et al., 2015; Siegel et al., 2020; The, 2018). Whereas new treatment and cancer-screening strategies have decreased

mortality rates in various types of cancer (e.g., breast cancer, prostatic cancer), in lung cancer new therapy regimes and screening approaches did not have similar effects on mortality rates. The worse prognosis of patient survival underlines the need of improvement in the biological understanding of lung cancer to moreover invent effective therapy strategies. According to a prospective study of the American Association for Cancer Research, lung cancer will keep the lead of cancer related mortality for at least 10 more years int the United States of America (Rahib et al., 2014).

1.1.2 Histopathology

Lung tumors include a broad spectrum of different cancer types, which differ in their oncogenic profiles and histological characteristics. Today's understanding on lung cancer tumorigenesis, cells of origin, molecular landscape and the implementation of different treatment regimens are largely based on the pathologic classification of lung cancer further summarized in the following section.

The histologic classification of lung cancer is primarily divided into small-cell or oat cell lung cancer (SCLC) and non-small-cell lung cancer (NSCLC) according to the size and appearance of the microscopic tumor cells (Travis, Brambilla, Burke, et al., 2015; Travis, Brambilla, Nicholson, et al., 2015). Key criteria for pathologic diagnosis of lung cancer were determined in the 2015 World Health Organization Classification of Lung tumors (Travis, Brambilla, Nicholson, et al., 2015). SCLC shows aggressive growth patterns, metastasizes early, and gains neuroendocrine functions.

NSCLCs represent about 85% of lung cancer cases and are defined by large dysmorphic tumor cells, which either have adenomatous, squamous or unspecific characteristics. According to the tumor cell pathology NSCLCs are further subdivided into lung squamous cell carcinoma (LUSC), large cell carcinoma (LCC), and lung adenocarcinoma (LUAD).

Between 25% to 30% of lung cancer is diagnosed as LUSC (Lewis et al., 2014). LUSC cells extensively produce keratin filaments causing the main histologic characteristics such as keratin pearls and intercellular bridging (Kadota et al., 2015; Kadota et al., 2014).

LCC represents 5% of lung cancer cases and is diagnosed if the histomorphology and immunohistochemistry (IHC)-staining excludes the diagnosis of LUAD, LUSC or neuroendocrine tumors. LCC forms sheet- or nest-like lesions and the cancer cells appear enlarged and polygonal (Lewis et al., 2014).

LUAD is the most common type of lung cancer with a proportion of 30% of all lung cancer cases and 40% of NSCLCs (Lewis et al., 2014). The incidence of LUAD has risen over the last decades and thereby has determined the global trend of increasing lung cancer cases (Devesa et al., 2005; Ferlay et al., 2019). LUAD originates from lung epithelial cells mainly alveolar type 2 cells (Desai

et al., 2014; Kim et al., 2005; Mainardi et al., 2014), which transform to dysplastic adenomatous cells with glandular features during epithelial neoplasia. As a main histopathologic characteristic, these cells are filled with mucin, which is exocytotic secreted or accumulates in the cytosol. Invasive LUAD lesions show different growth patterns, which determine the grading of the tumor lesion. These patterns are classified as glandular/acinar, papillary/micropapillary, solid or lepidic. To confirm LUAD tumors in poorly differentiated lesions or biopsies, immunohistochemical staining for LUAD marker proteins is applied in diagnostic routine. 85% of LUAD express thyroid transcription factor 1 and napsin A (Mukhopadhyay & Katzenstein, 2011; Rekhtman et al., 2011; Tacha et al., 2012), which are both used to discriminate LUAD from LUSC. The availability of personalized target therapies in advanced stage lung cancer have made IHC and genome sequencing essential in the diagnostic process and have improved the patient outcome. Nowadays, the genotype-based classifications are leading the way to patient-individualized therapies.

1.1.3 The biology of lung adenocarcinoma

According to basic cancer principles, the biology of lung adenocarcinoma relies on heterogeneous genomic and epigenomic alterations predominantly occurring in defined groups of genes which promote tumorigenesis by (i) maintaining growth signals (oncogenes) as wells as (ii) resisting cell cycle stops or cell death (tumor suppressor genes).

In the respiratory airway system lung epithelial cells and pneumocytes are continuously exposed to the exogenic environment containing mutagenic substances such as air pollution or cigarette smoke. Vulnerable bronchial cells accumulate various alterations in different genes and by chance in critical oncogenes and tumor suppressor genes. The analysis of randomly appearing alterations in LUAD genomes elucidated an overall heterogenous mutational pattern despite for alterations frequently appearing in the same genes with tumor driving functions. These distinct genes are seen as LUAD defining oncogenes or tumor suppressor genes (Ding et al., 2008; Jamal-Hanjani et al., 2017). LUAD related oncogenes mediate growth pathways, which are critical for the malignant transformation of precursor lung epithelial cells. In general, growth signaling cascades consist of receptors, mediating and executing proteins, which can all transform to oncogenes if changes sustain the activated form.

Frequently mutated growth receptors in LUAD involve the epidermal growth factor receptor family including epidermal growth factor receptor 1-3 (EGFR 1-3) and human epidermal growth factor receptor 2 (HER2). EGFR 1-3 and HER2 are transmembrane receptor proteins with intracellular kinase domains (Receptor tyrosine kinases – RTKs) and extracellular binding pockets for receptor specific growth factors. Activated receptors dimerize and thereby juxtapose the intracellular receptor segments to activate their kinase domains by trans-phosphorylation of

tyrosine rich oligomerized segments. Subsequently adapter proteins recognize phosphorylated receptor regions and activate downstream growth signaling pathways. For the tyrosine phosphorylation RTKs use adenosine triphosphates (ATP) as phospho-group donors. Gain of function mutations during oncogenic transformation affect the coding sequence of the ATP binding pocket in the RTK genes (exon 18-21). This results in an increase of the enzymatic phosphorylation activity and thus continuous initiation of cell proliferation (Marchetti et al., 2005; Red Brewer et al., 2013; Wang et al., 2011; Yun et al., 2007). The same principle can be found in additional mutated RTK genes often occurring in LUAD such as: Ret proto-oncogene (RET), Met proto-oncogene (MET), anaplastic lymphoma kinase (ALK), and reactive oxygen species proto-oncogene 1 (ROS1).

Despite receptors, oncogenic tumor driver mutations involve pathway proteins, which mediate the process of cell growth signaling. The most common oncogene of this group is the Kristen rat sarcoma (KRAS), which is frequently mutated in LUAD and transcribes for a group of the guanine nucleotide binding proteins (G-proteins). The KRAS protein has an enzymatic guanin triphosphatase (GTPase) domain, which dephosphorylates guanine triphosphate (GTP) to terminate transduced growth signals. KRAS is bound to the inner side of the cell membrane due to posttranslational addition of lipidic anker chains facilitating its interaction with membrane located growth receptors, like EGFR. The KRAS scaffold has two different conformations stabilized by the co-factor guanine tri- or biphosphate (GTP, GDP). The active KRAS-GTP conformation promotes, while the inactive KRAS-GDP conformation inhibits, downstream growth signaling. Autophosphorylation of RTKs recruit different adapter proteins, some of which can function as guanin nucleotide exchange factors (GEFs), therefore releasing GDP from the inactive KRAS-GDP complex. Subsequently, KRAS binds intracellular GTP for self-activation. The KRAS-GTP complex may interact with different downstream effector proteins such as: Raf kinase, phosphophatidylinositol 3-kinase (PI3K) and Ral guanine nucleotide dissociation stimulator (RALGDS). Nascent protein complexes determine the activation of several downstream signaling pathways like mitogen activated protein kinase cascade (MAP kinase cascade) (Fetics et al., 2015). These pathways control cell proliferation, motility, and survival. Inactivation of KRAS-GTP dependent growth signal relies on the KRAS-GTPase activity cleaving GTP to GDP. GTPase-activating proteins (GAPs) initiate the KRAS-GTPase and promote the GDP-KRAS confirmation, decreasing cell proliferation (Scheffzek et al., 1997). Mutations of KRAS as found in LUAD genomes affect the enzymatic domain and impairs the GTPase function. Without the GTPase activity the KRAS-GTP complex is trapped in its active form and cannot be transformed to the inactive KRAS-GDP complex, which results in a sustained growth signal. Mutations in the KRAS gene are mainly missense mutations in the GTPase coding exon 12 or 13. The mutating event induces a nucleotide transition from guanine (G) to adenosine (A) or transversion of guanine to thymine (T), which leads to a substitution of the amino acid on

position 12 or 13, most common glycine to cysteine (G12C), glycine to valine (G12V) or glycine to aspartate (G12D, G13D). Loss of glycine alters the conformation of the GTPase domain, inhibiting its enzymatic activity and thus eliciting an active KRAS-GTP conformation (Vatansever et al., 2020). These oncogenic transformations are responsible for persistently increased cell proliferation and are essential in the tumor formation of LUAD.

Nevertheless, hyperproliferating and dysplastic cells may prevent carcinogenesis by preserved rescue mechanisms activating tumor suppressors, which in case of critical genomic aberrations inhibit the cell cycle or induce cell death. To overcome rescue mechanisms frequently occurring additional mutations in the LUAD genome affect tumor suppressor genes, which are defined as second hit mutations. These second mutations prevent the oncogenic shutdown by proliferation blocks and aid to continue tumorigenesis.

The most prominent tumor suppressor is the tumor protein P53 (TP53). Mutations in TP53 are key targets in lung cancer especially SCLC, LUSC and LUAD. TP53 is a transcription factor activated in cell imperiling stress situations, such as metabolic dysfunction, DNA damage and oncogene expression, in which it guards genomic stability by regulating cell cycle arrest, senescence or cell death. To prevent tumorigenesis the TP53 protein structure contains a DNA binding domain, which interacts with specific promoter, enhancer, and silencer regions to regulate the transcription of proteins critically required to maintain an active cell cycle, mitosis or inhibit the prosecution of apoptotic cell death. To continuously control the cellular stability TP53 is permanently expressed, and its state of activation regulated by polyubiquitylation and phosphorylation. The main regulator of TP53 is the E3 ubiquitin protein ligase human double minute 2 homolog (HDM2), which ubiquitylates TP53 to maintain the inactive form further degraded by the proteasome. If DNA alterations accumulate and threaten the cellular integrity TP53-modifying-kinases like ataxia telangiectasia mutated (ATM), ataxia telangiectasia related (ATR), or checkpoint kinase 1 and 2 (CHK1, 2) recognize the DNA damage signature and prevent TP53 degradation by hyperphosphorylation. Phosphorylated TP53 stabilizes a protein scaffold conformation, which exposes a DNA binding motif and interacts with TP53-respond-elements to promote the expression of tumor suppressive effectors (proteins and regulatory RNAs). The expression of these proteins inhibits the cell cycle, repairs DNA damages, induces apoptosis in hypermutated cells or leads to cellular senescence. Taken together TP53 can prevent early tumorigenesis and is therefore often turned off by loss of function mutations in lung cancer.

Further mutated tumor suppressors in LUAD are: (i) kelch-like ECH-associated protein 1 (KEAP1) depressing cell proliferation by increasing oxidative stress; (ii) liver kinase B1 (LKB1) regulating cellular metabolism and decreasing cell proliferation in absence of energy sources like ATP; (iii) neurofibromin 1 (NF1) interacting and inhibiting KRAS.

The understanding of frequent genomic changes leading to oncogenic transformation in lung epithelial cells has been of emerging importance as it has led the way to tumor specific therapeutic approaches. Nowadays, oncogenic mutations in LUAD can be targeted by various inhibitory drugs to overcome the continuously activated proliferation signal for example by blocking the ATP binding pocket of RTKs. Additionally, identifying LUAD patients carrying these critical oncogenic mutations may increase the overall survival by more precisely stopping carcinogenesis in advanced disease (Janne et al., 2015; Maemondo et al., 2010; Mitsudomi et al., 2010; Mok et al., 2009; Rosell et al., 2012; Sequist et al., 2013; Soria et al., 2018; Zhou et al., 2011). Nevertheless, the LUAD biology is far more complex than in our todays understanding and therefore more tumor driving aberrations must be identified as we present in this doctoral thesis.

1.1.4 Clinical aspects of LUAD

Patients diagnosed with lung cancer often present with nonspecific symptoms such as dyspnea or cough, which prolongs clinical admission and diagnostic procedures leading to a dominating fraction of advanced diseases. Clinical staging of NSCLC complies to the TNM and UICC8 guidelines (Goldstraw et al., 2016) considering primary tumor size, location, tumor metastases in regional and distant lymph nodes identified by radiographic screening mostly X-ray chest and CT scan. Additionally, the histopathology of lung tumors is determined by bronchial or transthoracic biopsies. Whereas early disease of NSCLC in a non-metastatic or regional metastatic situation is treated in a curative intend by surgical elimination of the tumor burden, advanced diseases with distant metastases are restricted to palliative radio-/chemotherapy or on target therapeutics. Chemotherapeutic regimens for advanced diseases rely on Cisplatin or Carboplatin as mono- or dual regimen accommodated by Paclitaxel, Docetaxel, Gemcitabine, Pemetrexed or Vinorelbine (Postmus et al., 2017).

1.2 Mouse models for lung adenocarcinoma

1.2.1 Mouse models

To advance in the understanding of cancer biology, different research models have emerged in the field of basic science to allow *ex human* investigations still close to human-like conditions. The biology of cancer cells is often studied in human cell lines (*in vitro*). However, the complex multistep progress of tumorigenesis needs the pathophysiological context of a model organism mimicking human tissue conditions. For this reason, the most used model for studying tumor initiation and progression is the mouse (*mus musculus*). Mice share essential phylogenetic characteristics with human, such as mammalian anatomy, physiology and 80% homology with human genome (Mouse Genome Sequencing et al., 2002). Moreover, keeping mice is cost and space effective, scientific procedures are standardized, and the short life cycle of mice accelerate the observation time of results.

1.2.2 Genetic engineered LUAD mouse models

LUAD genetic engineered mouse models (GEMMs) are designed to precisely develop LUAD tumors due to the implementation of critical driving mutations identified by depicting the human LUAD biology further translated into the mouse genome. In principle, various alterations in LUAD generate a heterogenous genomic pattern in individual tumor cells. These invariant changes rely on the random mechanism of emerging mutations. For example, tobacco smoke is well known for inducing several different mutations in lung epithelial cells. As a result of sampling, sequencing, and comparing mutation patterns of a cohort of LUAD patients the overall tumor aberrational burden revealed a few but frequently occurring genetic alterations in tumor driving signaling pathways (oncogenes, tumor suppressor genes; see chapter 1.1.3). This knowledge of observed LUAD defining genes is then transferred to modify ortholog genes in the mouse genome leading the way to LUAD specific GEMMs with histopathological and genetic features like the ones observed in human cancer. Furthermore, because of similar genomic backgrounds GEMMs yield deep insight into LUAD tumorigenesis, the impact of defined genomic changes as well as therapy options and therapy resistance.

A majority of human LUAD accumulates Ras-gain of function mutations resulting in Ras-driven tumor signatures, which are maintained in mice by focusing on *Kras* based genetic backgrounds of GEMMs (Guerra et al., 2003; Jackson et al., 2001). Thereby, a frequently inserted transgene in the mouse genome relies on $Kras^{G12D}$ gain of function mutation. The induction of $Kras^{G12D}$ provides a strong oncogenic driver resulting in LUAD tumors if activated in lung epithelial cells and was therefore used in this doctoral thesis.

Further modified genes in LUAD-GEMMs are tumor suppressors which are frequently mutated in the human genomic background and therefore implemented into GEMMs to induce LUAD tumors such as *p53* (see chapter 1.1.3). Common utilized GEMMs for pre-clinical analysis and their genetic backgrounds are reviewed and summarized by Kwon et. al. (Kwon & Berns, 2013).

1.3 Tumor microenvironment (TME)

Tumorigenesis not only depends on tumor driving genomic changes, but also on surrounding environmental impacts of the tumor harboring tissue. Both tumor cells and bystander normal cells adopt to oncogenic transformation in the TME, which decrease environmental stress factors like nutritional deprivation and invading immune cells subsequently ensuring tumor survival. Hence, LUAD cells reprogram normal cells to favor tumor outgrowth instead of preventing lung dysplasia. Therefore, they paracrine secrete cytokines or regulatory proteins, which restructure TME-forming cells such as (i) tissue fibroblasts, which form tumor isolating boundaries (W. J. Chen et al., 2014), (ii) the extracellular matrix, which is disintegrated to make room for tumor proliferation (Navab et al., 2016), (iii) endothelial cells to increase angiogenesis, which ensures

the required nutritional supply (Dimitrova et al., 2016; McClelland et al., 2007; Xie et al., 2012), or (iv) resident and invading immune cells to prevent antitumoral immune response, which we focused on in this doctoral thesis due to the immunogenic function of the investigated cell death pathway (necroptosis, see chapter 1.5). All these processes in the tumor environment are critical to form a tumor niche in the lung and sustain tumor growth.

1.4 The immunology of LUAD

The immune system takes an important preventive role in controlling malignant transformation by suppressing tumorigenesis after recognizing cancer cells as foreign and inducing cell death. Immune defense mechanisms as described for the TIME inhibit cancer dissemination and proliferation to maintain a functional tissue network. In contrast to the anti-tumoral role of the immune system, cancer entities like LUAD tumors escape immune response and moreover recruit tumor promoting immune cells in the TIME to preserve tumorigenesis. Thus, finding ways to re-activate antitumoral immune cells in LUAD lesions may be of further interest to reduce LUAD tumorigenesis.

1.4.1 Tumor immune microenvironment (TIME)

Oncogenic transformation of normal cells to tumor cells processes with substantial changes in the genetic background due to mutations or changes in gene expression, which impacts the proteome and therewith proteins presented at the cell membrane. These changes are sensed by neighboring resident cells or invading immune cells, which prevent tumor formation by eliminating malignant cells. Hence, the lung immune microenvironment is a tissue securing instance inhibiting tumorigenesis in the normal lung. LUAD cells have a high tumor mutational burden, which accumulates tumor associated antigens recognized by immune cells. It is therefore critical during tumorigenesis to inhibit antitumoral immune responses. The antitumoral immune reaction is mediated by lung resident immune cells primarily by antigen presenting cells (APCs) such as macrophages and dendritic cells. APCs identify transformed cells by their associated, foreign-appearing antigens and transcriptomic changes and subsequently activate effector immune cells (T-cells and B-cells), which clear dysplastic cells from the normal lung tissue. LUAD cells escape the anti-tumoral immune system by establishing a pro-tumoral immune microenvironment, which blocks immune responses at different instances of the immune cascade: (i) Cytokines secreted by tumor cells or pro-tumoral immune cells inhibit immune cell invasion (Freeman et al., 2014), (ii) tumor cells decrease tumor-associated antigen (TAA) expression at the cell membrane or released during necrotic cell death (Karanikas et al., 2008), (iii) increased numbers of regulatory immune cells in the TIME inhibit the activation of anti-tumoral immune response and (Moatti et al., 2022) (iv) expression of immune cell-blocking proteins (PD1) reduce the activity of effector immune cells (Moatti et al., 2022).

Taken together LUAD tumorigenesis depends on inhibiting the immune system by shaping a tumor promoting immune microenvironment.

1.4.2 Tumor-suppressive immune response

The initiation of anti-tumoral immune response is triggered by tumor antigens especially the oncogenic pattern of cell surface antigens, which differ from normal cells and appear foreign to antigen recognizing immune cells. Tumor antigens result from changes in the transcriptome during tumorigenesis (TAAs) and induced mutations in gene coding regions found in cancer entities with high tumor mutational burden such as LUAD (Tumor specific antigens: TSAs). Hence, tumor antigens are diverse and either (i) non-mutated proteins, which are weakly- or not expressed in normal resident tissue cells (TAAs) or (ii) mutated proteins, which change their scaffold due to the genomic instability further exposing foreign epitopes recognized by the immune system (TSAs).

Moreover, tumor cell debris from non-viable tumor cells release damage associated molecular patterns (DAMPs) and cytosolic tumor antigens, which are highly immunogenic and recruit immune cells into the TIME to clear dead cell remnants. DAMPs are defined as intracellular and immunogenic substances normally isolated from the ECM by the plasma membrane (e.g., DNA, RNA, ATP, mitochondrial DNA, heat shock proteins, cardiolipin). Arising tumor lesions suffer from internal and external stress factors forcing tumor cells to cell death such as (i) lack of energy sources, (ii) production of radical oxygen species and (iii) ATP deficiency and thereby reduced function of transmembrane ion pumps, which maintain osmotic homeostasis.

Taken together, stress factors exposed to non-resistant tumor cells lead to cell death and subsequently the release of intracellular components (DAMPs) attracting immune cells and trigger inflammation.

Before the execution of anti-tumoral immune reactions, primary innate immune cells screen for malignant cells in the resident tissue and in case secrete interleukin-12/interferon-γ to stop cell proliferation or further activate regulated cell death cascades. Tissue associated phagocytes like tumor associated macrophages (TAMs) ingest and degrade dead cell remnants in phagolysosomes via endocytosis. Cleaved protein segments including tumor antigens get attached to cell surface receptors (Major Histocompatibility Complexes: MHCs) and presented to adaptive immune cells. These antigen presenting cells (APCs) are part of the innate immune system and consist of TAMs and dendritic cells (DCs). Tumor suppressive TAMs recruit and activate tissue infiltrating T-cells by chemokines, cytokines and presenting MHC bound tumor antigens, whereas DCs migrate into regional lymph nodes to activate naive B- and T-cells.

The adaptive immune system contains antibody producing B-cells and T-cells, which either regulate the immune system (Tregs), degrade tumor cells (CD-8^+ cytotoxic T-cells) or co-activate

B-cells, TAMs or CD-8^+ cytotoxic T-cells by antigen presentation (APC, T-helper cells). B-cells and T-cells express specific receptors, which bind to epitopes of cell surface proteins either directly present on target cells on MHC1 complexes or exposed on MHC2 complexes expressed by APCs. After the immune cell receptor recognizes an epitope, further co-stimulatory signals determine if the effector immune cell (T-cell or B-cell) gets activated or remains inactivated. Innate immune cells, which initiate the anti-tumoral immune response may provide activating signals, whereas the tumor environment and tumor cells often harbor inhibitory signals. In case stimulatory signals outweigh inhibitory signals, activated B-cells produce tumor specific antibodies, which bind to the antigen carrying cells and subsequently degrade these cells via the complement system or antibody mediated phagocytosis. Activated cytotoxic T-cells (CD8+-T-cells, γδ-T-cells) recognize MHC bound tumor antigens on tumor cell surfaces and if co-activated release cytotoxic enzymes (granzyme, perforin), which perforate the tumor cell membrane and degrades intracellular proteins. Additionally, T-cells induce tumor cell death by the expression of Fas-receptor ligands (FasL).

Taken together, antitumoral immune responses are a complex interplay of different immune cell subpopulations summarized as immune cells, which detect tumor cells and regulate the immune response (TAMs, DCs) and effector immune cells, which degrade tumor cells. Both groups are critically required to establish an antitumoral immune reaction.

1.4.3 Tumor immune escape

During tumorigenesis outgrowing tumor cells are forced to accumulate mechanisms, which bypass anti-tumoral immune responses, to survive. The adaption to the immune system is promoted by alterations (mutations and epigenetic changes), which block immune cells (e.g., by expression of receptors or cytokines) and decrease their activity. Those critical alterations enforce immune resistant tumor cells, whereas non-immune resistant tumor cells are cleared and thereby generate a cancer tolerating TIME.

Observed immune escape mechanisms in LUAD frequently rely on (i) decreasing tumor antigen expression for not being detected as malignant cells, (ii) direct or indirect inhibition of anti-tumoral effector cells by either the expression of immune blocking receptors or cytokines such as interleukin 10, -1β, - 6, -8, tumor growth factor β and CC motif chemokine ligand 2, -3 and (iii) recruitment of tumor promoting/ regulatory immune cells, which inhibit immune cell invasion and antitumoral response. Important tumor promoting immune cells, which enrich in the LUAD TIME are (i) tumor associated macrophages not acting as antigen presenting cells but moreover expressing immune blocking receptors, enhancing angiogenesis and metastasis (M2-phenotype) as well as (ii) regulatory T-cells and (iii) myeloid derived suppressor cell (MDSC), which both interrupt antitumoral immune reactions by secreting inhibitory cytokines e.g. arginase,

indoleamine 2,3-dioxygenase (IDO), tumor growth factor beta (TGF beta), interleukin 6 and 10 (IL6, 10) or diminishing co-stimulatory signals of anti-tumoral APCs to block the adaptive immune system (effector cells, T-/B-cells).

Normally, APCs bind to matching T- and B-cell receptors with the antigen carrying MHC complexes, subsequently activating effector cells by co-stimulatory signals (immune check point) such as T-lymphocyte activation antigen CD80 and B-lymphocyte activation antigen B7 binding to T-cell-specific surface glycoprotein CD28. Enriched tumor promoting immune cells (Tregs, TAMs, MDSCs) and LUAD cells express co-inhibitory receptors like programmed cell death 1 receptor (PD1), which bind to programmed cell death receptor ligand 1 (PD-L1) on T- and B-cells and further blocks downstream activation cascades. Whereas inhibitory co-signals normally prevent excessive T- and B-cell activation and uncontrolled inflammation, it shuts down the adaptive anti-tumoral immune system in the TIME.

The importance of these inhibitory co-signals for LUAD tumorigenesis was shown by interventions which target inhibitory receptors with so called immune checkpoint inhibitors. The PD1 antibody Pembrolizumab blocks PD1-receptors and disturbs its inhibitory co-signal by binding to PD-L1. Unblocked CD8+-T cells in turn re-activate and invade the TIME to eliminate LUAD-tumor cells. The clinical benefits of this mechanism were shown in the KEYNOTE-024 clinical trial, in which 305 patients with stage 4 NSCLC tumor lesions and a tumor cell PD-L1 expression of 50% or greater were enrolled. The patients were divided in two cohorts, treated with a chemotherapy regime either based on platinum or pembrolizumab. Pembrolizumab significantly enhanced the progression free survival (Hazard ratio, 0,50, median 4,3 months) and the overall survival (Hazard ratio, 0,63; 30,2 vs 14 months) (Reck et al., 2019). This study outlines that NSCLC patients benefit from disrupting the pro-tumoral TIME making the LUAD associated immune system a relevant target for further therapeutic approaches.

1.4.4 Tumor associated macrophages (TAMs)

Tumor associated macrophages are a key-regulatory immune subpopulation in the TIME and either promote the activation of anti-tumoral immune response or ensure tumor outgrowth by acting pro-tumoral and block effector immune cells.

In general, macrophages are part of the innate immune system and assigned to the subgroup of antigen-presenting cells, which only refers to one function out of many others such as wound healing, tissue engineering, defending from infectious disease and much more. These various functions are met by a broad spectrum of different macrophage phenotypes adapting to the needs of the residing tissue. Macrophages develop from bone-marrow derived myeloid precursor cells and migrate into the tissues to fulfill their local functions and maintain tissue homeostasis.

Macrophages, which accumulate in or nearby tumor lesions are defined as tumor associated macrophages and, depending on their phenotype, contribute to functions either eliminating or promoting carcinogenesis such as (i) regulation of angiogenesis (ii) recruitment, activation, or inhibition of effector immune cells (iii), influencing metastasis and (iv) tumor metabolism. The required functional phenotypes are shaped by the surrounding environment including normal cells, immune cells and the TME, which all expose TAMs to different cytokines.

Even though macrophages in tumor lesions are largely diverse, they can be grouped to moreover tumor promoting phenotypes supporting the needs of outgrowing tumors (M2-phenotype) or tumor inhibiting phenotypes contributing to tumor cell elimination by the immune system (M1-phenotype). This differentiation between the two extreme sides out of a broad spectrum of phenotypes allows to characterize the TIME as either pro- or antitumoral and is defined as macrophage polarization.

The tumor suppressing M1 macrophages differentiate after being exposed to damage-associated molecular patterns (e.g., Tumor antigens), which bind to macrophage surface receptors like toll like receptors (TLRs). Activated tumor associated M1-macrophages regulate tumor cell elimination by phagocytizing tumor cell remnants, which they further expose as antigens bound to MHC complexes and present to cytotoxic anti-tumoral T-cells (CD8+- /γδ- T-cells). Furthermore, M1-TAMs secrete pro-inflammatory cytokines to recruit immune cells into the TIME.

On the other side cancer cells secrete cytokines (Interleukin (IL)-4, -10, -13, TGF-β or prostaglandin E2), which differentiate precursor macrophages to M2-macrophages. M2-TAMs promote tumor proliferation by inhibiting the M1 initiated anti-tumoral immune response, decreasing MHC bound tumor antigens, enhancing the expression of inhibitory immune checkpoint proteins, and recruiting immune cell inhibitory Treg-cells into the TIME. Moreover, M2-TAMs not solely influence immune cells but remodel the ECM with matrix metalloproteases to gain space for tumor growth and to produce metastasis. Additionally, they secrete vascular endothelial growth factor (VEGF), which enhances tumor angiogenesis and increases nutritional resources.

LUAD tumorigenesis is preserved by the accumulation of M2- macrophages and depression of M1-phenotypes in the TIME. It is assumed that the repolarization of macrophages to an M1-phenotype for example by the release of DAMPs might be beneficial for antitumoral immune therapies and is therefore addressed by us in the present doctoral thesis. (Chung et al., 2012; Dai et al., 2010; Kim et al., 2008; C. Lee et al., 2019; Ma et al., 2010; Ohri et al., 2009; Welsh et al., 2005; Xiao et al., 2020; Zhang et al., 2011).

1.5 Cell death

Evasion of cell death is a critical hallmark of carcinogenesis securing prolonged survival of cancer cells, which suffer from external threats during oncogenic transformation and proliferation. Different influences from the surrounding tissue such as immune cells and insufficient supply for needed energy resources initiate programmed cascades inhibiting proliferation and, in the end, induce cell death to rescue from non-functioning, transformed cells.

These cascades are moreover important as they build the foundation of anti-cancer therapies including chemotherapy, radiation therapy, immunotherapy because of initiating therapy induced cell death. Vice versa, the accumulation of cell death resistance is often associated with therapy resistance in cancer cells. Whereas the evasion of non-inflammatory cell death like apoptosis has been shown in lung cancer by various mechanisms, the role of immunogenic pathways remains elusive.

As immunogenic cell death cascades not only induce death but furthermore inflammation and the recruitment of immune cells, these alternative death cascades might promote anti-tumoral immune responses. Regarding the possible immune cell recruiting, anti-tumoral role of alternative death cascades, we analyzed immunogenic cell death in lung adenocarcinoma in the present doctoral thesis.

1.5.1 Necroptosis

Necroptosis is a necrotic form of cell death consequently disturbing membrane integrity and releasing immunogenic cytosolic content. Hence, the initiated tissue inflammation exceeds any triggered immune reaction by non-necrotic forms of cell death like apoptosis and may substantially contribute to anti-tumoral immune responses.

In detail, the necroptotic pathway is induced by common cell death receptors like the tumor necrosis factor superfamily (TNFR), which are best understood for necroptosis activation. In the most studied paradigm, TNF is released from anti-tumoral immune cells, which invade the TME (e.g., M1-TAMs) and binds to the transmembrane TNFR. These receptors oligomerize and release receptor-blocking proteins (silencer of death domain proteins, SODDs) to subsequently expose so-called death domains (DD-motif). The DD-motifs function as adaptor domains for proteins carrying a DD-homologue sequence in their scaffold, most importantly: (i) Fas-associated protein with death domain (FADD), which mediates apoptosis induction and (ii) receptor-interacting serine/threonine-protein kinase 1 (RIPK1), which in the absence of caspase 8 induces necroptosis. Of note, the determination whether TNF signaling induces cell survival, apoptotic or necroptotic cell death depends on the conformation of RIPK1, which is mediated by posttranslational modifications: ubiquitylation- and phosphorylation. RIPK1 ubiquitylation at distinct protein residues is induced by enzyme 3 (E3)-ubiquitin-ligases in particular TNF receptor associated factors 2/5 (TRAF2/5), cellular inhibitors of apoptosis proteins (cIAPs) and linear ubiquitylation

assembly complex (LUBAC). Polyubiquitylation RIPK1 induces nuclear factor kappa B (NF-κB) and mitogen-activated protein kinase-cascade (MAPK-cascade), which both promote transcription factors for several anti-apoptotic and pro-inflammatory proteins. Additionally, NF-κB enhances the transcription of FADD-like-IL-1β-converting enzyme-inhibitory protein (c-FLICE-inhibitory protein, cFLIP), which in turn inhibits TNFR-induced-apoptosis by disturbing FADD dependent caspase-8 activation. To execute necroptosis, RIPK1 is liberated from the TNFR complex giving the chance to interact with the necroptosis key-regulatory protein RIPK3 in the cytosol. This process depends on proteins restructuring the RIPK1 scaffold like cylindromatosis lysine 63 deubiquitylase (CYLD). CYLD removes previously attached ubiquitin chains from RIPK1 to destabilize the TNFR binding death domain and to open a RIPK3 binding adaptor domain (receptor interacting protein (RIP) homotypic interaction motif, RHIM) (Wei et al., 2017). RHIM interaction facilitates RIPK1/RIPK3 oligomerization resulting in a polymeric complex defined as the necrosome (Li et al., 2012). In the necrosome RIPK1 and RIPK3 use their kinase function to cross-phosphorylate each other and activate necrosis executing proteins especially mixed-lineage kinase domain like protein (MLKL). Activated phospho-MLKL exposes a four-helical bundle domain (4HBD), which polymerizes MLKL monomers to octameric ion channels in the cell membrane (Huang et al., 2017; Liu et al., 2017; Quarato et al., 2016). Additionally, MLKL binds to membrane cation channels like transient receptor potential cation channel (TRPM7) and thus enhance cellular ion influx. The accumulation of sodium and calcium increases the intracellular osmotic pressure, which forces water molecules into the cell further leading to cell swelling and consequently membrane rupture. In the end, the release of intracellular content into the extracellular matrix triggers inflammation and associated immunogenic reactions.

Besides TNF induced necroptosis, other death activating substances such as DAMPs or physical/chemical stressors initiate necroptosis and are even more prevalent in tumor cells and the TME. For example, the DAMP recognizing TLR receptors 3,4 and 9 induce necroptosis via toll-interleukin-domain containing adapter inducing interferon-β (TRIF), which has a RHIM domain to interact and activate RIPK1 and 3 (Kaiser et al., 2013). Although the necroptosis executing necrosome is defined as RHIM interacting RIPK1/RIPK3-oligomer, RIPK3 can initiate necroptosis independently from RIPK1 by RHIM interaction with other RHIM carrying proteins such as TRIF or DNA-dependent activator of IFN-regulatory factors (DAI) (He et al., 2011; Kaiser et al., 2013; Lin et al., 2016; Newton et al., 2016). This instance defines necroptosis as RIPK3 dependent necrotic cell death pathway (Galluzzi et al., 2018; Kaiser et al., 2011).

1.5.2 The role of necroptosis in cancer

Necroptosis constitutes a potential tumor suppressive cell death pathway in LUAD because of eradicating tumor cells and furthermore raising tissue inflammation, which may establish an anti-tumoral immune environment.

Hints for a tumor suppressive role of necroptosis are given by frequently decreased mRNA levels of pathway executing proteins such as RIPK1, RIPK3, MLKL and CYLD in human cancer expression profiles. The clinical relevance of the stated tumor suppressive function is assumed because the overall survival rate is worse for patients with low RIPK3 mRNA levels in breast-, gastric-, colorectal cancer and melanoma (Ertao et al., 2016; Feng et al., 2015; Geserick et al., 2015; Ke et al., 2013; Koo et al., 2015; Moriwaki, Bertin, Gough, Orlowski, et al., 2015; Stoll et al., 2017). Taken together, necroptosis supports the development of a tumor suppressive TIME by inducing necrosis like cell death, thereby releasing immunogenic DAMPs and tumor antigens into the surrounding ECM. These inflammatory molecules attract APCs like M1-TAMs, which in turn secrete cytokines or phagocytize cancer cell remnants further exposed to effector immune cells with anti-tumoral functions. Activated CD8+-T-cells recognize tumor cell epitopes, which may result in a tumor eradication. Of note, to sustain a tumor-eliminating TIME, RIPK1/RIPK3 additionally promote NF-κB downstream signaling, which contributes to the secretion of inflammatory cytokines and chemotaxis such as IL-1α, IL-6, IL-12. In contrast to the immunogenic and tumor suppressive role of necroptosis, it is also associated with tumor promoting inflammation. An increase in RIPK1, RIPK3, FADD and MLKL in pancreatic cancer enhances carcinogenesis *in vivo* and if highly expressed in human patients worsens the overall survival (Colbert et al., 2013; Seifert et al., 2016). In a tumor promoting TIME as seen in pancreatic cancer necroptosis induced inflammation may support the recruitment and activation of immune suppressive M2-TAMs as well as MDSCs. Cancer cells undergoing necroptosis secrete cytokines affecting bystander immune cells, which in case of an M2-dominated TIME may promote the suppression of anti-tumoral immune response in turn enhancing tumor progression. Such cytokines are C-X-C motif chemokine 1 (CXCL1), Sin3-associated polypeptide (SAP-130) and macrophage inducible Ca^{2+}-dependent lectin receptor (mincle) signaling (Seifert et al., 2016). Additionally, tumor associated immune cells produce radical oxygen species (ROS), which increase genomic instability and lead to an accumulation of critical DNA-mutations promoting tumorigenesis.

In conclusion the function of necroptosis in cancer is moreover diverse and either results in tumor promoting or suppressive effects depending on the resident immune system. In case of a resident tumor suppressing TIME, necroptosis might offer an antitumoral immunogenic pathway.

1.5.3 Necroptosis in lung cancer

The role of necroptosis in lung cancer such as LUAD is yet not clarified despite knowing that lung cancer patients with low expression of necrosome forming proteins (RIPK1, RIPK3) and MLKL have a worse disease-free survival (Park et al., 2020). In contrast to a potential tumor suppressive role, LUAD as well as LUSC patient samples and cell lines with high *RIPK1* mRNA levels accelerated lung cancer progression (Wang et al., 2013), which moreover points to a tumor promoting role. Observed mechanisms, which suppress the necroptosis key regulating protein RIPK3 rely on epigenetic methylation shown in a small group of LUAD cell lines furthermore suggesting a possible restoring option by demethylating agents if RIPK3 expression benefits LUAD treatment as a tumor suppressor (Q. Wang et al., 2020).

Overall, these observations suggest that the inhibition of necroptosis might benefit LUAD proliferation and survival. Nevertheless, the influence of necroptosis in LUAD tumorigenesis and changes in the associated TIME is still weakly investigated.

1.6 Objectives

The mortality rate of lung cancer is remaining in the lead of cancer associated deaths outlining the need of a better understanding of lung tumorigenesis and in turn novel treatment options. The most common subgroup of lung cancer is the lung adenocarcinoma (LUAD) frequently acquiring therapy resistance associated with repressed cell death cascades. This process is nowadays well described for non-immunogenic apoptosis but nevertheless remains elusive for immunogenic cell death cascades. Thereby, necroptosis is assumed to be a promising death pathway because not only promoting tumor death but moreover attracting and activating immune cells with possible antitumoral functions. Especially, the successful implementation of immune checkpoint inhibitors in the treatment regime of LUAD strengthens the important role of the immune system in the TIME. This doctoral thesis aims to define the impact of necroptosis on LUAD tumorigenesis, therapy and the associated TIME using LUAD GEMMs as well as human LUAD datasets and cell lines by further evaluating the relevance of the key pathway mediator: RIPK3. The experimental studies were designed to answer the following questions:

(A) Does RIPK3 function as a tumor suppressor in LUAD?

(B) Does the TIME change in a RIPK3 associated manner in LUAD?

(C) Are human LUAD cell lines expressing the necroptotic signaling cascade?

(D) Is necroptosis a relevant death cascade initiated by chemotherapeutics in human LUAD cell lines?

2 Material

2.1 Mouse experiments

2.1.1 Mouse lines

Mouse line	Genotype	Company	Reference
C57BL/6	$Kras^{tm4Tyj}/Kras^{+}$ ($Kras^{G12D}/Kras^{+}$)	The Jackson laboratory	Jackson *et al.* (Jackson et al., 2001)
C57BL/6	$Trp53^{tm1Brn}/Trp53^{tm1Brn}$ ($p53^{flox}/p53^{flox}$)	The Jackson laboratory	Marino *et al*. (Marino et al., 2000)

2.1.2 Mouse keeping

Name	Catalogue number	Company
Sealsafe Next Greenline IVC-cages	GM500	Tecniplast, Buguggiate, Italy
Sealsafe Next Blueline IVC-cages	1145T	Tecniplast, Buguggiate, Italy
Polycarbonate drinking bottles	ACBT0702	Tecniplast, Buguggiate, Italy
Metal bottle cap	ACCPS50	Tecniplast, Buguggiate, Italy
Polycarbonate mouse house (red)	GYM500	Tecniplast, Buguggiate, Italy
10mm food pellets (Breeding diet)	1314	Altronin Spezialfutter, Lage, Germany

Mouse keeping and mouse keeping materials were organized and administered from the centrum of preclinical research (ZPF) at the institution of TranslaTUM.

2.1.3 Genotyping of KC-LUAD and KPC-LUAD mice

DNA isolation

Name	Catalogue number	Company
Proteinase K from Tritirachium album	P8044	Sigma-Aldrich; Missouri; USA
Tris(hydroxymethyl)aminomethane (Tris); pH: 8,5	T1503	Sigma-Aldrich; Missouri; USA
Ethylenediamine tetraacetic acid (EDTA) 0,5 M	E177	VWR; Pennsylvania; USA
Sodium dodecyl sulfate (SDS) Pellets	CN30.2	Carl Roth; Karlsruhe; Germany
Sodium chloride (NaCl)	71376	Fluka Biochemika; St. Louis; USA

Genotyping PCR

Name	Catalogue number	Company
GoTaq® Green Master Mix	M7823	Promega; Fitchburg; USA
Custom Primers; forward/reverse	48190011	Invitrogen; Massachusetts; USA

Genotyping Primer

Genotype	Primer	Sequence (5`→3`)	Length
Kras$^{G12D/+}$	*Kras-WT*: forward	CAGCAGCTTCGGCTTCCTATT	270 bp
	Kras-WT: reverse	AGCTAATGGCTCTCAAAGGAATGTA	
	Kras$^{G12D/+}$: forward	CCATGGCTTGAGTAAGTCTGC	170 bp
	Kras$^{G12D/+}$: reverse	AGCTAATGGCTCTCAAAGGAATGTA	
p53$^{flox/flox}$	*p53-WT*: forward	GGTTAAACCCAGCTTGACCA	270 bp
	p53-WT: reverse	GGAGGCAGAGACAGTTGGAG	
	p53$^{flox/flox}$: forward	GGTTAAACCCAGCTTGACCA	390 bp
	p53$^{flox/flox}$: reverse	GGAGGCAGAGACAGTTGGAG	

Anesthesia, analgesia, and antagonists

Name	Trademark	Catalogue number	Company
Midazolam	Dormicum®	4921530	Ratiopharm GmbH; Ulm; Germany
Medetomidin	Dorbene vet®	07725742	Zoetis; New Jersey; USA
Fentanyl	Fentanyl-Janssen®	2084366	Janssen Cilag GmbH; Neuss; Germany
Meloxicam	Meloxicam	71125387	ACROS Organics; New Jersey; USA
Flumazenil	Anexate®	4470990	Hexal AG; Holzkirchen; Germany
Atipamezol	Revertor®	800732	CP-Pharma; Burgdorf; Germany
Naloxon	Naloxon-ratiopharm®	4788930	Ratiopharm GmbH; Ulm; Germany

2.1.4 Equipment for mouse intubation and virus administration

Mouse interventions were performed at the centrum for preclinical research of TranslaTUM. Basic experimental equipment for mouse interventions were provided from the institution (e. g. fixation plate, cold and infrared lights).

Name	Catalogue number	Company
Sub-Q-syringes	SRM (9184998) SRM (9210033)	BD Bioscience; Franklin Lakes; USA
Syringe Luer 2ml	210357	B. Braun; Melsungen; Germany
Sterican® Cannula 20G and 24G	210355	B. Braun; Melsungen; Germany
Introcan safety® Cannula	4251644	B. Braun; Melsungen; Germany

2.1.5 Equipment and reagents for lung resection

Name	Catalogue number	Company
Surgical scissor	91401	Fine Science Tools; California; USA
Surgical forceps	11000	Fine Science Tools; California; USA
Surgical suture; Trelon®	C0790065	B. Braun; Melsungen; Germany
Introcan safety® Cannula	4251644	B. Braun; Melsungen; Germany
Formalin (PFA)	41531400	Medite GmbH; Burgdorf; Germany

2.2 Molecular biological methods

2.2.1 RNA isolation

Name	Catalogue number	Company
Trypsin-EDTA (0.5%)	15400054	Life technologies; California; USA
TRIzol®	15596018	Life technologies; California; USA
Trichlormethan/Chloroform	3313.1	Carl Roth; Karlsruhe; Germany
Direct-zol® RNA Miniprep	R2051	Zymo Research; Freiburg; Germany

Reagents:	Amount:
Tri Reagent	50 ml
Direct-zol® RNA PreWash	40 ml
RNA Wash Buffer	12 ml
DNase I	1500 U
DNA Digestion Buffer	4 ml
DNase/RNase-Free Water	6 ml
Zymo-Spin® IIICG Columns	50 pcs
Collection Tubes	100 pcs

2.2.2 RNA reverse transcription

Name	Catalogue number	Company
QuantiTect Reverse Transcription Kit	205311	Qiagen; Venlo; Netherlands

Reagents:	Amount:
gDNA Wipeout Buffer	100 µl
Quantiscript Transcriptase	50 µl
Quantiscript RT Buffer	200 µl
RT Primer Mix	1,9 ml

2.2.3 PCR primers

Gene name	Primer sequence	Scale [µmole]	Company
RIPK1	Forward: TGGAAAAGGCGTGATACACA Reverse: TCCACTTCCCTCAGCTCATT	0,025	Sigma-Aldrich; Missouri; USA
RIPK3	Forward: CTTCCAGGAATGCCTACCAA Reverse: TCCATTTCTGTCCCTCCTTG	0,025	
MLKL	Forward: AGAGCTCCAGTGGCCATAAA Reverse: GCGGAGTCACTGTTTCATCA	0,025	
TNFR1	Forward: GTGCCTACCCCAGATTGAGA Reverse: TGTCGATTTCCCACAAACAA	0,025	
TNFR2	Forward: CAGACGTGGTGTGCAAGC Reverse: ATGGCCACCACGTTACAGAT	0,025	

2.2.4 Quantitative real time PCR

Name	Catalogue number	Company
ABsolute qPCR Plate Seals	AB1170	ThermoFisher; Massachusetts; USA
GoTaq® qPCR Kit	A6101	Promega; Fitchburg; USA

Reagent:	Amount:
GoTaq® Probe qPCR Master Mix, 2X	2 ml
CXR Reference Dye	100 µl
Nuclease-Free Water	2,5 ml

2.2.5 Conventional endpoint PCR

Name	Catalogue number	Company
GoTaq® Green Master Mix	M712B-C	Promega; Fitchburg; USA
Nuclease-Free water	P1195	Promega; Fitchburg; USA

2.2.6 Plasmid

Name	Catalogue number	Company
pLUAD	60226	Addgene; Massachusetts; USA
Sequence/Reference:	Map:	
AAV:ITR-U6-sgRNA(backbone)-pEFS-Rluc-2A-Cre-WPRE-hGHpA-ITR; Platt *et al.* (Platt et al., 2014)	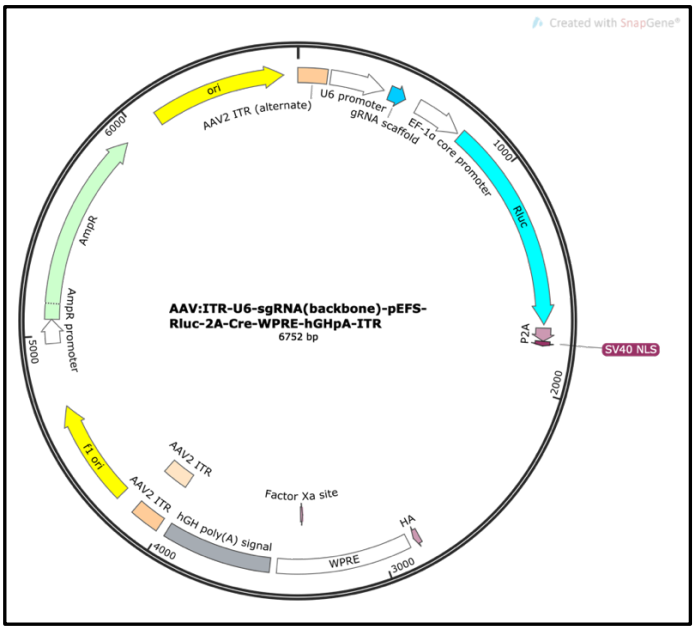	

2.2.7 Plasmid cloning

Name	Catalogue number	Company
T4 Polynucleotide Kinase Buffer	B0201S	New England BioLabs; Massachusetts; USA
T4 Polynucleotide Kinase	M0201S	New England BioLabs; Massachusetts; USA
Buffer G	BG5	ThermoFisher; Massachusetts; USA
BpiI (BbsI) (10 U/µl)	ER1011	ThermoFisher; Massachusetts; USA
LguI (SapI) (5 U/µl)	ER1931	ThermoFisher; Massachusetts; USA
Rapid Ligation Buffer	C671A	Promega; Fitchburg; USA
T4 DNA Ligase	M1801	Promega; Fitchburg; USA

2.2.8 Protein isolation

Name	Catalogue number	Company
RIPA lysis buffer	Ab156034	Abcam; Cambridge; United Kingdom
cOmplete ULTRA Tablets, Mini, *EASY*pack Protease inhibitor Cocktail	5892970001	Hoffmann-La Roche; Basel; Switzerland
Sodium fluoride solution (NaF)	201154	Sigma-Aldrich; Missouri; USA
Sodium orthovanadate solution (Na_3VO_4)	450243	Sigma-Aldrich; Missouri; USA

2.3 Biochemical methods

2.3.1 Protein concentration assay

Name	Catalogue number	Company
Pierce™ BCA Protein Assay Kit	23225	ThermoFisher; Massachusetts; USA

Reagent	Amount
BCA Reagent A	1000 ml
BCA Reagent B	25 ml
Albumin	10 ml (10 x 1 ml)

2.3.2 Agarose gel electrophoresis

Name	Catalogue number	Company
Agarose Standard, Roti®garose	3810.3	Carl Roth; Karlsruhe; Germany
SERVA DNA Stain Clear G	39804.01	SERVA; Heidelberg; Germany
BenchTop 100bp DNA Ladder	G829B	Promega; Fitchburg; USA
Ethylenediamine tetra acetic acid (EDTA) 0,5 M	E177	VWR; Pennsylvania; USA
Tris(hydroxymethyl)aminomethane (Tris); pH: 8,5	T1503	Sigma-Aldrich; Missouri; USA
Acetic acid	7332.1	Carl Roth; Karlsruhe; Germany

2.3.3 SDS-PAGE

Name	Catalogue number	Company
Tris(hydroxymethyl)aminomethane (Tris); pH: 8,5	T1503	Sigma-Aldrich; Missouri; USA
Sodium dodecyl sulfate (SDS) Pellets	CN30.2	Carl Roth; Karlsruhe; Germany
Hydrochloric acid (HCl)	100317	Merck; New Jersey; USA
2-Mercaptoethanol	63689	Sigma-Aldrich; Missouri; USA
Ethylenediamine tetra acetic acid (EDTA) 0,5 M	E177	VWR; Pennsylvania; USA
Bromophenol blue	T116.1	Carl Roth; Karlsruhe; Germany
UltraPure™ Glycerol	15514011	ThermoFisher; Massachusetts; USA
Rotiphorese® Gel 30	3029.2	Carl Roth; Karlsruhe; Germany
N, N, N`, N`-Tetramethylethylenediamine (TEMED)	T9281	Sigma-Aldrich; Missouri; USA
Ammonium persulfate (APS)	A3678-25G	Sigma-Aldrich; Missouri; USA
Glycine	3908.4	Carl Roth; Karlsruhe; Germany
PageRuler™	26616	ThermoFisher; Massachusetts; USA
2-Propanol (Isopropanol)	6752.4	Carl Roth; Karlsruhe; Germany

2.3.4 Cell death assay

Name	Catalogue number	Company
Recombinant Human Tumor Necrosis Factor-α (TNF-α)	210-TA-020/CF	R&D Systems; Minnesota; USA
Z-VAD-FMK	ALX-260-020-M001	Enzo Life Sciences; New York; USA
SMAC - mimetic, IAP Antagonist, BV6	533965	Sigma-Aldrich; Missouri; USA
Necrostatin-1, (Nec-1s)	2263	BioVision; California; USA
CellTiter Glo® Luminescent Cell Viability Assay	G7571	Promega; Fitchburg; USA

2.3.5 Chemotherapeutics

Name	Trademark	Amount	Company
Cisplatin	Cisplatin Teva	100 mg	Teva; Tikwa; Israel
Carboplatin	Carbomedac	600 mg	Medac; Wedel; Germany
Oxaliplatin	Eloxatin	100 mg	Sanofi; Paris; France
Etoposide	Eto-Gry	1000 mg	Teva; Tikwa; Israel
Paclitaxel	NeoTaxan	300 mg	Hexal AG; Holzkirchen; Germany
Pemetrexed	Alimta	500 mg	Lilly; Indiana; USA
Vinorelbine	Navirel	50 mg	Medac; Wedel; Germany
Gemcitabine	Hexal	2000 mg	Hexal AG; Holzkirchen; Germany

2.4 Microbiological methods

2.4.1 Material for Stbl3 E. coli cultures and transformation

Name	Catalogue number	Company
Stbl3™ Chemically Competent E. coli	10193952	Invitrogen; Massachusetts; USA
UltraPure™ Glycerol	15514011	ThermoFisher; Massachusetts; USA
LB-Medium (Luria/Miller)	X968	Carl Roth; Karlsruhe; Germany
Calcium chloride ($CaCl_2$)	A119	Carl Roth; Karlsruhe; Germany
Ampicillin, Sodium salt	HP62	Carl Roth; Karlsruhe; Germany
Super Optima broth with Catabolite repression media (S.O.C. media)	B9020	New England Biolabs; Massachusetts; USA

2.4.2 Plasmid isolation

Name		Catalogue number	Company
NucleoSpin® Plasmid		740588.50	Macherey-Nagel
Reagents:	Amount:		
Resuspension Buffer A1	15 ml		
Lysis Buffer A2	15 ml		
Neutralization Buffer A3	20 ml		
Wash Buffer AW	30 ml		
Elution Buffer AE	13 ml		
NucleoSpin® Plasmid Columns (white rings)	50		
Collection Tubes (2 mL)	50		

2.5 Immunological methods

2.5.1 Fluorescence-activated cell sorting (FACS) – chemicals

Name	Catalogue number	Company
Fetal bovine serum (FBS)	P30-1302	PAN-Biotech; Bavaria; Germany
Ethylenediamine tetra acetic acid (EDTA) 0,5 M	E177	VWR; Pennsylvania; USA
Phosphate buffered saline (PBS)	RNBG7730	Sigma-Aldrich; Missouri; USA
Alexa Fluor® 647 Annexin V	640943	BioLegend; California; USA
Propidium iodide solution	P4864-10ML	Sigma-Aldrich; Missouri; USA
2 - [4 - (2-hydroxyethyl) piperazine – 1 - yl] ethane sulfonic acid (HEPES) buffer	A1069,0100	AppliChem GmbH; Darmstadt; Germany
Sodium chloride (NaCl)	71376	Fluka Chemie GmbH; Buchs; Suisse
Calcium chloride ($CaCl_2$)	A119	Carl Roth; Karlsruhe; Germany
Magnesium chloride ($MgCl_2$)	KK36	Carl Roth; Karlsruhe; Germany
Potassium chloride (KCl)	6781	Carl Roth; Karlsruhe; Germany

2.5.2 Western Blot material

Name	Catalogue number	Company
Mini Trans-Blot® Cell	1703930	Bio-Rad; California; USA
Tris(hydroxymethyl)aminomethane (Tris)	T1503	Sigma-Aldrich; Missouri; USA
Glycine	3908.4	Carl Roth; Karlsruhe; Germany
Methanol ROTIPURAN®	4627.6	Carl Roth; Karlsruhe; Germany
Sodium dodecyl sulfate (SDS) Pellets	CN30.2	Carl Roth; Karlsruhe; Germany
TWEEN® 20	93773	Sigma-Aldrich; Missouri; USA
Ponceau S solution	P7170	Sigma-Aldrich; Missouri; USA
Skimmed Milk Powder	70166	Sigma-Aldrich; Missouri; USA
Amersham™ Protran™ 0,45µm	10600002	GE Healthcare Life science; Illinois; USA
Extra thick blot paper,	1703969	Bio-Rad; California; USA
Sodium azide	26628	Carl Roth; Karlsruhe; Germany
Pierce™ ECL Western Blotting Substrate	32209	ThermoFisher; Massachusetts; USA
Pierce™ ECL Plus Substrate	32132	ThermoFisher; Massachusetts; USA

2.5.3 Western Blot primary antibodies

Name	Catalogue number	Company
RIP3 Antibody	2283	ProSci; Colorado; USA
Purified Mouse Anti-RIP	610458	BD Bioscience; Franklin Lakes; USA
Recombinant Anti-MLKL antibody	ab184718	Abcam; Cambridge, United Kingdom
Anti-Beta-Actin (D6A8, HRP-conjugated)	8457	Cell Signaling Technology; Massachusetts; USA
Anti-Alpha-Tubulin (11H10, HRP-conjugated)	2125	Cell Signaling Technology; Massachusetts; USA

2.5.4 Western Blot secondary antibodies

Name	Catalogue number	Company
Goat anti-Mouse IgG (H+L), HRP	626520	ThermoFisher; Massachusetts; USA
Goat anti-Rat IgG (H+L), HRP	31470	ThermoFisher; Massachusetts; USA
Goat anti-Rabbit IgG (H+L), HRP	31460	ThermoFisher; Massachusetts; USA

2.6 Material for histological analysis

2.6.1 Preparation and embedding

Name	Catalogue number	Company
Embedding cassettes (12 mm, 6,5 mm)	7-0009, 7-0015	NeoLab; Heidelberg; Germany
Microtome blade S35	207500000	Feather; Osaka; Japan
Microscope slides; 45° corners	7695012	Th. Geyer; Höxter; Germany
Epredia™ SuperFrost Plus™	J1800AMNZ	Th. Geyer; Höxter; Germany
NUNC™ Thermanox®; Cover slips	E72280	Nalge NUNC International; New York; USA

2.6.2 IHC-Antibodies

Name	Catalogue number	Company
RIP3 antibody	2283	ProSci; Colorado; USA
SP-C antibody	Sc.7705	Santa Cruz; Texas; USA
CC10 antibody	Sc-9772	Santa Cruz; Texas; USA
CD3-SP7	CI597R06	DCS; Hamburg; Germany
Anti-CD8 (Hu)	DIA-TC8	Dianova; Barcelona; Spain
F4/80 antibody	MCA497R	Bio-Rad; California; USA
iNOS antibody	ab15323	Abcam; Cambridge; United Kingdom
Arginase-1 (D4E3M™) XP®	93668	Cell Signaling Technology; Massachusetts; USA

2.7 Cell culture experiments

2.7.1 Cell lines

Name	Species	Pathology	Catalogue number	Company
MEF: CF-1	Mus musculus	-	SCRC-1040	ATCC; Virginia; USA
NCI-H23	Homo sapiens	NSCLC, LUAD	CRL-580	ATCC; Virginia; USA
NCI-H358	Homo sapiens	NSCLC, LUAD	CRL-5807	ATCC; Virginia; USA
NCI-A549	Homo sapiens	NSCLC, LUAD	CCL-185	ATCC; Virginia; USA
NCI-H1437	Homo sapiens	NSCLC, LUAD	CRL-5872	ATCC; Virginia; USA
NCI-H1650	Homo sapiens	NSCLC, LUAD	CRL-5883	ATCC; Virginia; USA
NCI-H1975	Homo sapiens	NSCLC, LUAD	CRL-5908	ATCC; Virginia; USA
NCI-H2087	Homo sapiens	NSCLC, LUAD	CRL-5922	ATCC; Virginia; USA
NCI-H2126	Homo sapiens	NSCLC, LUAD	CCL-256	ATCC; Virginia; USA
HCC44	Homo sapiens	NSCLC, LUAD	ACC534	DSMZ; Leibniz; Germany

2.7.2 Cell culture media and supplements

Name	Catalogue number	Company
Dulbecco's Modified Eagle Medium (DMEM)	41966052	Life technologies; California; USA
Roswell Park Memorial Institute (RPMI) 1640	31870-074	Life technologies; California; USA
Fetal bovine serum (FBS) good forte	P40-47500	PAN-Biotech; Aidenbach; Germany
Penicillin-Streptomycin (10000 U/ml)	15140122	Life technologies; California; USA
2-Mercaptoethanol (50mM)	31350010	Life technologies; California; USA
L-Glutamine (200mM)	25030-032	Life technologies; California; USA
HEPES Buffer (1M)	15630-056	Life technologies; California; USA
Sodium bicarbonate solution	S8761-500ML	Sigma-Aldrich; Missouri; USA
Sodium pyruvate	11360-039	Life technologies; California; USA
D-Glucose	HN06.2	Carl Roth; Karlsruhe; Germany

2.8 General consumables

Name	Catalogue number	Company
Bacterial culture dishes	633180	Greiner Bio-One; Kremsmünster; Austria
Bacterial culture tubes	EC04.1	Carl Roth; Karlsruhe; Germany
Cell culture flasks (T25, T75)	833910302, 833911302	Sarstedt; Nümbrecht; Germany
Cell culture plates (6-, 48-, 96well)	833920, 833923, 833924	Sarstedt; Nümbrecht; Germany
Cell Strainer (70 µm, 100 µm)	352350, 9185508	BD Bioscience; Franklin Lakes; USA
DURAN® Erlenmeyer Flasks	5141144	Omnilab; Bremen; Germany
FACS Tubes (5ml)	551579	Sarstedt; Nümbrecht; Germany
Filter tips (10µl, 300µl)	771261, 738261	Greiner Bio-One; Kremsmünster; Austria
Filter tips (20µl, 1250µl)	7695882, 7695887	Th. Geyer; Höxter; Germany
Micro Tubes Flat Safeseal (0,5ml, 1,5ml, 2,0ml)	72704, 72706, 72695400	Sarstedt; Nümbrecht; Germany
Microtest-plates (96 well U-/V-form)	G080	Kisker; Biotech; Steinfurt; Germany
Multiply® PCR plates	721982202	Sarstedt; Nümbrecht; Germany
PCR Tubes/Caps	G006-Tuca	Kisker; Biotech; Steinfurt; Germany
Serological pipettes (10ml, 25ml, 50ml)	606180, 607180, 760180, 768180	Greiner Bio-One; Kremsmünster; Austria
Tissue culture dishes for adherent cells (10cm, 15cm)	833902, 833903	Sarstedt; Nümbrecht; Germany

2.9 Technical equipment

Name	Company
Accu-jet® Pro	Brand GmbH; Wertheim; Germany
Axiovert 40 C; Light microscope	Zeiss AG; Oberkochen; Germany
BE 500, Bacterial Incubator	Memmert GmbH; Schwabach; Germany
Biometra TAdvanced; PCR-Thermocycler	Analytik Jena GmbH; Jena; Germany
BOND RX Research Stainer	Leica Biosystems; Wetzlar; Germany
Cell culture Aspirator	STARLAB International GmbH; Hamburg; Germany
CO_2 Cell incubator	Binder; Tuttlingen; Germany
ENVAIR eco air H; laminar flow hood	ENVAIR Germany GmbH; Emmendingen; Germany
FACSCanto™ II; Flow Cytometer	BD Bioscience; Franklin Lakes; USA
Fusion FX; Western Blot Imaging System	Vilber; Paris; France
GloMax® Discover Microplate Reader	Promega; Fitchburg; USA
Innova 40, Bacterial Incubator Shaker	New Brunswick Scientific; New Jersey; USA
Leica RM2235; Manual Rotatory Microtome	Leica Biosystems; Wetzlar; Germany
Leica SCN400, Slide scanner	Leica Biosystems; Wetzlar; Germany
LightCycler® 480	Roche Diagnostics AG; Basel; Suisse
Mini-PROTEAN Tetra Cell system	Bio-Rad Laboratories; California; USA
NanoDrop1000; spectrophotometer	Thermo Scientific; Massachusetts; USA
Neubauer hemocytometer	Omnilab; Bremen; Germany
Pipette Multichannel: ErgoOne®	STARLAB International GmbH; Hamburg; Germany
Pipettes Eppendorf: Research®Plus, Multipette®Plus,	Eppendorf AG; Hamburg; Germany
Polymax 1040, Orbital-rocking shaker	Heidolph Instruments; Schwabach; Germany
PowerPac™ HC High-Current Power Supply	Bio-Rad Laboratories; California; USA
Precision and analysis scale	Sartorius AG; Göttigen; Germany
Precision scale	Kern & Sohn GmbH; Tübingen; Germany
Refrigerated Centrifuge: Multifuge 3s	Haereus; Hanau; Germany
Refrigerated Centrifuges: 5417R, 5810R	Eppendorf AG; Hamburg; Germany
Sub Cell GT Electrophoresis system	Bio-Rad Laboratories; California; USA
Thermomixer compact	Eppendorf AG; Hamburg; Germany
Tube Roller	STARLAB International GmbH; Hamburg; Germany
UVsolo; UV gel documentation system	Analytik Jena GmbH; Jena; Germany
Vortex-Genie™2	Scientific Industries, Inc.; New York; USA
WNB 29; Waterbath	Memmert GmbH; Schwabach; Germany

2.10 Softwares

Name	Version	Company
Affinity Designer	1.9.3	Serif, Ltd.; West Bridgford; United Kingdom
Aperio ImageScope	12.4.3	Leica Biosystems; Wetzlar; Germany
EndNote X9	9.3.2	Clarivate Analytics; London; United Kingdom
FlowJo Software	10.05.5	Tree Star Inc.; Ashland; USA
GraphPad Prism 9	9.1.2	GraphPad Software, Inc.; La Jolla; USA
ImageJ	1.52	Wayne Rasband; National Institute of Mental Health; Maryland; USA
Microsoft Excel	16.50	Microsoft; Redmond; USA
Microsoft Word	16.50	Microsoft; Redmond; USA
PyCharm	2021.1.2	JetBrains; Prague; Czech Republic
Python	3.9.5	Python Software Foundation; Delaware; USA
R statistics	4.1.0	R Core Team; R Foundation for Statistical Computing; Vienna; Austria
RStudio	1.4.1103	RStudio, PBC; Massachusetts; USA
SnapGene®	5.3.1	Insightful Science, LLC; California; USA
SnapGene® Viewer	5.3.1	Insightful Science, LLC; California; USA

3 Methods

3.1 Mouse experiments

In the present doctoral thesis, all experiments on mice followed the regulations of the German animal protection act. The animal experiments rely on the animal welfare recommendations of the Federation of European Laboratory Animal Science Associations. The experimental procedures were approved by the government of Oberbayern (Az.: ROB-55.2-2532.Vet_02-17-199, Az.: ROB-55.2-1-54-2532-55-12) and supervised or performed by trained post-doctoral research fellows, Dr. Deepti Agrawal and Dr. Caterina Branca. The qualification to work with experimental animals regarding annex 1, section 3, German animal protection act was obtained by completing the theoretical course: las-interactive and the practical training requirements. All mice used in the following experimentation originated from the C57BL/6 strain. New mouse lines were obtained from the Jackson Laboratory (Maine; USA) and were declared healthy as well as suitable for breeding and experimental procedures.

3.1.1 Genetic engineered mouse models for lung adenoma, lung adenocarcinoma

Two C57BL/6 mouse lines were established with genetic alterations to induce tumor formation of lung adenoma and adenocarcinoma. The first mouse line induced tumor lesions by Cre-dependent expression of the $Kras^{G12D}$ oncogene flanked by loxP sides (Jackson et al., 2001). This mouse model has the following genotype and will be further referred to as K-LUAD model.

$$< lox\text{-}STOP\text{-}lox\ Kras^{G12D/+} >$$

The second mouse model induced lung adenomas and adenocarcinomas by Cre dependent $Kras^{G12D}$ expression and *p53* deletion. The C57BL/6 mouse line with floxed (flanked by loxP-sides) *p53* sites was established by Marino *et al.* (Marino et al., 2000). This second mouse model is further referred to as KP-LUAD and has the following genotype.

$$< lox\text{-}STOP\text{-}lox\ Kras^{G12D/+},\ p53^{lox/lox} >$$

C57BL/6; $Kras^{G12D/+}$ and C57BL/6; $Kras^{G12D/+},\ p53^{lox/lox}$ mouse lines were established by Dr. Enkhtsetseg Munkhbaatar (Munkhbaatar et al., 2020).

3.1.2 Mouse housing

All mice were kept in pathogen free conditions in Sealsafe Next Greenline IVC-cages or Sealsafe Next Blueline IVC-cages. Cages were bedded with autoclaved cellulose and contained a red polycarbonate mouse house. The maximum number of mice per cage was calculated in compliance with the European directive for mouse keeping EU-RL 2010/63 and is shown in table 1.

Weight/ Mouse	< 20g	>20 – 25 g	>25 – 30 g	>30 – 35 g	> 40 – 50 g	> 50 – 60 g	>60 – 70 g	> 70 – 80 g
Surface are per cage:	Maximum number of mice per cage							
Blueline 435 cm^2	7	6	5	4	3	2	2	2
Greenline 501 cm^2	8	7	6	5	4	3	2	2

Table 1: Mice cages

Autoclaved water and food (Altromin, pellets) were administrated *ad libitum* and changed every week. The mouse rooms maintained a room temperature of 22 °C and were kept under a day-night cycle of 12 hours per phase.

3.1.3 Genotyping

The genetic background of all mice in the breeding and experimental settings were validated and controlled by genotyping mice after birth. Mouse DNA was isolated from ear punches after marking newborn mice. The DNA isolation protocol for mammalian tissue was adopted from Laird *et al*. (Laird et al., 1991). 250µl of sodium chloride-tris-EDTA (STE) buffer and 5 µl of proteinase K (20 mg/ml) were pipetted in a 1,5 ml Micro Tube containing the ear tissue. Concentrations of STE buffer supplements are shown in table 2. The suspended ear digestion solution was incubated overnight in an agitating thermoblock at 800rpm and 55 °C.

Name	Concentration
Tris-HCl; pH: 8,5	100 mM
EDTA; pH 8	5 mM
SDS	0,2 %
NaCl	10 mM

Table 2: Sodium Chloride-Tris EDTA (STE) buffer solution.

The digested tissue was pelleted by centrifuging for 10 minutes at room temperature at >20000g (14000 rpm). The supernatant was added to 250 µl of isopropanol, centrifuged again for 5 minutes (RT, 14000 rpm), discarded, and the isolated DNA resuspended in 150 µl of Tris-EDTA-buffer (TE-buffer: concentrations shown in table 3).

Name	Concentration
Tris-HCl; pH 8	10 mM
EDTA; pH 8	1 mM
NaCl	10 mM
	pH-Adjustment to 8.0

Table 3: Tris-EDTA (TE) buffer solution

Mouse genotypes were identified by conventional endpoint polymerase chain reaction (PCRs, see chapter 3.2). The utilized primers for the genotyping PCR protocols are listed in chapter 2.2.3. 2 µl of isolated DNA was added to 18 µl of the in table 4 listed master mix.

Name	Concentration
GoTaq Green	2X
Forward primer	10X
Reverse primer	10X
dH_2O	*Final volume of 20 µl per sample*

Table 4: Master mix for genotyping PCRs.

The PCR reagent was pipetted into 0,2 ml PCR tubes and placed into a thermocycler. The cycler protocol for genotyping-PCRs is shown in table 5.

Kras-WT, $Kras^{G12D/+}$				*p53-WT,* $p53^{flox/flox}$			
Program	Cycles	Temperature [°C]	Duration	Program	Cycles	Temperature [°C]	Duration
Denaturation	1	95	3 min	Denaturation	1	95	3 min
		95	30 sec			95	30 sec
Amplification	35	60	45 sec	Amplification	35	57	45 sec
		72	45 sec			72	45 sec
Cool down	1	4	∞	Cool down	1	4	∞

Table 5: Genotyping protocol for K- and KP-LUAD mice.

Amplified DNA products were separated and visualized by agarose-gel-electrophoresis. The obtained base pair lengths (bp) for *Kras-WT/KrasG12D, P53-WT/floxed-p53* are shown in figure 2 by a representative gel for 13 mice.

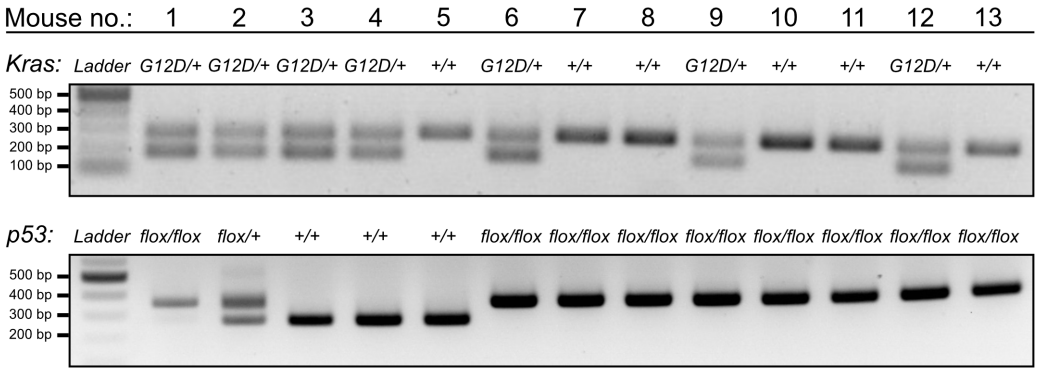

Figure 2: Genotypes of LUAD-GEMMs

3.1.4 Intratracheal Virus administration

6-8 weeks old C57BL/6, K-LUAD, and KP-LUAD mice were infected with adeno-associated viruses serotype 9 (AAV9). AAV9 was utilized as a viral vector shuttle system, delivering plasmids into lung epithelial and alveolar cells after application. Plasmids expressed Cre-recombinases and and a *sgLacZ* cassette with no complementary genomic target sequence for any possible Cas9 experimentation not utilized in the present doctoral thesis further leaving LUAD lesions *Ripk3* competent (pLUAD, see chapter 2.2.6). 30 minutes before starting the intubation all mice were anesthetized with intraperitoneal application of Midazolam (5 mg/kg BW), Medetomidin (0,5mg/kg BW) and Fentanyl (0,05 mg/kg BW). After ensuring a proper anesthesia by checking the pedal withdrawal reflex, the mice were placed on a plate with a 60° slant lying on the back. The upper incisor teeth were clamped into a spring-loaded mouth lock keeping it open during the intubation. A cold light source was used to visualize the larynx and a 24-gauge cannula was inserted into the trachea just before the tracheal bifurcation. 75µl of saline containing $1*10^{11}$ genome copies of AAV9 were injected into the lungs with a tuberculin syringe. After the virus administration was completed, the anaesthesia was antagonized with an intraperitoneal injection of Atipamezol (2,5mg/kg BW), Flumazenil (500 µg/kg BW) and Naloxon (1200µg/kg BW). All mice were checked for sufficient breathing after intubation and warmed with an infrared light.

3.1.5 Mouse lung resection and preparation

K-LUAD mice were euthanized 24 weeks- and KP-LUAD mice 16 weeks after AAV9 virus administration and tumor induction. The mice carcasses were dampened in 70% ethanol and placed under a sterile laminar flow hood on a Styrofoam plate covered with an aluminum foil. A thoracotomy was performed to prepare and release heart and lung lobes from the mediastinal- and thoracic cavity. A 5 ml syringe with a 22-gauge needle was drawn up with 1x phosphate buffered saline (PBS) to puncture the right heart ventricle and perfuse lung vessels removing the residual blood. A retrograde blood flow to abdominal organs was interrupted by performing a laparostomy and cutting the vena cava inferior under the lower liver margin. Afterwards a 24-gauge catheter with a 10ml syringe was placed in the trachea to inflate mice lungs with air. The air was trapped

in the lung by knotting up the trachea with a surgical suture. Lungs were removed by cutting the trachea below the larynx and placed into a 50 ml falcon containing 20 ml of 4% paraformaldehyde. Resected lungs were incubated for 48 hours at room temperature and then moved into 70% ethanol for 24 hours to start the dehydration. Subsequent histological tissue preparation steps are described in chapter 3.6.

3.2 Molecular biological methods

Experimental reagents containing RNA or proteins were continuously kept on ice. Experiments with cell lines were performed in a sterile environment under a laminar flow hood. All tubes used for RNA suspensions were declared RNase free and stored under sterile conditions. Hazardous substances such as 2-mercaptoethanol, TRIzol and chloroform were restricted to protective wear under a chemical hood. Plasmid sequences for LUAD initiating viral vector shuttles were obtained from Addgene® (see chapter 2.2.6)

3.2.1 Isolation of total RNA

Isolation of total RNA was based on the guanidinium thiocyanate-phenol-chloroform extraction method published from Chomczynski and Sacchi 1987 (Chomczynski & Sacchi, 1987). This method isolates nucleotides by phase separation. Denatured proteins enrich in the organic phenol phase, lipids in the lipophilic chloroform phase and nucleotides in the hydrophilic phase. DNA can be separated from RNA by adjusting the buffer pH to an acidophilic condition moving DNA into the organic phase. This method was extended using silica membranes. Positive charged ions complexed by silicon dioxid were bound to the negative phosphate backbone of nucleotide polymers like RNA or DNA. DNA remnants were further degraded with DNase. Total RNA was isolated from *in vitro* cell cultures, which were grown to a confluent monolayer on 10 cm coated cell culture dishes. Cell monolayers were washed with 10ml 1x PBS to remove not viable floating cell debris. Viable cells were detached by adding 3ml of trypsin per plate and incubating the cell culture plates for 3 min in a 37 °C cell incubator. 7 ml of antitrypsin containing media was given to cell-trypsin suspensions inhibiting the cell harming protease function of trypsin. The ingredients of the used cell medias differed between cultured cell lines and are described in chapter 2.7. Cell suspensions were removed from cell culture dishes and centrifuged in 15 ml falcons (5min, 400g, 4°C). After decanting trypsin containing supernatant, cell pellets were dissolved in 1ml 1X PBS and transferred into 1.5 ml Micro Tubes. Trypsin was further removed by washing the cell pellets twice with PBS (5min, 400g, 4°C). Washed cell pellets were lysed by 1ml of TRIzol. Cell-TRIzol suspensions were either stored in -20°C or used to continue the RNA isolation protocol.

0,2 ml of chloroform was added to 1ml TRIzol. The suspensions were incubated for 2-3 min at room temperature. Phase separation was achieved by centrifugation of the suspensions for 15 min at 12.000 g, 4 °C. The resulting aqueous phases (around 600µl) were transferred to new 1.5 ml Micro Tubes and mixed with 600µl of 100% ethanol. These suspensions were pipetted on Zymo-Spin® IIICG columns inserted in collecting tubes and centrifuged through silica membranes (15.000 g for 30 seconds). DNA leftovers were removed, adding 5µl DNase with 75 µl DNase digestion buffer. After 15 min of incubation silica membranes were washed with 400 µl of Direct-zol® RNA PreWash and 700 µl of RNA wash buffer. Adherent RNA was eluted with 100 µl of RNase-free water centrifuged at 15.000 g through the membranes and collected in RNase free Micro Tubes. Final RNA concentrations were measured with a spectrophotometer (Nanodrop). The RNA isolation protocol achieved a mean RNA concentration of 1000ng/µl per confluent 10 cm cell-culture dish.

3.2.2 Reverse transcription

Quantification of mRNA expression levels in cell lines were determined by reverse transcription – quantitative real-time polymerase chain reaction (RT-qPCR). This two-step procedure started by reverse transcription of total RNA into cDNA, needed for the DNA dependent Thermus Aquaticus (Taq) -polymerase.

Reverse transcription of total RNA into cDNA was based on the QuantiTect® Reverse Transcription protocol from Qiagon. All qPCR Primers were designed to span over two bordering exon sequences. This ensured an RNA specific amplification by losing signals of leaking genomic DNA having intron sequences, which prevent primers from binding. Genomic DNA leftovers of the RNA isolation protocol were eliminated by a DNA elimination buffer, which was mixed with 500ng of total RNA in 0,2 ml PCR tubes and incubated for 2min at 42 °C in preheated thermocyclers. All components of the gDNA elimination buffer are listed in table 6.

Name	Amount	Concentration
gDNA Wipeout Buffer	2 µl	1 X
Template RNA	10 pg – 1µg	
RNase-free water	*Final volume of 14µl per sample*	

Table 6: Genomic DNA (gDNA) elimination Buffer.

After gDNA degradation mRNA was reverse transcribed into cDNA.

Poly-thymine-primers were annealed to mRNA specific regions like poly-adenosine tails and initiated total mRNA reverse transcription. Other used RT-primers of the RT primer mix had similar mRNA specific annealing regions. 6µl of the reverse transcription master mix was added to RNA suspensions and incubated for 15 min at 42°C followed by 3 min at 95 °C in a thermocycler. The components of the reverse transcription master mix are listed in table 7.

Name	Amount	Concentration
Quantiscript Reverse Transcriptase	1 µl	
Quantiscript RT Buffer	4 µl	1X
RT Primer Mix	1 µl	

Table 7: Reverse-transcription Master Mix.

The used thermocycler program for reverse transcription is shown in table 8. Reverse transcribed cDNA was diluted with 180µl RNase and DNase free water (1:10) and either used for primer validation, qPCR or stored at -20°C.

Program	Temperature	Duration
Reverse transcription	42 °C	15 min
RT-Inactivation	95 °C	3 min
Cool down	4 °C	∞

Table 8: Thermocycler protocol for reverse transcription.

3.2.3 Quantitative real-time PCR (qPCR)

The qPCR was used to quantify gene expression folds of double stranded (ds)-cDNA by detection of fluorescent ds-DNA binding dye (Sybr Green®). Fluorescent emission intensity was measured after every PCR cycle correlating with the amplified target cDNA concentrations in the samples. To quantify mRNAs of interest, the number of cycles needed to reach a predefined threshold of fluorescent emission intensity (cycle threshold, Ct-value). The threshold was defined as the first differing fluorescence intensity between sample signal and background signal (quantification value). All samples and controls were used in triplets. The expression normalization for all samples was done by paired qPCR samples amplifying cDNA of interest and housekeeping cDNA for β-actin. For every sample 3µl of cDNA were added to 7 µl of qPCR-master mix into a 96-well qPCR-plate. The utilized primers for qPCR are listed in chapter 2.2. All components of the qPCR master mix are shown in table 9. Evaporation of qPCR suspensions was avoided by sealing the PCR plates with transparent foils.

Name	Amount	Concentration
GoTaq® Probe qPCR Master Mix, 2X	5 µl	1X
Forward primer	0,3 µl	0,3 µM
Reverse primer	0,3 µl	0,3 µM
Nuclease-Free water	1,4 µl	

Table 9: qPCR Master Mix.

The qPCR thermocycler protocol is described in table 10.

Program	Cycles	Temperature	Duration
DNA polymerase activation	1	95 °C	2 min
Denaturation	40	95°C	15 sec
Annealing and extension		60°C	1 min

Table 10: Quantitative qPCR protocol.

Ct-values were obtained after a mean qPCR running time of 1.5 h. The calculation procedure of gene expression folds was based on the $2^{\Delta\Delta Ct}$-method (Livak & Schmittgen, 2001). The average of all triplet Ct-values was calculated and normalized to the corresponding average β-actin Ct-value:

$$\Delta Ct = Ct\ (\text{Average gene of interest}) - Ct\ (\text{Average } \beta\text{-actin})$$

ΔCt-values were calibrated to a reference sample, which was either the sample with the lowest ΔCt value having the highest expression fold for the gene of interest or an experimental control sample.

$$\Delta\Delta Ct = \Delta Ct\ (\text{sample}) - \Delta Ct\ (\text{reference})$$

The gene expression fold was calculated by a primer efficiency of 2.

$$\text{Gene expression fold} = 2^{-\Delta\Delta Ct}$$

3.2.4 Conventional endpoint PCR

Conventional endpoint PCRs amplified DNA sequences within a pre-defined time duration. Conventional PCRs were used to replicate genomic transgene regions for the genotyping protocol and validation of primer effectiveness and specificity used for genotyping or qPCRs. Primer validation was done by adding 3µl of cDNA into PCR tubes containing the PCR-master mix (Table 11). All primers used for validation were designed with a melting temperature of 60 ± 1 °C to amplify cDNAs with the same qPCR and genotyping protocol. 3µl of control gDNA and 3µl of a negative control containing water was added to additional PCR tubes with 17 µl of the master mix.

Name	Amount	Concentration
GoTaq®Green Master Mix, 2X	10 µl	1X
Forward primer	0,6 µl	0,3 µM
Reverse primer	0,6 µl	0,3 µM
Nuclease-Free Water	5,8 µl	

Table 11: Conventional endpoint PCR Master Mix

The conventional endpoint PCR program shown in table 12.

Program	Cycles	Temperature	Duration
Denaturation	1	95 °C	1 min
Denaturation	30	95 °C	30 sec
Annealing		55 °C	1 min
Extension		72 °C	1 min
Taq inactivation	1	72 °C	5 min
Cool down	1	4 °C	∞

Table 12: Conventional endpoint PCR protocol.

3 µl of amplified DNA was used for an agar gel electrophoresis (see chapter 2.3.2).

3.2.5 Production of plasmids for LUAD initiation.

The *AAV:ITR-U6-sgRNA(backbone)-pEFS-Rluc-2A-Cre-WPRE-hGHpA-ITR* (further abbreviated as pLUAD) from Feng Zhang (Addgene plasmid #60226; http://n2t.net/addgene:60226; RRID: Addgene_60226) (Platt et al., 2014) contained the following inserts to induce LUAD lesions in K- and KP-LUAD GEMMs. The bacterial amplification codon with an antibiotic resistance gene as a selection marker:

<AmpR-promoter - AmpR - […] - ORI>

This sequence was used to amplify pLUAD plasmids in Stbl3 E. coli (see chapter 3.4). The Cre-recombinase coding sequence:

<EF-1α - RlucP2ACre - WPRE - hGHpoly(A)signal>

Cre-recombinase removed genomic floxed STOP codons to express *KrasG12D* and removed the floxed tumor suppressor gene $p53^{fl/fl}$ in KP-LUAD mice. Cre was expressed by the constitutive eukaryotic translation elongation factor 1 α (EF-1α) promoter. The woodchuck hepatitis virus posttranscriptional regulatory element (WPRE) enhanced Cre expression and the human growth hormone polyadenylation signal (hGHpoly(A)signal) inhibited protein degradation to further enhance Cre mRNA-translation.

3.2.6 Isolation of total protein

Total protein was isolated from cultured cell lines by radio-immune precipitation assays (RIPA). RIPA-detergents resolved lipidic cell membranes and released proteins from the cytosol, nucleolar and mitochondrial compartments. Isolated proteins were used for sodium dodecyl sulfate polyacrylamide gel electrophoresis (SDS-PAGE) and western blots (Ji, 2010). Cell pellets, protein suspensions and experimental reagents were precooled and continuously kept on ice. Cell pellets were suspended in RIPA lysis buffer adding a total volume of the double pellet size. The mean added RIPA volume was 150 µl of lysis buffer for a standard 10 cm cell culture dish containing $9x10^6$ cells at confluency and 100 µl of lysis buffer for a standard T75 cell culture flask containing $8.5x10^6$ cells at confluency. The lysis buffer was reduced to 50 µl for human

bronchial epithelial cell cultures (HBECs) and to an individual volume for every non confluent cell culture. The components of the lysis buffer are listed in table 13.

Name	Concentration
RIPA lysis buffer	10X
Protease inhibitor Cocktail	20X
Sodium fluoride solution (NaF)	100X
Sodium orthovanadate solution (Na_3VO_4)	100X
dH_2O	*Up to final volume*

Table 13: Lysis buffer for total protein isolation.

Suspended cell pellets were incubated on ice for 20 min and vortexed every 2 min. Afterwards the suspension was centrifuged for 20 min at (20.817) g and 4°C. The supernatant containing the isolated proteins was transferred into a new 1.5 ml Micro Tube and stored in -80°C.

3.3 Biochemical methods

Biochemical experiments were performed with conventional available kits (see chapter 2.3). Biohazard substances were used under a chemical hood. Temperature-sensitive reagents and samples were kept on ice.

3.3.1 Measurement of nucleotide concentrations

Nucleotide concentrations of isolated RNA or plasmids from cell line experiments were measured by a photo spectrophotometer (NanoDrop 1000). Nucleotide solutions were kept on ice during experimentation and stored at -80 °C before and after the measurement. Micro Tubes used for nucleotide solutions were RNase free. 2 µl of sample nucleotide solutions were pipetted onto the spectrophotometer and used to measure nucleotide concentrations and purities. All solution had to reach a 260/280-Ratio between 1,70-2,20 before including them to further experiments.

3.3.2 Measurement of protein concentrations

The concentration of isolated protein suspensions was measured by bicinchoninic acid assays (BCA-assays). These assays relay on the reduction of cooper ions from amino acids which complexes with bicinchoninic acid in alkaline conditions. Cooper BCA complexes were detected by characteristic light absorption at a wavelength of 562nm correlating with the amount of protein in the sample. Protein concentrations were calculated with an albumin standard curve using pre-defined concentrations. All samples were pipetted in a two-fold order into a 96 well plate. The amount of albumin per well is listed in table 14. 1 µl of each protein solution per well was sufficient to detect the BCA color reaction.

	1	2	3	4	5	6	7	8	9	10	11	12
	Amount of albumin per well [µl]											
A	0,2	0,4	0,6	0,8	1,0	2,0	4,0	6,0	8,0	10,0	12,0	14,0
B	0,2	0,4	0,6	0,8	1,0	2,0	4,0	6,0	8,0	10,0	12,0	14,0

Table 14: Amount of albumin for albumin standard curve

Every well was treated with 200 µl of BCA-Reagent to start the reduction and complexation. Protein assay plates were incubated for 30 min at 37°C and the light absorption of BCA complexes was detected in a plate photometer (GloMax®, Microplate reader). The known albumin concentrations were correlated to the resulting light absorption values giving an albumin standard curve approximated to a linear regression. Protein sample signals were normalized to blank sample signals. Protein concentrations were calculated by the linear function of the albumin standard curve.

$$\text{Fluorescent signal} = a * \text{protein concentration} + b$$

$$\text{Protein concentration} = (\text{Fluorescent signal}/a) - b$$

Albumin standard curves were considered valuable if the coefficient of determination (R^2) was higher than 0,95. The concentration of isolated sample protein was used to calculate the amount of protein needed for SDS-Pages.

3.3.3 Agarose gel-electrophoresis

Agarose gel-electrophoresis was used to identify amplified DNA sequences from PCR products. Amplified DNA bands were validated to determine the genotype of mice (see chapter 3.1) and the efficiency of DNA primers used for qPCRs (see chapter 3.2).

For a 1.5 % agarose gel, 1,5 g agarose and 100 ml Tris-Acetate-EDTA (TAE)-buffer were given into an Erlenmeyer flask and the solution was heated in a microwave until the agarose dissolved. 3µl of DNA intercalating DNA stain (sybr-safe) was added. The liquid agarose was continuously swirled while cooling the solution to 60-70 °C. The gel was poured evenly into a gel container including a 15 or 30 well comb. Air bubbles disturbing the DNA running lines were removed and the agarose gel left to solidify for 20 minutes. The container was placed into an electrophoresis chamber and covered by TAE buffer. The comb was removed and 8µl of each DNA PCR product as well as 4µl of DNA ladder were pipetted into the gel pockets. The DNA fragments got separated by applying 120 volts for 40 minutes. Negative charged DNA was attracted to the electrical anode and DNA fragments separated by having different numbers of negative charges depending on the length of their phosphate backbone. Afterwards the PCR products were visualized by a ultraviolet camera (UV-solo) and the length of the DNA fragments determined by the co-migrating DNA-ladder.

3.3.4 SDS-PAGE

Sodium dodecyl sulfate polyacrylamide gel-electrophoresis (SDS-PAGE) adapted from Laemmli *et al.* (Laemmli, 1970) was performed to separate denatured protein isolations by differing molecular weights. A total amount of 30 – 50 µg of isolated protein per sample was mixed with a 4x Laemmli buffer (see table 15), which contained 2-mercaptoethanol to reduce peptide disulfide bonds.

Name	Amount	Concentration
Tris-HCL pH: 6,8	2,0 ml	1M
Sodium dodecyl sulfate (SDS)	0,8 g	
Glycerol	4 ml	
2-Mercaptoethanol	0,4 ml	14,7 M
Ethylenediamine tetra acetate acid	1,0 ml	0,5 M
Bromophenol Blue	8 mg	

Table 15: Laemmli buffer.

4x Laemmli-protein solutions were further filled up with a 1x Laemmli buffer to a final volume of 20 µl per sample for a 15 well gel or 40 µl per sample for a 10 well gel. Protein solutions were denatured in a thermoblock at 95 °C for 10 minutes and then kept on ice before pipetting into the SDS-gels. The SDS-PAGE was performed discontinuously and split into a primary stacking gel and a secondary separating gel. Both polyacrylamide gels were made with hand cast units of the BioRad Mini-PROTEAN Tetra cell system. The recipes for stacking and separating gels are listed in table 16.

Separating gel			Stacking gel		
Name	Amount per gel	Stock Concentration	Name	Amount per gel	Stock Concentration
Tris pH 8,8	2,5 ml	1,5 M	Tris pH 6,8	3,025 ml	1,5 M
SDS	50,0 µl	20 %	SDS	1,2 ml	20 %
Rotiphorese®	4,0 ml	30 %	Rotiphorese®	25 µl	30 %
TEMED	5 µl		TEMED	5 µl	
APS	50 µl	10 %	APS	25 µl	10 %
dH_2O	*Final volume of 10 ml per gel*		dH_2O	*Final volume of 4,3 ml per gel*	

Table 16: Separating and stacking gel

Two spacer plates were assembled to a glass chamber in which at first the separating gel was poured. Bubble formation disturbing protein running lines was prevented by adding a temporary layer of isopropanol until the gel was solidified by radical polymerization of polyacrylamide, which took about 20 to 30 minutes. Afterwards the isopropanol was discarded, and the stacking gel was poured on top of the separating gel until the chamber was filled. Leftover bubbles were

removed, and the SDS-PAGE-comb inserted. Stacking gels solidified for an additional 20 minutes. Acrylamide-gels were either used directly or stored in the fridge at 4 °C in wet towels. The maximum storage time was one week. SDS-PAGEs were started by clamping the hand cast SDS-gels into a Mini-PROTEAN®Tetra vertical electrophoresis cell and filling the electrophoresis chamber with SDS-running buffer until the gels were covered (see table 17).

Name	Amount	Stock Concentration
Tris pure	30,2 g	
Glycine	144,0 g	
SDS	50 ml	20%
dH_2O	*Final volume of 1 l for 10 X stock,*	

Table 17: Running buffer (10X)

SDS-PAGE-combs were removed, and empty wells rinsed with running buffer. Laemmli-protein samples were pipetted into the wells sparing an additional well for 10µl of a PageRuler used to identify the immune marked protein of interest by showing multiple bands for defined molecular protein weights. SDS-PAGEs were run with constant 70 volts for 30 min to line up all samples in the stacking gel and subsequently with 130 V for 1,5 to 2,5 hours to separate the proteins by molecular weight in the separating gel. SDS-PAGEs were ended either after bromophenol blue of the Laemmli buffer left the end of the gel or for high weight proteins until the predicted position in the visible PageRuler bands reached 2/3 of the separating gel. Afterwards the protein containing gels were removed from the glass chamber and used to perform Western blots described in chapter 3.5.3.

3.3.5 Cell death assays

Programmed cell death was initiated in NSCLC-cell lines to analyze TNF- or chemotherapeutic induced apoptosis and necroptosis. Cell lines were treated in a sterile environment under a laminar flow hood.

Cell death assays were performed with 2000 cells per well seeded in a 96 well plate. After 24h of incubation, cells were treated with 500 µM human TNF-α and 1µM inhibitor of apoptotic protein antagonists (Second mitochondria-derived activator of caspase (SMAC) mimetics) to induce apoptosis. 50 µM of carbobenzoxy-valyl-alanyl-aspartyl-[O-methyl]- fluoromethylketone (Z-VAD-FMK), a pan caspase inhibitor, was added to block apoptosis and induce necroptosis. This TNF, SMAC, and Z-VAD-FMK (TSZ) treatment was antagonized by 10µM Necrostatin-1 (Nec1s), a RIPK1 antagonist (Cai et al., 2016). Chemotherapeutics were added in different concentrations according to presented titration curves (see chapter 4.10). Every treatment was run in triplicates in 100µl per well of suspended reagents in NSCLC media. Empty blanks and cells without treatment were included to calculate the baseline of cell viability. Cells were treated for 48 and 72 hours in the incubator. Cell death was detected with a luminescent cell viability assay

(CellTiter-Glo®), which detects intracellular ATP of viable cells via the ATP dependent luciferase reaction (Kangas et al., 1984). The 96 well plates and the CellTiter-Glo® reagents were equilibrated to room temperature for 30 minutes and subsequently 45 µl of media per well was removed. 50µl per well of CellTiter-Glo® substrates dissolved in CellTiter-Glo® buffer were added and the cell lysis enhanced by placing the plates on an orbital shaker. The luminescent signals were stabilized by keeping the plates in the dark under a Styrofoam box. After two minutes 80 µl per well of the cell lysate was transferred from transparent 96 well plates to white 96 well plates. The luminescent signal was detected in a GloMax® Discover Microplate Reader. Cell viability was calculated by normalizing the luminescent signal of treated cells to untreated cells:

$$\text{cell viability} = \frac{\text{mean luminescent signal of treated cells}}{\text{mean luminescent signal of untreated cells}}$$

3.4 Microbiological methods

Experiments with non-pathogen bacteria (Stbl3 Escherichia coli, E. coli) were restricted to a sterile laminar flow hood for non-infectious microbiology work. Stbl3 bacteria were used to replicate plasmids.

3.4.1 Transformation of competent Stbl3

Stbl3 E. coli were previously prepared to competent Stbl3 facilitating the intracellular uptake of produced plasmids. Gram-negative E. coli have negative charged phospholipid-residues in the plasma membrane, which in non-competent Stbl3 repel the negative phosphate backbone of DNA constructs. Therefore, positive charged calcium ions were enriched at the phospholipid membrane antagonizing the repulsive electric force. One glycerol stock of Stbl3 E. coli was added to 5ml Luria-Bertani media (LB-media) in a 10 ml bacterial culture tube. The recipe of LB-Media is described in table 18. The liquid bacterial culture was grown out overnight in a bacterial incubator by 37°C.

Name	Amount
Tryptone	10 g
NaCl	10 g
Yeast extract	5 g
dH_2O	*Up to 1 l*

Table 18: Luria-Bertani media recipe

Further experimental reagents and bacterial cultures were continuously kept on ice to inhibit bacterial growth. 2 ml of the Stbl3 culture was moved to 100ml LB Media in an Erlenmeyer flask and incubated for 1.5 h by 37°C. During the outgrow of Stbl3 bacteria the state of bacterial growth was kept in the log phase to prevent overgrowing and nutritional deprivation leading to bacterial death. The optical density of the liquid bacterial culture was measured after 1.5 h by a non-bactericidal wavelength of 600nm (OD_{600}). The log-phase was verified by a OD_{600} between 0,35-

0,5 (Atolia et al., 2020). Bacterial growth was stopped by taking the flask on ice for 15 min. Stbl3 cultures were split into two 50 ml falcons and centrifuged (11000 rpm,10 min, 4 °C). The LB-media supernatant was decanted, and the bacterial pellet dissolved in 10 ml precooled 100mM calcium chloride ($CaCl_2$) solution. Both suspensions were filled in a 50 ml falcon and an additional 5ml of $CaCl_2$ solution was added. This suspension was centrifuged again, and the supernatant decanted. The bacterial pellet was dissolved in 25 ml pre-cooled $CaCl_2$ and cooled for 2 h on ice. During this two-step procedure Ca^{2+} ions attached to the bacterial plasma membrane. The bacterial suspension was centrifuged again (11000 rpm, 10 min, 4 °C) and resuspended in 1,6 ml $CaCl_2$ plus 0,4 ml glycerol. 2 ml competent Stbl3 E. coli of the final stock solution was aliquoted in 1,5 ml Micro Tubes (25 µl/tube for 80 Micro Tubes) and stored at – 80 °C.

3.4.2 Transformation of Stbl3 bacteria

Plasmids were translocated into bacterial cells by chemical transformation. Previous described Ca^{2+} enrichment at the plasma membrane and heat shock treatment (Bergmans et al., 1981; van Die et al., 1983) increased cell membrane permeability facilitating DNA uptake. Translocation was initiated by mixing 10µl from each ligated plasmid product with 25µl of competent Stbl3 E. coli. In this suspension negative DNA-plasmids migrated to positive charged Ca^{2+} ions at the bacteria cell membrane. The suspensions were subsequently cooled on ice for 10 min and heat-shocked at 42°C for 45 seconds in a thermos-block. Heat exposed bacteria destabilized their plasma membrane integrity, interrupting the repellent barrier for plasmids. Shocked and labile bacteria were re-stabilized by cooling again for 2 min on ice and incubating in 200 µl of Super Optimal Broth with Catabolite repression media (SOC-media: 45 min, 37 °C and 300 rpm). SOC-media was used to buffer induced heat stress and favored plasmid uptake (Hanahan, 1983). The selection of successfully transformed Stbl3 bacteria was performed on LB-agar-selection plates. Plasmids contained ampicillin resistance genes making transformed bacteria resistant to ampicillin agar plates (see chapter 3.2.5, see Figure 3). 100µl of Stbl3 bacteria in SOC media were distributed on a 10 cm LB-agar-selection plate and incubated overnight.

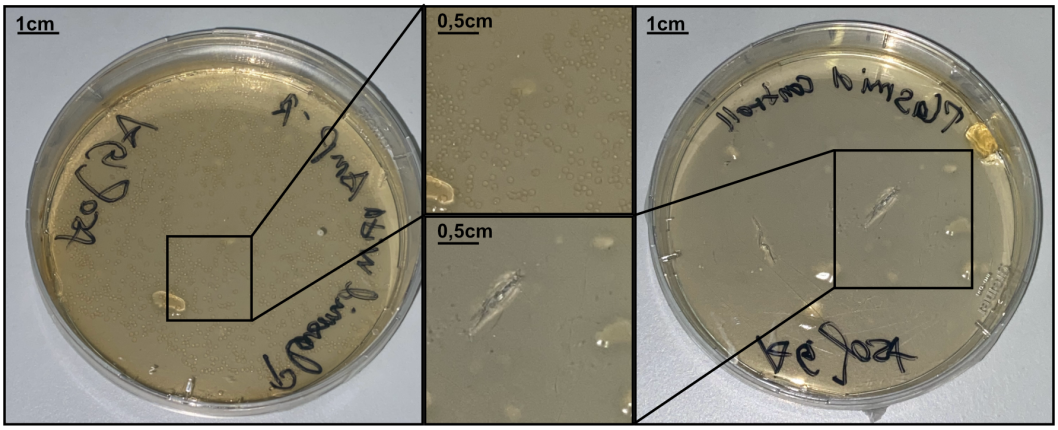

Figure 3: Selection plates of successfully transformed (left) and control Stbl3 E. coli (right) colonies.

Successfully transformed Stbl3 E. coli grew out multiple colonies on LB-agars. One colony was added to 10 ml LB-ampicillin-media in a bacterial tube. These liquid bacterial cultures were incubated overnight to replicate transformed plasmids using an Stbl3 compatible high copy number origin of replication in the plasmid sequences. 600 µl of each Stbl3 E. coli suspension was mixed with 600 µl glycerol in freezing tubes and stored at -80 °C. The rest of the bacterial cultures were used to isolate amplified plasmids.

3.4.3 Isolation of plasmids from Stbl3 bacteria

The extraction of plasmids from bacteria was based on the miniprep protocol (NucleoSpin® Plasmid NoLid) from Macherey Nagel (Birnboim & Doly, 1979; Vogelstein & Gillespie, 1979). Isolation of plasmid DNA relied on silica membranes, which got inserted in Micro Tubes. Silica membranes were treated with sodium containing buffers forming sodium-silicon dioxide complexes, which further bind negative phosphate groups of plasmid DNA. Liquid Stbl3 bacterial cultures were centrifuged (11000 g, 30 sec, room temperature) to remove LB-ampicillin-media. Remaining bacterial pellets were lysed by adding sodium dodecyl sulfate alkaline buffer (Buffer A2). NucleoSpin® columns were inserted in Micro Tubes and bacterial lysate suspensions were pipetted onto silica membranes. Columns were centrifugated to bind plasmid DNA to the membrane and collect unbound bacterial cell debris in Micro Tubes. Bound plasmid DNA was eluted by subsequently washing out complexed sodium ions from silica membranes with low ion alkaline buffer ((Buffer AE) 5mM Tris/HCL pH 8,5). Plasmid DNA was collected in RNase and DNase free Micro Tubes after centrifugation. The efficiency of plasmid isolation was measured by a NanoDrop spectrophotometer. The mean amount of isolated plasmid was between 200-300 ng/µl.

3.4.4 Production of adeno associated viruses

The transfection of produced plasmids in AAV9 was done by a viral vector core (Vector BioLabs).

3.5 Immunological methods

3.5.1 Fluorescence-activated cell sorting (FACS)

Fluorescence-activated cell sorting uses laser beams with predefined wavelengths to analyze and identify fluorochrome-marked proteins on the cell surface or cytosol. The cells can be counted and sorted for analysis on ongoing experiments. Single cells can be analyzed by their size using forward scatters (FSC) and their granularity using sideward scatters (SSC).

3.5.2 FACS for cell death detection

Chemotherapeutic induced cell death in NSCLC cell lines was identified as apoptotic- or necroptotic by measuring the cell membrane integrity using Annexin V and propidium-iodide in

a FACS based analysis. Thereby, Annexin V was used to bind phosphatidylserine residues in the outer layer of the cell membrane, which shifted from the inner to the outer leaflet after apoptosis activation. Annexin V bound to the cell membrane was detected by a conjugated fluorochrome. Propidium-iodide solution (PI) was used to identify necroptotic cell death, in which dying cells lose their cell membrane integrity and leak DNA. PI intercalates into free DNA and gives a red fluorescent signal in the FACS analysis. For a Annexin V/PI analysis 2000 NSCLC cells per treatment group were seeded into a 96 well plate and treated with either cisplatin or paclitaxel for 48 and 72 hours. Every individual treatment group was analyzed in triplicates. Treated NSCLC cells were washed with PBS and suspended in an Annexin V binding buffer (see table 19). Afterwards 0,2 µl of Alexa Fluor® Annexin V was added in every well and incubated for 15 minutes at room temperature followed by 10µl of a 1:50 dilution of propidium-iodide.

Name	Amount	Concentration
HEPES Buffer	4,76 g	100mM
NaCl	17,4 g	1,5 M
$CaCl_2$	4 ml	20 mM
$MgCl_2$	2 ml	10 mM
KCl	10 ml	50 mM

Table 19: Annexin V binding buffer.

Labeled cells were analyzed with a FACS Canto™ II flow-cytometer. Cell suspensions were first pre-gated for singlets by forward scatters (FSC-H, FSC-A) and the background signal including debris was further removed by forward and sideward scatters (FSC-A, SSC-A). Annexin V positive cells were detected in the Allophycocyanin (APC) channel and propidium-iodide positive cells in the Peridinin chlorophyll protein-Cyanine5.5 channel.

3.5.3 Western Blot

Western blots were performed with a wet blotting system (BioRad Mini-TransBlot®). An SDS-PAGE polyacrylamide gel (see chapter 3.3.4) was equilibrated in transfer buffer (see table 20).

Name	Amount
10X stock solution	
Tris(hydroxymethyl)aminomethane	58,2 g
Glycine	29,4 g
SDS (20%)	20 ml
dH_2O	Final volume of 1 l
Methanol for 1X solution	200 ml to 100 ml of 10X stock solution and 700 ml dH_2O

Table 20: Transfer buffer recipe

Size-separated proteins from SDS-gels were blotted on nitrocellulose membranes. Unblocked nitrocellulose membranes were kept in Transfer- or Tris-buffered saline with Tween20 (TBST) -buffer solutions. SDS separating gels were placed on activated nitrocellulose membranes. Membrane and gel were covered with soaked Whatman papers. Western Blot sandwiches were inserted into Western Blot clamps from the Mini-TransBlot® system and moved into chambers sitting in a TransBlot® tank. The tank was filled with Transfer Buffer until the membranes were completely covered. The blotting procedure was continuously cooled with a cooling unit in the tank and by covering the TransBlot® system with ice in a styrofoam box. Proteins were transferred to nitrocellulose membranes by electrotransfer with a constant current of 0,2 A for 1 gel or 0,4 A for two gels applied for 2 hours. Blotted membranes were washed in TBST, (see table 21) for five minutes.

Name	Amount
Tris pure	24,23 g
NaCl	80,06 g
TWEEN	2,5 ml
dH_2O	*Final volume of 1 l*
HCl	*pH adjustment to 7,4*

Table 21: 10X TBST-Buffer recipe

Protein binding capability of nitrocellulose membranes was blocked with 5% skim milk for 30 min. Primary antibodies binding to the protein of interest were added to 3 ml of 5% skim milk in a 50 ml falcon. Blocked membranes were placed in the falcons containing the primary antibody solutions (see table 22) and incubated on a tube roller overnight by 4°C.

Name	Concentration
Anti-Ripk3	1:2000
Anti-Ripk1	1:2000
Anti-MLKL	1:1000
Anti-Beta-actin	1:1000
Anti-Alpha-tubulin	1:5000

Table 22: Western Blot antibody concentrations

Unspecific antibody binding was prevented by washing membranes in TBST for 30 min. Proteins of interest marked with the primary antibody were visualized with an fc-region binding secondary antibody conjugated to a horseradish peroxidase (HRP). 2,5 µl of secondary antibodies were added to 5ml of skim milk in 50 ml falcons resulting in a final concentration of 1:2500. Membranes were incubated for 1,5 hours in the falcons containing the secondary antibody and washed again in TBST for 30 minutes to remove unspecific secondary antibodies.

The chemiluminescent signal initiated from the HRP conjugated enzyme was produced by Pierce ECL Plus Western Blot substrate (1ml per membrane). Peroxidases of the secondary antibody produced hydrogen peroxide generating acridinium esters reflecting strong chemiluminescent signals. The chemiluminescent signal was detected with a charge-coupled device camera imaging system.

The Western Blot loading control was either performed by cutting the blotting membrane at 50 kDa to simultaneously stain control proteins or followed after stripping antibody-stained membranes with stripping buffer (see table 23).

Name	Amount
TBST (1X)	15 ml
Sodium azide	150 µl

Table 23: Stripping buffer recipe

β-actine or α-tubulin were used for western blot loading controls. Primary antibodies binding β-actine or α-tubulin were directly conjugated with the HRP enzyme. The stripped or non-marked membrane was incubated for 1,5 hours in 5ml skim milk including primary HRP conjugated antibody used in a concentration of 1:2500. Afterwards, the membrane was washed in TBST and the HRP signal was detected with Pierce ECL Western blot substrate.

3.6 Histological methods

The following histological methods were supervised from the department of Pathology (Technical University of Munich). Single procedures were performed at the department of pathology and are not described in detail.

3.6.1 Paraffin embedding of mouse lungs

Resected and formalin incubated mouse lungs were transferred into 70% ethanol for 24 hours. Afterwards the lungs were cleaned by removing non-lung annexing tissue like trachea, heart and remaining mediastinal tissue. Lungs in toto were divided into 5 lung lobes following the anatomical lobe boarders. The right lung was separated into the upper right lobe (URL), the middle right lobe (MRL) and the lower right lobe (LRL) and the left lung into the left upper (LUL) and lower lobe (LLL). All 5 lobes were placed into a tissue embedding cassette and covered with 70% ethanol. The lung dehydration and paraffin fixation processes were performed at the Institute of Pathology with an automatic tissue processor. Lung paraffin blocks were returned to perform the sectioning protocol.

3.6.2 Sectioning of paraffin embedded lung tissue

Paraffin embedded lungs were sectioned with a two-step section procedure. Every step section had an interval of 100µm. Ten 2µm thick sections were taken in every interval. The last 10

sections were used for IHC analysis. Section 1-9 in the previous sectioning steps were removed leaving the tenth section for H&E stainings. Following this procedure for a 100µm interval and a 2µm cutting thickness every tenth cut was used for tumor burden analysis. All cutting sections were given into a prewarmed 40 °C water bath and placed on an acetone degreased microscope slide. Lung sections were dried overnight at 60 °C before starting the staining procedure.

3.6.3 Lung tissue staining

Lung tissue stains were performed, and quality controlled at the department of Pathology (Technical University of Munich). Hematoxylin and eosin (HE) staining was used to evaluate the pathology of tumor lesions and calculate the tumor burden. Immunohistochemistry (IHC) staining was performed by an automated staining system (Bond Max, Leica microsystems) to quantify RIPK3 expression and IHC scores for different immune populations in the tumor lesions. HE and IHC stained lung slides were scanned and digitalized with a SCN400 slide scanner (Leica microsystems).

3.7 Histological analysis

The analysis strategy was designed to testify the impact of RIPK3 expression on tumor progression and tumor immune microenvironment (see Figure 4). Histology slides were analyzed after digitalization with Tissue IA image analysis software (Slidepath, Leica microsystems). *Ripk3* expression in tumor lesions was quantified with anti-RIPK3 stainings. Tumor area of lesions showing high or low RIPK3 staining intensities was calculated on anti-RIPK3 IHC slides. Tumor infiltrating immune cells were scored with different immune IHC stainings after matching high or low RIPK3 expressing tumor lesions to similar immune stained lesions.

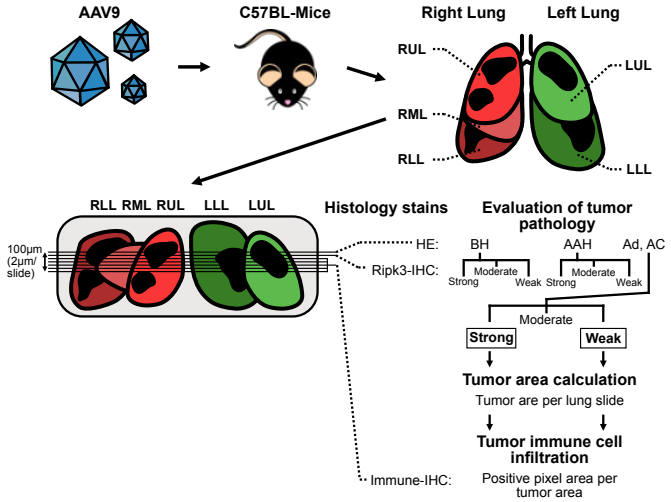

Figure 4: Analysis strategy of RIPK3 competent K- and KP-LUAD mouse lungs (RUL: Right upper lobe, RML: right middle lobe, RLL: right lower lobe, LUL: left upper lobe, LLL: left lower lobe).

3.7.1 Evaluation of tumor lesion pathology

The classification of lung tumor lesions was determined in regard of defined pathological criteria adapted from Nikitin *et al.* (Nikitin et al., 2004). Induction of lung adenoma and lung

adenocarcinoma was validated by staining LUAD cells of origin with anti-SPC (Surfactant protein C) for alveolar type 2 cells and anti-CC10 (Club cell protein 10) for Club cells (Jackson et al., 2001). Both epithelial cell types are known for being LUAD specific (Xu et al., 2012). All tumor lesions were grouped into either bronchial hyperplasia (BH), atypical adenomatous hyperplasia (AAH), or adenoma/adenocarcinoma (Ad, AC). The pathology of every lesion was determined on H&E slides showing the following criteria:

Bronchial hyperplasia: Enlarged and enriched cell clusters without showing cellular atypia. Hyperplastic cells keep the alveoli and bronchial tissue structure. Bronchial cells maintain apical cilia and cell-cell connections. Alveoli hyperplasia may thicken alveoli septa but do not show growth pattern atypia.

Atypical adenomatous hyperplasia: Grouped cell clusters partly keeping the alveoli or bronchial tissue structure. AAH show atypic cells with dense cell chromatin, reduced nuclei to cytosol ratio and dysmorphic cell structures (cuboidal, columnar, or acinar). AAH lesions can show adenoma like growth characteristics.

Adenoma and Adenocarcinoma: Delimited tumor burdens destroying the bronchial and alveoli tissue morphology. Adenomas and adenocarcinomas can show different growth patterns like solid, papillary, or mixed. Adenomatous cells are dysplastic having hyperchromatic and enlarged nuclei in cuboidal or columnar cell clusters. Adenomas have smaller lesion sizes (defined as smaller than 5mm). Compared to adenocarcinoma, adenomas have less cellular atypia and neovascularization. Adenocarcinoma further show more atypic and dedifferentiated cells and can induce metastasis. In the pathological evaluation advanced adenomas can be hardly distinguished from adenocarcinomas (Nikitin et al., 2004). Therefore, they are shown in one group: Adenoma and Adenocarcinoma (Ad, AC)

3.7.2 Evaluation of *Ripk3* expression

In LUAD mice the lesion pathology, tumor area per tumor lesion and amount of tumor immune cells per tumor lesion were categorized by different RIPK3 expression intensities. The *Ripk3* expression was semiquantitative scored on IHC-RIPK3 staining by 2 independent experimenters blinded to the lung pathology.

All IHC-RIPK3 slides had negative controls by non RIPK3 expressing normal lung alveolar cells and positive controls by high RIPK3 expressing lung macrophages. Tumor lesions were classified as RIPK3 low if the staining intensity was similar to non-RIPK3 expressing normal lung alveolar cells and high if the staining intensity was similar to RIPK3 high expressing lung macrophages. Tumor lesions were defined as RIPK3 intermediate if the staining intensity was between high and low tumor lesions.

3.7.3 Tumor burden calculation

Tumor burden was analyzed for LUAD adenoma and adenocarcinoma. The tumor area was measured with Tissue IA image analysis software (Slidepath, Leica microsystems). Tumor burdens were manually drawn by using the free hand mode allowing to calculate the circumscribed tumor area. The tumor burden was calculated on RIPK3-IHC slides after assessing RIPK3 staining intensities. The tumor area per lesion was compared between RIPK3 high or RIPK3 low expressing Adenoma and Adenocarcinoma.

3.7.4 Calculation of tumor immune cell infiltration in mouse LUAD lesions

Tumor immune cell infiltration in the K and KP-LUAD mice was calculated by a positive pixel count algorithm provided from the Tissue IA image analysis software (Slidepath, Leica microsystems). Positive stained immune cells were detected by counting IHC positive pixels of every immune cell in previously circumscribed tumor areas. The immune score was calculated by multiplying the amount of positive stained pixels with the area per pixel. This positive pixel area per tumor lesion was divided by the total area of the tumor lesion. 5 different immune IHC stains were used to analyse different immune populations in the tumor. Anti-CD3 and anti-CD8 IHC-staining were used to investigate infiltrating T-cell. Macrophages were detected by anti-F4/80 (EGF-like module-containing mucin-like hormone receptor-like 1), anti-iNOS (inducible Nitric Oxidase Synthase) and anti-Arginase1 IHC-staining.

3.8 Cell culture experiments

Cell culture experiments were performed with human and mouse cell lines in a sterile environment under a laminar flow hood. NSCLC LUAD cell lines were used to analyze the presence of the necroptotic signaling pathway and its impact on chemotherapeutic induced cell death. All cell lines were kept in CO_2 incubators at 37 °C and 5% CO_2 and plated on T75 flasks or cell culture dishes for adherent cells.

3.8.1 Cell culture of human non-small cell lung cancer cell lines

Human non-small cell lung cancer cell lines were used to investigate the executing part of TNF or chemotherapeutic induced necroptosis as well as apoptosis. Necroptosis was further characterized by validating the expression of the RIPK1/RIPK3 necrosome and the pore forming MLKL multimer. NSCLC cell cultures were incubated in T75 flasks or 10cm dishes. For every cell line 1 to 2 million cells were seeded and grown out for three to four days before becoming 90-100% confluent. NSCLC cells were grown in a modified RPMI-1640 media (see table 24) in incubators adjusted to 37 °C and 5 % CO_2.

Name	Concentration
RPMI-1640	-
FBS	10%
L-Glutamine	1%
HEPES-Buffer	1%
Sodium bicarbonate	2%
Sodium pyruvate	1%
Penicilin/Streptomycin	1%
Glucose	0,45%

Table 24: Human NSCLC cell media

3.9 Data and statistical analysis

Analysis of human datasets obtained from The Cancer Genome Atlas Project (TCGA) were performed in collaboration with Dr. Nicholas McGranahan and Dr. Michelle Dietzen form the UK Lung Cancer Center of Excellence, University College London (United Kingdom). All collaboration partners agreed to show the results of bioinformatic analysis in this thesis. TCGA datasets are provided from the National Cancer institute and downloaded from the Genomic Data Commons Data Portal (GDC) (Campbell et al., 2016; Cancer Genome Atlas Research, 2014). Data safety and security was ensured from the network system of the Technical University of Munich. Sensible patient data was investigated in encrypted formats. Collected data was processed in the R-statistical environment version 4.1.0.

3.9.1 Gene expression and gene ontology term enrichment analysis

LUAD datasets from TCGA were grouped into RIPK3 High and Low expression groups by using the upper and lower normalized RIPK3 expression quartiles. Both groups were compared and analyzed for significant up- or down regulated genes further corresponding to gene ontology terms. A total amount of 14170 genes were available and analyzed for significant differences between both groups and the 20 most significant up- and downregulated biological processes related to gene ontology terms were calculated.

3.9.2 Calculation of tumor infiltrating immune cells: Danaher score

The calculation of tumor infiltrating immune cells was based on expression profiles of quantified marker genes for different immune subpopulations in patient LUAD tumors. The protocol was published by Danaher et. al 2017 (Danaher et al., 2017). Validated gene sets for all immune populations are shown in table 25. Each immune cell specific Danaher score was calculated by the mean of log2 transformed and normalized marker gene expression values.

Cell type	Marker gene
B-cells	*BLK, CD19, MS4A1, TNFRSF17, FCRL2, KIAA0125, PNOC, SPIB, TCL1A*
CD45	*PTPRC*
CD8 T-cells	*CD8A, CD8B*
Cytotoxic cells	*CTSW, GNLY, GZMA, GZMB, GZMH, KLRB1, KLRD1, KLRK1, PRF1, NKG7*
Dendritic cells	*CCL13, CD209, HSD11B1*
Exhausted CD8 T-cells	*CD244, EOMES, LAG3, PTGER4*
Macrophages	*CD163, CD68, CD84, MS4A4A*
Mast cells	*MS4A2, TPSAB1, CPA3, HDC, TPSB2*
Neutrophils	*CSF3R, S100A12, CEACAM3, FCAR, FCGR3B, FPR1, SIGLEC5*
Natural killer $CD56^-$ cells	*IL21R, KIR2DL3, KIR3DL1, KIR3DL2*
Natural killer cells	*NCR1, XCL2, XCL1*
T-cells	*CD3D, CD3E, CD3G, CD6, SH2D1A, TRAT1*
Th1 cells	*TBX21*
Treg	*FOXP3*

Table 25: Marker genes for Danaher score calculations adapted from Danaher et al. (Danaher et al., 2017)

3.9.3 Statistical analysis

Statistical analysis was performed with Prism GraphPad Version 9.1.0 or R statistics Version 4.1.0. Normality and Lognormality were tested with Anderson-Darling Test or Kolmogorov-Smirnov test. Data sets with normal distribution were analyzed by classic Fisher or paired/unpaired t-tests and non-normal distributed datasets with nonparametric Mann-Whitney test. Contingency table analyses were performed with Chi-square or Fisher's exact tests.

4 Results

4.1 RIPK3 expression in human LUAD is associated with tumor suppressive gene ontologies.

To analyze the stated tumor suppressive potential of RIPK3 mediated necroptosis in human LUAD, we identified enriched biological processes in tumors with high *vs* low *RIPK3* mRNA counts. Regarding our hypothesis, that inflammatory cell death attracts immune cells by the expression of inflammatory molecules, we aimed to detect a transcriptome contributing to inflammation in RIPK3 high human LUAD samples. For doing so, we cooperated with Dr. Nicholas McGranahan and Dr. Michelle Dietzen form the UK Lung Cancer Center of Excellence, University College London (United Kingdom), who performed gene ontology enrichment analysis on mRNA sequenced human LUAD samples of the TCGA cohort.

To depict differentially expressed genes in human LUAD with high or low *RIPK3* expression levels, we investigated a total of 575 RNA sequenced LUAD samples. We compared those with a normalized *RIPK3* mRNA count higher than the 75% quartile (*RIPK3* high tumors) with those lower than the 25% expression quartile (*RIPK3* low tumors). In this analysis, we found 7799 differently expressed genes visualized on a volcano blot (Figure 5 A, B). The top up-regulated genes had an average log-transformed fold change of more than 1 and the top downregulated genes an average log-transformed fold change of less than -1 in *RIPK3* high *vs* low samples. The different normalized mRNA levels of these genes had a P value of < 0.05 (Classic Fisher Test) and were therefore reported as significantly different. All these genes are shown as red dots and labeled by their gene name (Figure 5 A, B). The top genes (significantly differing and log fold change > 1 or < -1; labeled as red dots) were included in gene ontology analysis to calculate the overall enrichment of biological processes in LUAD samples with high *versus* low *RIPK3* mRNA levels. Enrichment scores were based on fold change differences of the average mRNA count of genes in each ontology term. Up-regulated genes in *RIPK3* high tumors were found to participate in immunogenic processes such as regulation and activation of the immune system or the immune response (Figure 5 C), whereas down-regulated genes were involved in cell division or proliferation (Figure 5 D).

Taken together, these results suggest that an increased *RIPK3* expression in human LUAD correlates with an increase of immunogenic processes and a decrease of tumor cell proliferation. This underlines the stated tumor suppressive potential of the key regulator of the necroptotic pathway, RIPK3.

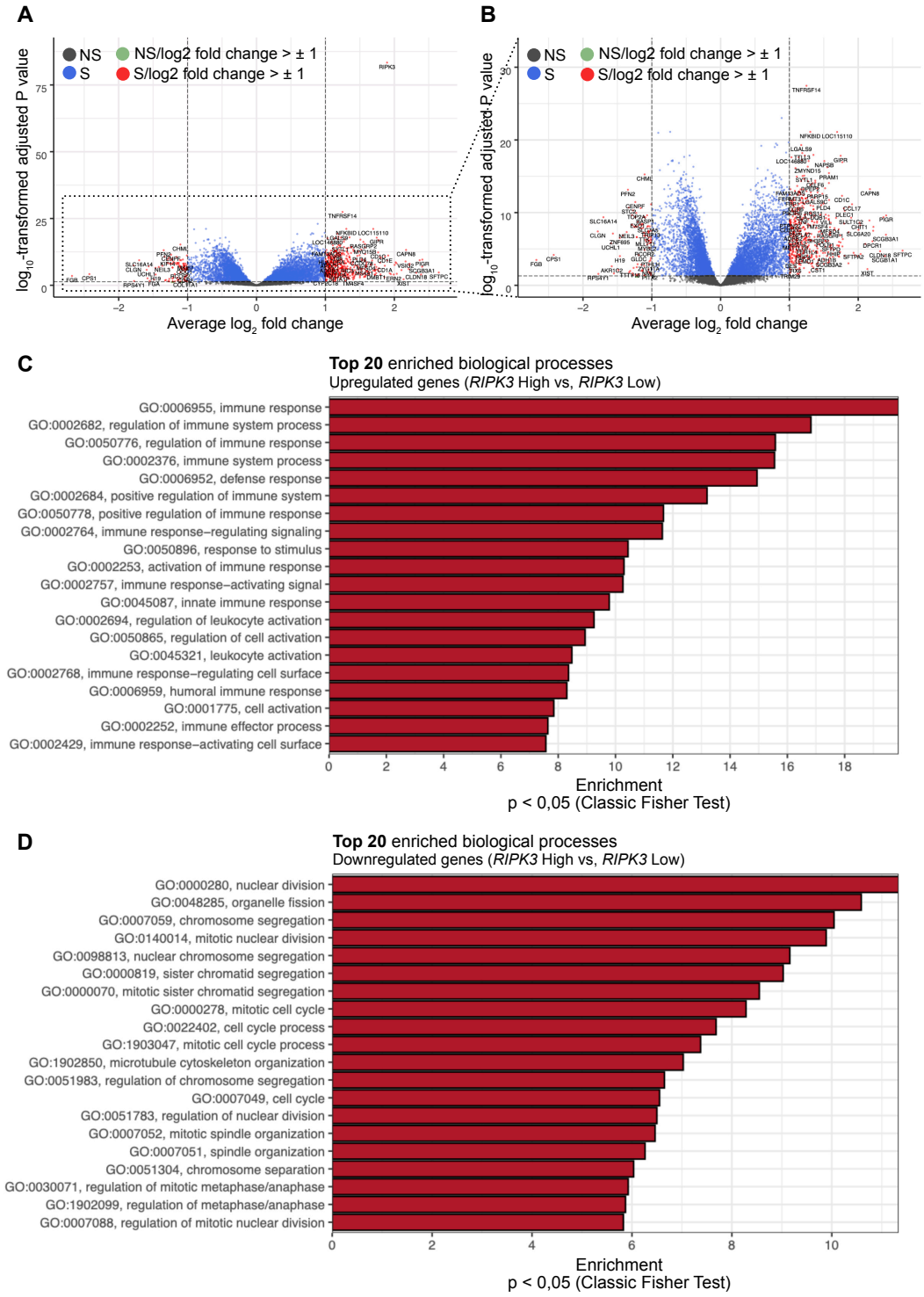

Figure 5: Gene expression profile and gene ontology enrichment analysis in human TCGA-LUAD datasets comparing high against low RIPK3 expressing tumor bulk samples. (A, B): Volcano-plots showing differentially expressed genes comparing human LUAD samples with high RIPK3 expression (normalized RIPK3 mRNA counts > 75%) and low RIPK3 expression (normalized RIPK3 mRNA counts < 25%) from TCGA datasets. (A): Complete Volcano-plot and (B) Volcano-plot without RIPK3 showing top increased genes with P value < 0.05 and average log-transformed fold change > ± 1 and top decreased genes with P value < 0.05 and average log-transformed fold change < ± 1 as red dot and labeled by gene-names (NS: non-significant, S: significant). (C, D): Gene-ontology analysis elucidating enriched biological processes associated with genes being significantly higher (C) or lower (D) expressed in RIPK3 high (upper quartile) versus RIPK3 low (lower quartile) tumor samples. Statistical analyses were performed by Classic Fisher Tests and significance reported by shown p-values. Bioinformatic analysis performed by Dr. Nicholas McGranahan and Dr. Michelle Dietzen.

4.2 High *RIPK3* expression correlates with enriched immune signals of different subpopulations

To evaluate whether the associated immunogenicity of human LUAD samples with high *RIPK3* expression impacts on the presence of different immune subpopulations in the tumor bulk samples, we calculated immune cell specific scores. Thereby, we were able to depict the presence of various subpopulations out of available LUAD TCGA datasets. The scores are based on immune cell marker genes, which are highly expressed if the immune cell of interest is present in the tumor sample or weakly expressed if not (Danaher et al., 2017) (see chapter 3.9.2) and were performed in cooperation with Dr. Nicholas McGranahan and Dr. Michelle Dietzen. The applied immune score was published by Danaher *et al.* and is further reported as Danaher score. To elucidate the impact of high *RIPK3* mRNA levels on immune signals compared to low *RIPK3* levels, we restricted our analysis to TCGA-LUAD samples with either having a *RIPK3* high (normalized *RIPK3* mRNA count > 75% of all human LUAD samples, upper quartile) or *RIPK3* low (normalized *RIPK3* mRNA count < 25% of all human LUAD samples, lower quartile) expression (upper vs lower quartile comparison). We excluded samples within the median plus middle quartiles of the *RIPK3* expression range (± 25%). We compared the immune score of 144 LUAD samples in the *RIPK3* low expression group with 144 samples in the *RIPK3* high expression group.

This analysis resulted in significantly increased Danaher scores for total tumor infiltrating lymphocytes in tumor samples with high *RIPK3* mRNA counts (Figure 6 A). The immune scores for analyzed immune subpopulations were also significantly higher in *RIPK3* high tumor samples except for natural killer cells and CD8+ T-cells. This outlined an enrichment of immune cells in tumor samples with high *RIPK3* mRNA levels. Especially, immune cells known to participate in antitumoral immune reactions such as antigen presenting macrophages and dendritic cells as well as effector immune cells (B- and T-cells) (Figure 6 B).

This suggests that human LUAD tumors with high *RIPK3* expression enrich antitumoral immune cells and establish an antitumoral immune microenvironment.

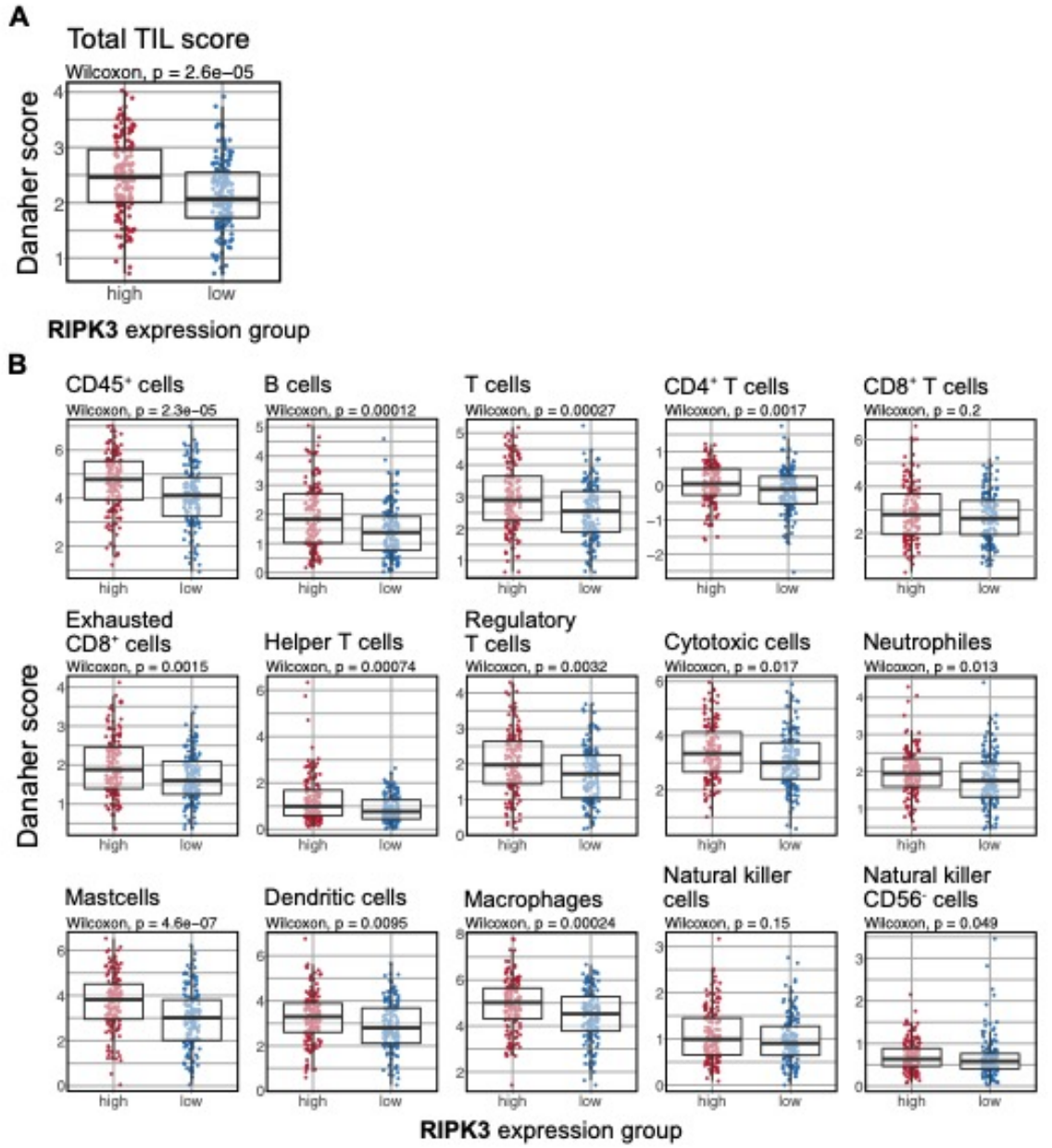

Figure 6: Danaher scores for RIPK3 high and low human LUAD samples. (A): Box plot showing the Danaher score of Total tumor-infiltrating lymphocytes for *RIPK3* high tumors (normalized *RIPK3* mRNA count > 75% of all TCGA-LUAD samples) and *RIPK3* low tumors (normalized *RIPK3* mRNA count < 25% of all TCGA-LUAD samples). (B): Box plots showing the Danaher scores of published immune subpopulations (Danaher *et al.* (Danaher et al., 2017)) for *RIPK3* high and low expression groups. Each box plot represents immune cell subpopulations as named above (A-B): Box plots indicate the mean with inter-quartile range (IQR) and maximum/minimum defined as 1,5 times of the IQR. Statistical analysis was performed by Wilcoxon tests and p-values are reported in the figures. Bioinformatic analysis performed by Dr. Nicholas McGranahan and Dr. Michelle Dietzen.

4.3 LUAD induction in *Kras$^{G12D/+}$* (K) and *Kras$^{G12D/+}$; p53$^{lox/lox}$;* (KP) LUAD mice.

The role of RIPK3 dependent necroptosis in the pathogenesis of LUAD tumors was studied in *Ripk3* competent mice to evaluate the non-modified biology of RIPK3 associated tumor suppression in a self-regulated wild-type setting. RIPK3 as a cell death regulatory protein was suspected to have tumor suppressive functions influencing tumor progression in LUAD mouse models. In *Ripk3* competent mice we investigated if LUAD tumors do depress RIPK3 and if the reduction of RIPK3 has any benefit on tumor progression.

KP-LUAD mice were intratracheally infected with Adeno-associated viruses (serotype 9, AAV9) (see chapter 3.1) liberated in infected lung cells 6-8 weeks after birth. Infected LUAD cells of origin developed macroscopic tumor lesions until week 16. The tumor development was driven by the induced mutations *Kras^{G12D}* and loss of *p53* (Figure 7 A-C). Macroscopic tumor lesions were predominantly found at the pleural lung sides (pleura visceralis) and the bronchial lining. Tumor pathology was validated on HE-staining by predefined criteria from Nikitin *et al.* (Nikitin et al., 2004). The most frequent pathologic phenotype in KP-LUAD mice were atypical adenomatous hyperplasia (AAH) and adenoma. Morphological LUAD phenotypes on HE-staining were further validated by LUAD specific IHC-staining for the marker proteins SPC and CC10. Both are expressed from LUAD cells of origin (CC10 from Club cells; SPC from Alveolar Type 2 cells). CC10 and SPC positive tumor cells were located at the tumor burden or in the middle of the tumor parenchyma and showed similar staining intensities compared to control non-dysplastic Club cells (CC10) or Alveolar Type 2 cells (SPC) (Figure 7 D).

K-LUAD mice were also infected with AAV9 plasmids 6-8 weeks after birth and developed macroscopic tumor lesions after 24 weeks of infection. The tumor driving mutation was restricted to *Kras^{G12D}* (Figure 7 A-C). Tumor lesions in the macroscopic lungs were mainly found in the bronchial lining and few at the lung pleural side. Pathological characterization was performed on HE-staining, showing less dysplastic lesions compared to the KP tumors with a dominant fraction of bronchial hyperplasia (BH) and AAH. K-LUAD lesions were further validated for LUAD specific marker proteins SPC and CC10 and showed positive cells at the tumor burden and in the tumor parenchyma (Figure 7 E).

Loss of *p53* in KP-LUAD tumors enhanced tumor progression in adenoma and adenocarcinoma (Ad, AC) compared to *Kras^{G12D}* restricted K-LUAD tumors. The *Kras$^{G12D/+}$, p53$^{\Delta/\Delta}$* genotype showed bigger tumor areas after 16 weeks than *Kras^{G12D}* mice after 24 weeks (Figure 7 F). *P53* had no significant influence on LUAD tumor initiation. The number of tumors per lung in K and KP mice did not differ significantly (Figure 7 G). These results suggest that *p53* loss does not initiate LUAD tumors but enhance tumor growth by losing *p53*-mediated cell cycle stop and tumor cell rescue mechanisms, as described by Wang *et al.* (Wang et al., 1995) (see chapter 1.1.3).

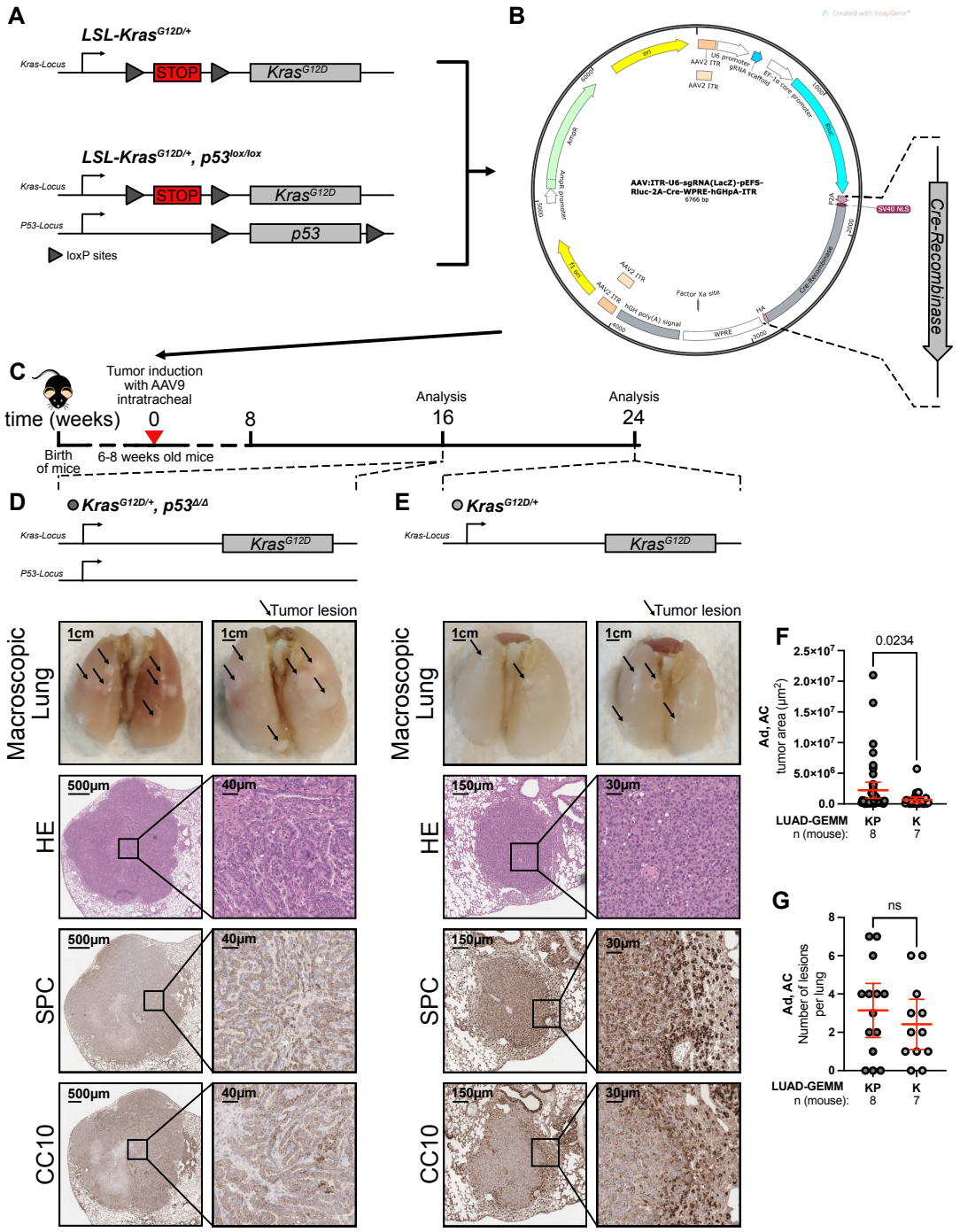

Figure 7: Validation and comparison of Kras$^{G12D/+}$ (K) and Kras$^{G12D/+}$; p53$^{lox/lox}$ (KP) mice. (A-E): Experimental design and timeline of LUAD mice showing genetic changes after AAV9 application subsequently activating LUAD driving mutations. (A) Modified genetic background of both investigated LUAD mouse models. K-LUAD: Lox-STOP-Lox-Kras$^{G12D/+}$ and KP-LUAD: Lox-STOP-Lox-Kras$^{G12D/+}$; p53$^{lox/lox}$. (B) Plasmid used to provide a Cre-Recombinase to initiate LUAD driver mutations. The sgLacZ-pLUAD sequence was AAV: ITR-U6-sgLacZ-pEFS-Rluc-2A-Cre-WPRE-hGHpA-ITR and the backbone was gifted from Feng Zhang (Addgene plasmid #60226; http://n2t.net/addgene:60226; RRID:Addgene_60226) (Platt et al., 2014). (C): Experimental timeline of mice showing intratracheal AAV9 application at 6-8 weeks after birth and analysis at 16 weeks post-infection for KP-LUAD mice or at 24 weeks for K-LUAD mice. (D) Genomic changes after AAV9 application in KP-mice leading to Kras$^{G12D/+}$; p53$^{Δ/Δ}$, and in K-mice to Kras$^{G12D/+}$. Whole lungs showing macroscopic tumor lesions marked by arrows. Representative HE-staining of LUAD lesions for validation of the histopathology of lung adenocarcinoma (LUAD) by morphological characteristics described from Nikitin et al. (Nikitin et al., 2004). Representative immunohistochemistry staining for CC10 and SPC to analyze marker proteins for LUAD cells of origin and verify adenomatous lesions, as published by Jackson et al. (Jackson et al., 2001). Image scales reporter in each figure. (F-G): Comparison of K- and KP lung adenoma (Ad) and lung adenocarcinoma (AC) by tumor area (F) and number of lesions per lung (G). Data are presented as mean ± SD and were analyzed by Mann-Whitney test for tumor area and unpaired t-test for number of lesions per lung. Number (n) of analyzed animals and p-values are reported in the figures.

4.4 Advanced LUAD in K- and KP-LUAD mice is associated with reduced *Ripk3* expression.

We hypothesized that LUAD tumors depress *Ripk3* during tumorigenesis to escape necroptotic cell death and survive tumor-induced stress. This hypothesis was evaluated in *Ripk3* competent LUAD mice, in which changes of *Ripk3* expression were analyzed by IHC-staining of the RIPK3 protein (see chapter 3.7). We thereby investigated RIPK3 staining intensities across different LUAD tumor stages: less dysplastic bronchial hyperplasia proceeding to more advanced atypical adenomatous hyperplasia (AAH) and subsequently to dysplastic adenoma, adenocarcinoma (Ad, AC). This process was further described as LUAD tumorigenesis (Figure 8 A).

In K- (Figure 8 B) and KP-LUAD mice (Figure 8 C) early-stage lesions (Bronchial hyperplasia) with strong RIPK3 staining intensities were more prevalent than lesions with weak RIPK3 staining intensities and therefore most lesions showed high RIPK3 protein levels. Advanced stage tumors (adenoma and adenocarcinoma; Ad, AC) had mostly weak RIPK3 staining intensities and less strong staining intensities. These findings depict a decrease of the RIPK3 protein level in advanced tumor lesions suggesting a tumor-mediated downregulation of RIPK3 expression.

Comparing staining fractions across tumor stages showed that less dysplastic BH had the biggest proportion of lesions with strong staining intensities (Figure 8 B, C: 37% in K- and 58% in KP-LUAD mice), which was reduced in adenoma and adenocarcinoma (Figure 8 B, C: 15% in K- and 8% in KP-LUAD mice). Ad, AC lesions showed the biggest proportion for tumor lesions with weak staining intensities (41% of K- and 64 % of KP-mice).

Overall, we found decreased RIPK3 protein levels in advanced LUAD lesions, both in K- and KP, further highlighting a reduction of RIPK3 expression during tumorigenesis. These results suggest that tumor driven RIPK3 downregulation is critical for tumorigenesis and leads to survival advantages, due to the inhibition of necroptotic cell death.

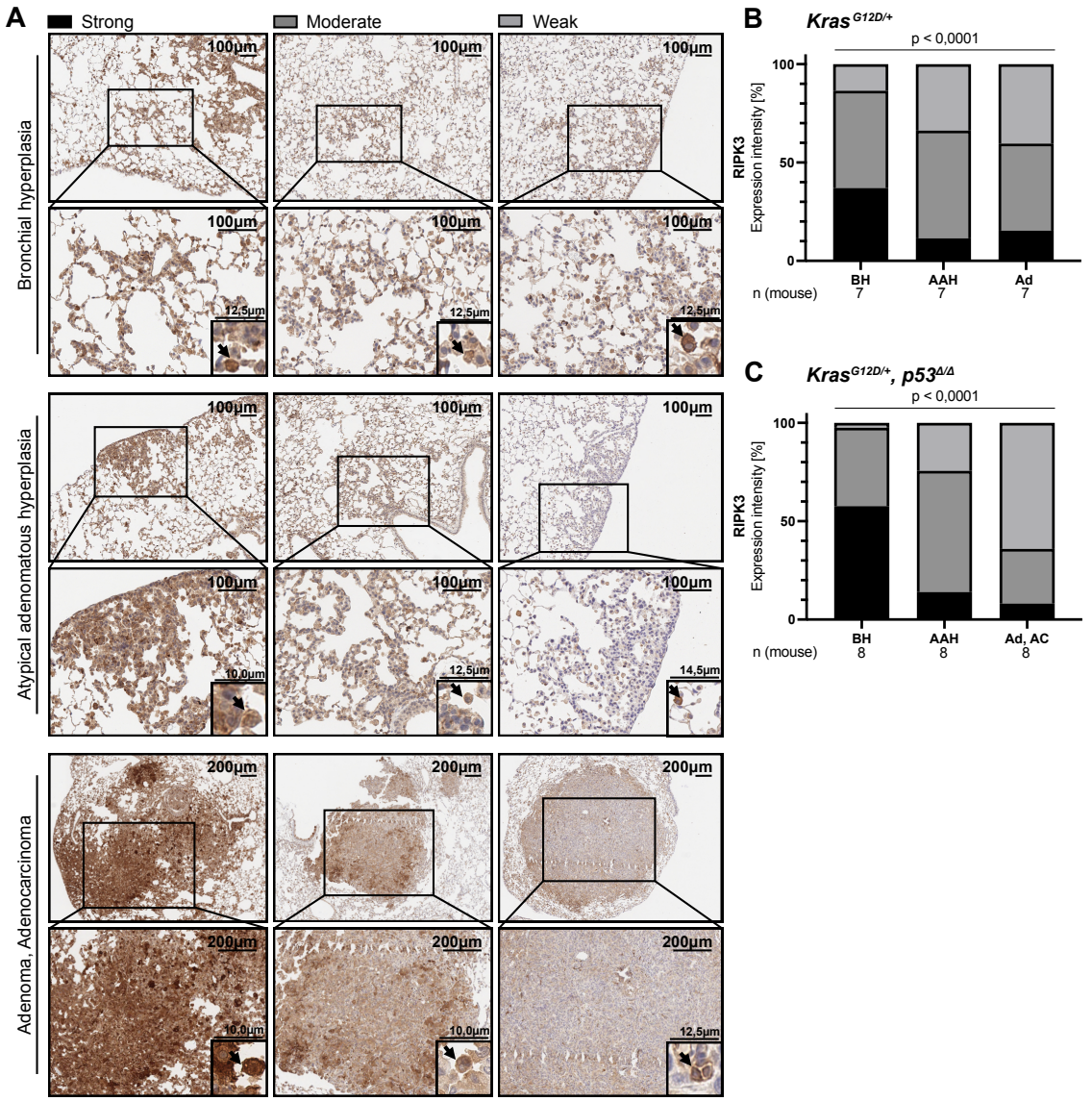

Figure 8: RIPK3 reduction in advanced lesions from Kras^{G12D}; and Kras^{G12D}; p53$^{\Delta/\Delta}$ mice. (A): Representative images of RIPK3 staining in lung tumors from experimental animals. RIPK3 staining intensity was assessed and classified as weak, intermediate, or strong using the macrophage (➘) staining intensity as positive control. (BH: bronchial hyperplasia; AAH: atypical adenomatous hyperplasia; Ad, AC: adenoma and adenocarcinoma; arrows indicating macrophage staining control). Image scales are reported in each panel. (B-C): Quantification of RIPK3 staining intensities in Kras^{G12D} LUAD mice (n=7) and Kras^{G12D}; p53$^{\Delta/\Delta}$ LUAD mice (n=8). Every lesion was classified by staining intensity and tumor stage in a double blinded approach from two independent experimenters. Data were analyzed by chi-square test and p-values are shown in the figures.

4.5 Decreased *Ripk3* expression in K- and KP-LUAD mice promotes tumor progression

In *Ripk3* competent LUAD mice, the interaction between RIPK3 levels and tumor progression was analyzed by comparing tumor sizes of lesions with RIPK3 strong and weak staining intensities. The expression levels of RIPK3 in LUAD lesions were detected by staining intensities, as previously described in chapter 3.7.2. Lung adenomas and adenocarcinomas with strong and weak RIPK3 IHC-staining were analyzed to determine the tumor area by Tissue IA image analysis from Slidepath.

In K-LUAD mice, the average tumor area of all LUAD lesions showing strong RIPK3 IHC staining was significantly lower than the average size of LUAD lesions having low RIPK3 staining intensities (Figure 9 A, B). Further, the 5 most advanced lesions of each group were growing larger if RIPK3 was not or weakly detectable (Figure 9 C) and smaller if RIPK3 was strongly present. This difference in size depending on the presence of RIPK3 was not significant in the smallest 5 LUAD lesions of each group (Figure 9 D). The presence of RIPK3 was correlating with smaller tumor areas suggesting a tumor suppressive effect.

In KP-LUAD mice, the average tumor area of lung adenomas and adenocarcinomas with weak IHC-RIPK3 staining was bigger than tumor lesions with strong RIPK3 staining intensities (Figure 9 F). This was also the case for comparing the 5 most advanced and therefore biggest lesions of each group (Figure 9 G) and the 5 less advanced LUAD lesions of each group (Figure 9 H). These results are in line with the K-LUAD mouse model.

$Kras^{G12D/+}$ as well as $Kras^{G12D/+}$, $p53^{\Delta/\Delta}$ driven lung adenomas and adenocarcinomas showed smaller tumor sizes if RIPK3 was highly expressed. This phenotype was suspected for RIPK3, as it mediates stated tumor suppressive effects by inducing necroptotic cell death in LUAD.

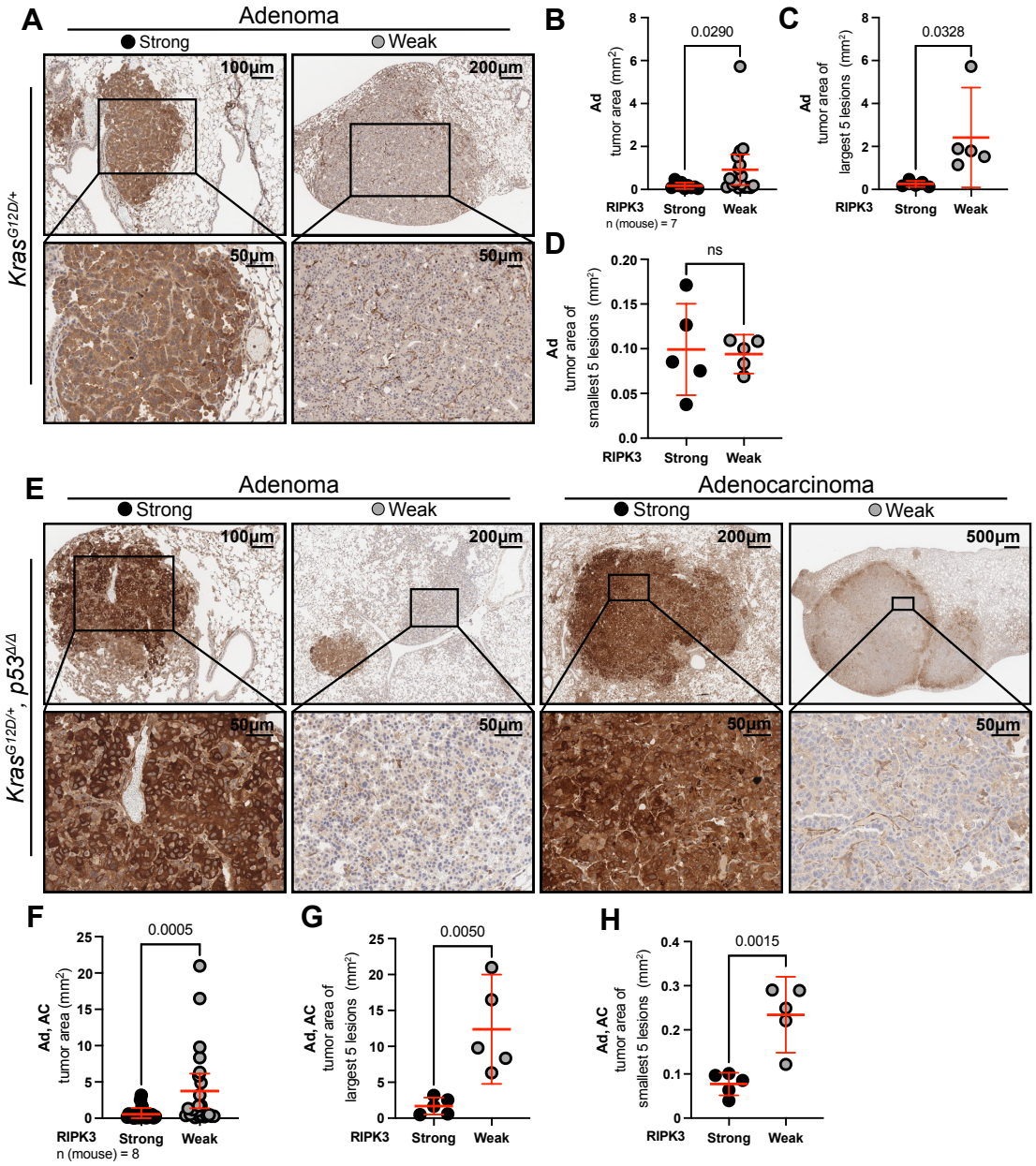

Figure 9: High RIPK3 expression correlates with decreased tumor sizes in LUAD mice. (A): Representative images of adenoma (Ad) in $Kras^{G12D}$ LUAD mice (K-LUAD) with strong and weak RIPK3 expression quantified by RIPK3 IHC-staining intensities. Image scales are shown in each panel. (B-D): Quantification of the tumor area of each lesion classified as strong or weak for RIPK3 expression. Comparison of all strong and weak lesions (B) as well as the five biggest (C) and five smallest (D) lesions of each group. (E): Representative images of adenoma and adenocarcinoma (Ad, AC) in $Kras^{G12D}$; $p53^{\Delta/\Delta}$; LUAD mice (KP-LUAD) with strong and weak RIPK3 expression quantified by RIPK3 IHC-staining intensities. Image scales are shown in each panel. (F-H): Quantification of the tumor area of each lesion classified as strong or weak for RIPK3 expression. Comparison of all strong and weak tumors (F) as well as the five biggest (G) and five smallest (H) of each group. Number (n) of investigated mice and p-values are shown in each figure. Data are presented as mean ± SD and were analyzed by Mann-Whitney test for panel B and F, and unpaired t-test for C, G and H.

4.6 KP LUAD mice recruits antitumoral iNOS-positive macrophages (M2)

Necroptosis triggers inflammation by the release of cytokines and intracellular DAMPs as well as TAAs. It was suggested that this inflammatory profile of necroptosis attracts immune cells to necroptotic tumor cells, which may further have an antitumoral function. To investigate this hypothesis, we tracked tumor infiltrating immune cells by IHC-staining and calculated the positive staining area of immune cells per total tumor area using positivity scores from Tissue IA image analysis from Slidepath (see chapter 3.7.4). Immune IHC analysis were restricted to the KP-LUAD mouse because of the dominant fraction of Ad, AC lesions.

LUAD lesions on RIPK3-IHC slides having either strong or weak staining intensities were matched to the same lesions on immune IHC slides to calculate the presence of CD3/CD8 T-cells and macrophage phenotypes in each tumor area. The presence of immune cells in the tumor area was calculated by positivity scores (positive pixel area per total tumor area). Tumor lesions with previously evaluated RIPK3 intensities were excluded if the tumor area on RIPK3-IHC slides could not be matched to the same tumor area on immune IHC-slides. For CD3-IHC staining one mouse had to be excluded because of poor staining quality.

For CD3 and CD8 T-cells the positivity scores between LUAD lesions showing strong or weak RIPK3 staining were not significantly different (Figure 10 A-D). Macrophages had equal positivity scores for F40/80 and Arginase 1 positive (M1) macrophages, but the positivity score for iNOS positive (M2) macrophages was significantly higher in RIPK3 high lesions (Figure 10 E-J).

Therefore, no cytotoxic T-cell enrichment depending on RIPK3 expression could be detected in RIPK3 competent KP-LUAD mice. Pro-tumoral M1- macrophages characterized by being Arginase-1 positive were present in tumor areas independent of RIPK3 expression. The antitumoral M2 phenotype identified by iNOS positive macrophages was enriched in high RIPK3 tumor areas. RIPK3-dependent necroptosis may be recruiting antitumoral M2 macrophages in the tumor immune microenvironment without attracting cytotoxic T-cells.

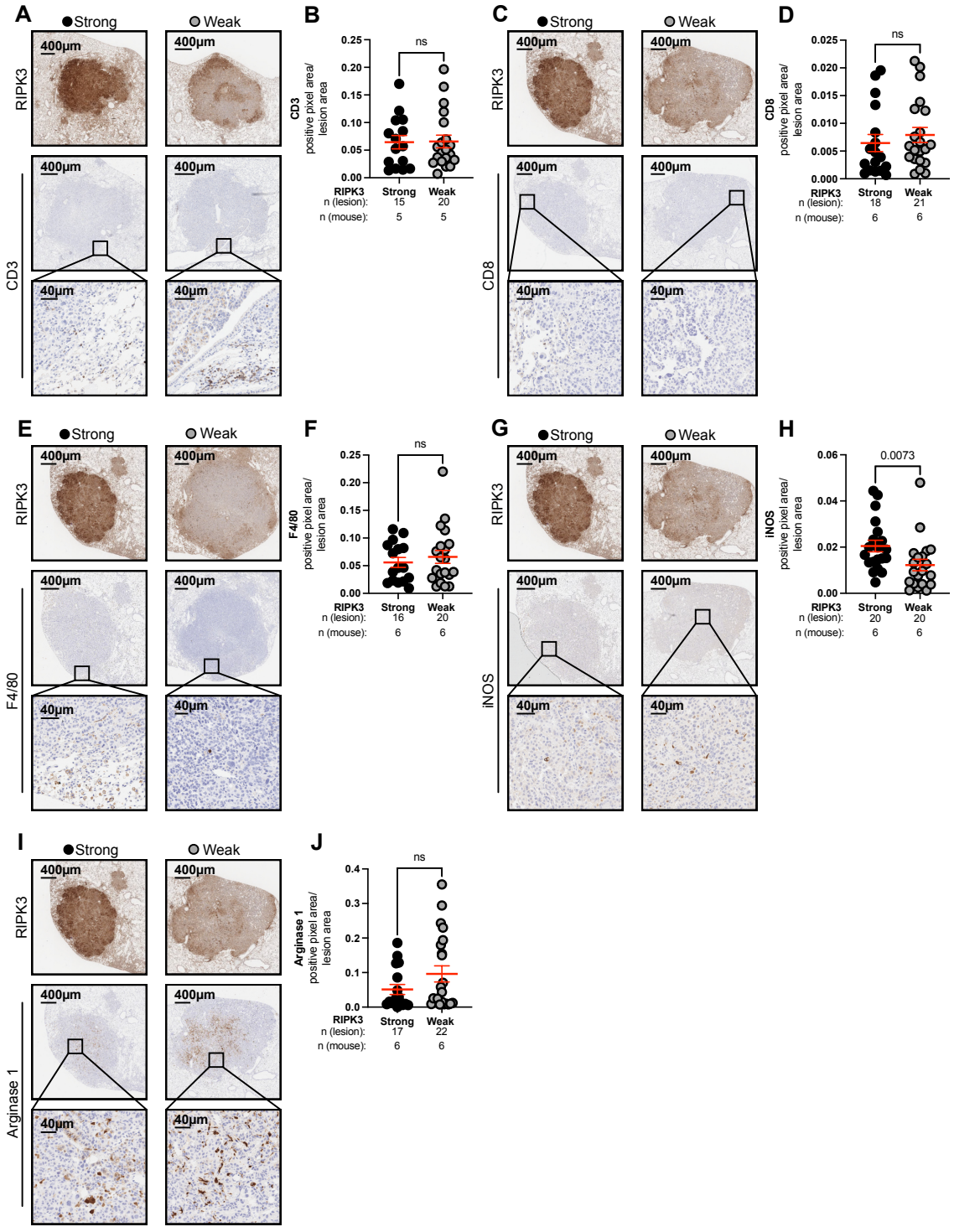

Figure 10: High RIPK3 expression correlates with increased intratumoral iNOS positive macrophages in Kras^{G12D}; p53$^{\Delta/\Delta}$ LUAD mice. (A-J): Representative images of LUAD lesions showing RIPK3 IHC-staining to assign adenoma and adenocarcinoma into strong and weak RIPK3 lesions and immune IHC-staining to mark intratumoral immune cells. Scales are shown in each image. The presence of immune cells was calculated by positivity scores (staining positive pixel area per lesion area). Data were analyzed with Mann-Whitney tests and are presented with mean ± SEM. Number (n) of investigated mice and p-values are shown in each panel. Evaluated immune subgroups were CD3 positive T-cells (A, B), CD8 positive T-cells (C, D), F4/80 positive macrophages (E, F), iNOS positive macrophages (G, H) and Arginase-1 positive macrophages (I, J).

4.7 High RIPK3 expression is associated with antitumoral macrophage polarization.

To get a hint if RIPK3-mediated necroptosis and its inflammatory nature changes macrophage phenotypes in the tumoral immune microenvironment, we took advantage of Arginase-1 and iNOS IHC-staining on lesions assigned to RIPK3 strong or weak expression groups. We used iNOS staining as a marker for antitumoral macrophages (M2 phenotype) and Arginase-1 staining to detect pro-tumoral macrophages (M1 phenotype) (see chapter 1.4.3). The proportion of M1 to M2 macrophages was significantly different between tumor areas having strong or weak RIPK3 expression levels (Figure 11 A). Antitumoral M2 macrophages stained by iNOS were more prevalent in RIPK3 high LUAD lesions compared to RIPK3 weak lesions. The proportion of Arginase-1 positive M1 macrophages stated as pro-tumoral was higher in RIPK3 low expressing lesions (Figure 11 A-C). We found that RIPK3 was associated with an antitumoral macrophage polarization assuming to promote M2 macrophage recruitment.

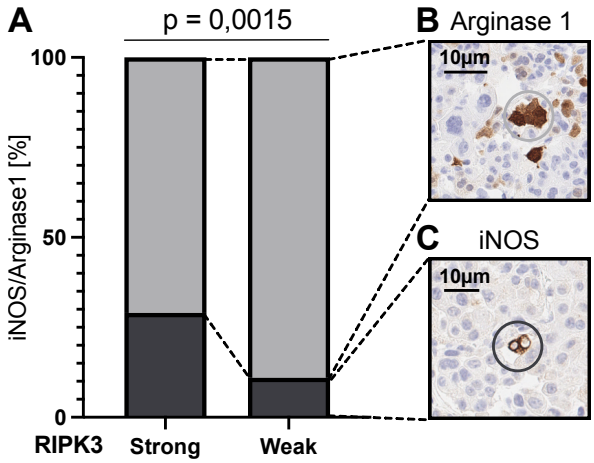

Figure 11: Increased RIPK3 expression mediates macrophage polarization to an antitumoral M2-phenotype. (A): Quantification of iNOS and Arginase-1 positivity in adenoma and adenocarcinoma with strong or weak RIPK3 expression. Positivity was calculated by positive pixel area per lung area. 6 mice were investigated. Data were analyzed by chi-square test and p-value is shown in the figure. (B, C): Images representing IHC-staining of Arginase-1 positive macrophage (B) and iNOS positive macrophage (C). Scale bars are shown in each panel.

4.8 Characterization of the necroptotic pathway axis RIPK1-RIPK3-MLKL in human NSCLC-LUAD cell lines

In vitro experiments with human lung adenocarcinoma cell lines were performed to demonstrate that necroptosis is a functional cell death pathway in human lung adenocarcinoma, which is pharmaceutically inducible and moreover relevant for chemotherapeutic drugs used in treatment regimes.

A possible mechanism to overcome necroptotic cell death in LUAD cells could be the down regulation of the key necroptotic proteins, *RIPK3*, *RIPK1,* and *MLKL* (Figure 12 A). We initially evaluated RIPK3 protein levels on western blots, in which we used a RIPK3 knockout sample as negative control and human bronchial epithelial cells (HBECs) as positive control. We observed heterogenous RIPK3 protein expression levels across different cell lines, which we further

grouped in low RIPK3 expressing (weaker band than HBEC, like RIPK3 knockout): H23, H358, A549 and medium, high RIPK3 expressing (band density similar or stronger than for HBECs): HCC44, H1437, H1650, H1975, H2087, H2126 (Figure 12 B).

We further investigated normalized mRNA levels in LUAD cell lines using qRT-PCR to measure *RIPK1*, *RIPK3*, and *MLKL* levels (FC = fold change).

We also analyzed TNF-receptor (*TNFR1* and *TNFR2*) mRNA levels to investigate whether the TNF receptor is transcribed and possibly accessible to initiate necroptosis. We found detectable *TNFR1* and *TNFR2* mRNA levels throughout all cell lines (Figure 12 C), except for HCC44, A549, and H1975, which showed low to non-detectable *TNFR2* mRNA levels (Figure 12 D). Because either or both TNF-receptors were present in all cell lines, we assumed that TNF induced necroptosis can be pharmaceutically activated by TNF-receptor agonists. TNF-signaling is known to activate necroptosis among other cell death pathways, in particular apoptosis.

We further analyzed *RIPK1* normalized mRNA levels to show that the necroptosis initiating element, which recruits RIPK3 by oligomerization can be detected in all used cell lines. *RIPK1* mRNA reached high levels for H358, H1437 and H2126 comparing to remaining NSCLC cell lines, which also had detectable *RIPK1* mRNA levels (Figure 12 E).

The necroptosis key regulator RIPK3 showed heterogenous levels, similar to what observed on a protein level. Absent or low mRNA *RIPK3* levels were detected for H23, HCC44, A549, and H1650. A medium and high *RIPK3* mRNA expression was found in H1975, H2126, H358, H1437, and H2087 (Figure 12 F). Comparing these *RIPK3* mRNA levels with the detected protein levels confirmed low RIPK3 expression for H23 and A549 and high RIPK3 expression for H1437, H1975, H2087, H2126.

HCC44 and H1650 showed low mRNA levels and high protein levels, H358 high mRNA levels and low protein levels. Both observations were not in line with the central dogma of protein expression (mRNA transcription leading to protein translation). Therefore, additional mechanisms impacting mRNA or protein expression were assumed, but not pursued by us on further validations (Figure 12 B, F).

MLKL mRNA levels were detectable in all cell lines and reached high levels for H1437 and low levels for H23 (Figure 12 G).

Taken together, these data suggested a highly expressed necroptotic pathway (RIPK1-RIPK3-MLKL axis) in the cell line H1437 with high normalized mRNA levels for *RIPK1*, *RIPK3* and *MLKL* and a suppressed necroptotic pathway in H23 with low mRNA levels for *RIPK1*, *RIPK3* and *MLKL* and a low RIPK3 protein level. These phenotypes were further investigated in functional analysis, in which necroptosis was pharmaceutically induced.

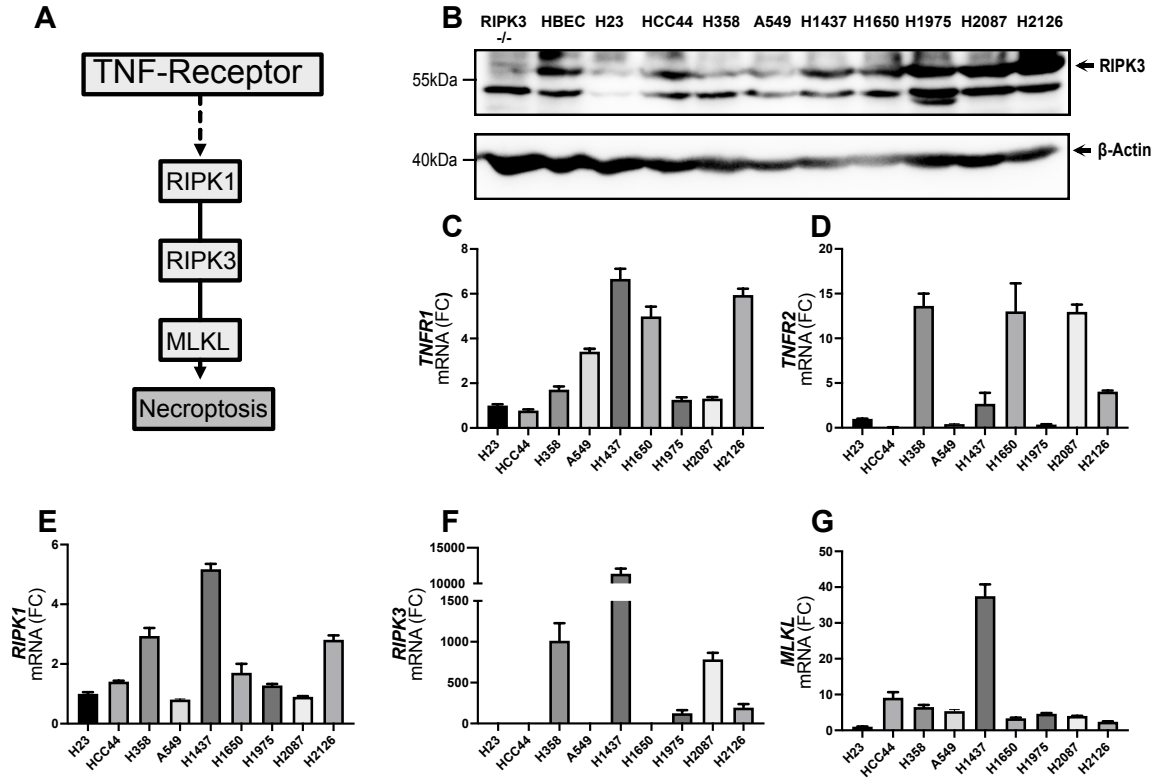

Figure 12: Characterization of necroptosis by analyzing the RIPK1-RIPK3-MLKL axis in NSCLC- LUAD cell lines. (A): Schematic illustration of the TNF induced RIPK1-RIPK3-MLKL axis initiating necroptotic cell death (B): Representative western blot for analyzing RIPK3 protein levels among 9 NSCLC-LUAD cell lines. RIPK3 knockout samples (RIPK3$^{-/-}$) were used as negative control and RIPK3 reference expression was investigated by non-malignant human bronchial epithelial cells (HBECs). Molecular weight markers (kDa) and β-actin control are reported in the figure. (C-G): QRT-PCR determining mRNA levels presented as fold change (FC) to H23 mRNA levels for *TNFR1* (C), *TNFR2* (D), *RIPK1* (E), *RIPK3* (F) and *MLKL* (G) across 9 NSCLC-LUAD cell lines reported in each panel. Data presented as mean ± SEM.

4.9 TNF-agonists initiates apoptotic and necroptotic cell death in LUAD cell lines

We activated TNF dependent cell death in LUAD cell lines with TNF-agonists (recombinant human tumor necrosis factor-α) and SMAC-mimetics (Second mitochondria derived activator of caspase). Thereby, we validated the functional consequence of differently expressed RIPK1-RIPK3-MLKL axis by inducing cell death *in vitro*. Activation of the TNF-receptor initiates the downstream cell death cascades, which in a caspase-dependent manner induces apoptosis or, in the absence of caspases, initiates RIPK3 dependent necroptosis. SMAC mimetics were used to inhibit IAP-family members (inhibitors of apoptosis proteins) and sensitized LUAD cell lines to TNF mediated cell death. Apoptosis was induced by applying TNF and SMAC mimetics to NSCLC cell culture media (TS-treatment group) and further reversed with a pan-caspase inhibitor: carbobenzoxy-valyl-alanyl-aspartyl-[O-methyl]- fluoromethylketone (Z-VAD-FMK). Caspase inhibition shifted TNF induced apoptosis towards necroptosis, which was activated by treating NSCLC cell cultures with TNF, SMAC-mimetics, and Z-VAD-FMK (TSZ-treatment group). Necroptosis was inhibited by the RIPK1 inhibitor Necrostatin-1s (Nec1s, TSZ-Nec1s treatment group) (Figure 13 A). We analyzed human LUAD cell lines for necroptosis induction by measuring cell death with ATP-release assays (Cell Titer-Glo®). We initiated necroptosis by

previously described TSZ treatment and compared the viability signal with untreated DMSO control cultures. After 72 hours of incubation with TSZ treatment, we observed significantly reduced viable cells compared to control cultures for the human LUAD cell lines H23, H1437, and H1975 and a not-significant reduction for HCC44, H358, A549, H1650, H2087 and H2126 (Figure 13 B). These results suggested that H23, H1437 and H1975 are necroptosis competent cell lines. Interestingly, H1437 cells were the most susceptible to necroptosis induction by TSZ treatment, this is in line with the previously reported data, showing for H1437 the highest mRNA levels of the necroptotic machinery (see chapter 4.8).

To further elucidate the capability to undergo apoptosis or necroptosis in human LUAD cell lines, we induced apoptosis with TS and necroptosis with TSZ treatment regimes. The LUAD cell lines H23 and A549 did not show a significant reduction of viable cells by applying TS or TSZ reagents compared to their DMSO control and therefore were not susceptible to either TNF-induced apoptosis or necroptosis (Figure 13 C, D). These results were in line with previously shown low mRNA levels of key proteins in the necroptotic machinery and supported our conceptual hypothesis. In H23, we were initially able to induce a significant reduction of viable cells via TSZ treatment but could not reproduce this result in three independent experiments. We therefore stated H23 as necroptosis non-competent (Figure 13 B, C).
In the cell lines HCC44, H1975 and H2126 we observed a significant reduction of viable cells in the apoptotic TS treatment group. This cell death signal was reversed by adding Z-VAD-FMK, which rescued from apoptotic cell death by inhibiting caspases. Moreover, TSZ did not induce necroptotic cell death suggesting a restriction to apoptosis (Figure 13 E-G).
In H1437 cell cultures TS treatment did not show a significant induction of cell death, but the TSZ treatment significantly reduced the number of viable cells in H1437 cell cultures. Occurring cell death in the TSZ treatment group was reversed by adding Nec-1s, suggesting a restriction to TNF-dependent necroptosis in H1437 (Figure 13 H). These results confirmed an inducible necroptotic pathway in H1437, which was assumed because of high *RIPK1*, *RIPK3* and *MLKL* normalized mRNA levels and TSZ dependent necroptosis induction.
In H2087, both TS and TSZ treatment showed a significant reduction in viable cells compared to the DMSO control group. In the TSZ treated culture, caspase inhibition did not show a rescue from apoptotic cell death, which instead was rescued by Nec-1s treatment and suggested a predominant induction of necroptosis.

Taken together, these results showed that TNF dependent necroptosis is a relevant cell death pathway in a subgroup of human LUAD cell lines, such as H1437 and H2087. Interestingly, necroptosis was inducible even in apoptosis-resistant cell lines. This could outline a relevant cell death pathway to bypass known apoptosis resistance mechanisms in LUAD (Munkhbaatar et al., 2020).

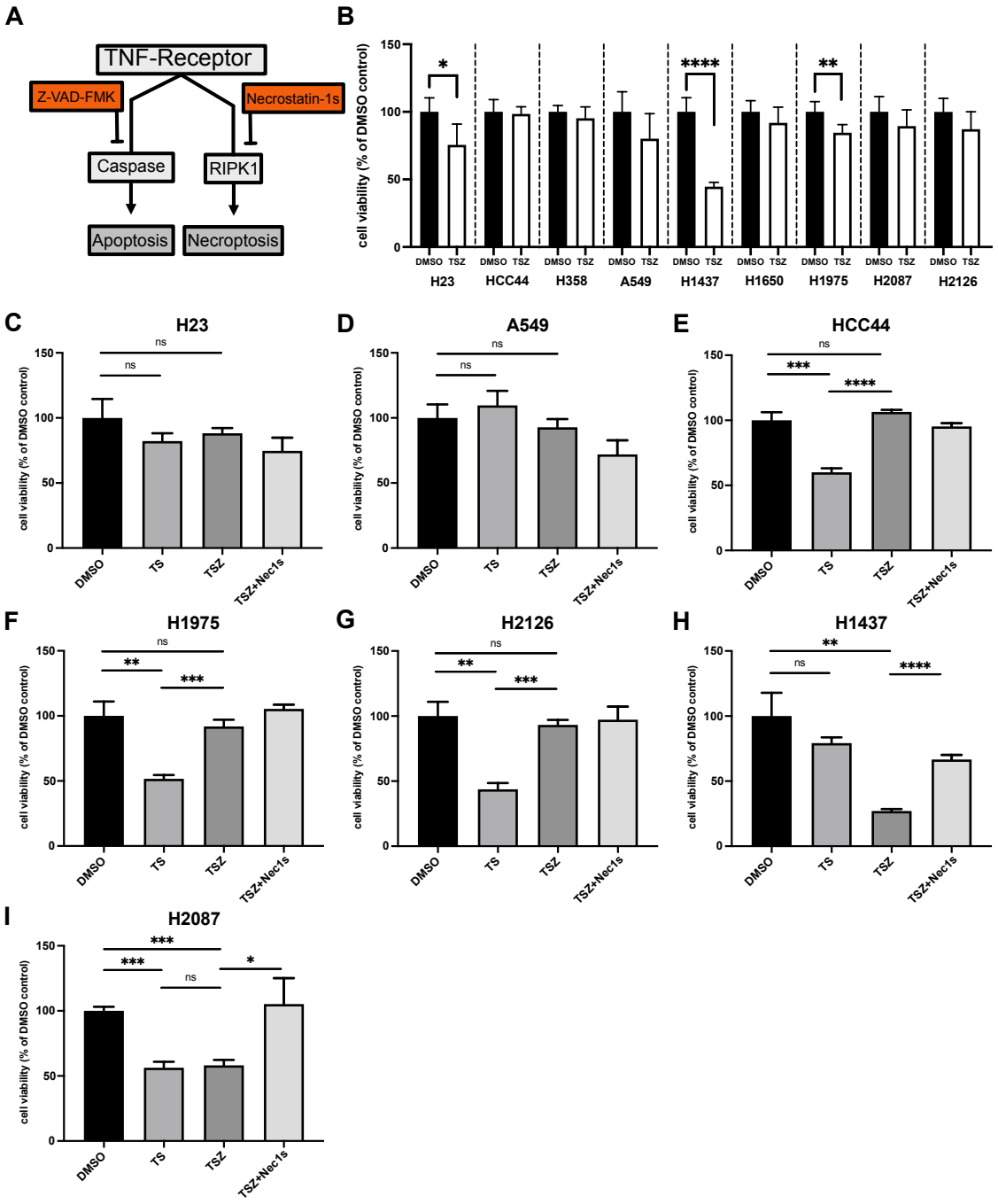

Figure 13: Functional analysis of TNF-induced apoptosis and necroptosis in NSCLC-LUAD cell lines. (A): Schematic illustration of proteins mediating TNF induced apoptosis (caspase) and necroptosis (RIPK1), which were further pharmaceutically inhibited to reverse apoptosis (Z-VAD-FMK) and necroptosis (Necrostatin-1s). (B-I): NSCLC cell lines treated as reported (T = TNF-α [100ng/µl], S = SMAC mimetics [1µM], Z = Z-VAD-FMK [50µM], Nec1s = Necrostatin-1s [10µM]). Cell viability measured by detection of ATP levels after 72 hours. Data presented as mean ± SEM and analyzed by unpaired t-test (ns p>0,05; *p≤0,05; **p≤0,01; ***p≤0,001; ****p≤0,0001).

4.10 Chemotherapeutic titration for efficient cell death induction

To evaluate if necroptosis is a relevant pathway for chemotherapy induced cell death in human NSCLC-LUAD cell lines, we investigated different chemotherapeutics and their effect on cell death initiation with or without apoptosis or necroptosis inhibition. Therefore, we cultured H1437 cells, which showed a necroptotic signature by TNF activation and HCC44 cells, which showed an apoptotic signature by TNF activation. As a control cell culture, we used H23 cells, which showed no apoptotic or necroptotic cell death after treatment with TNF- regimes (see chapter 4.8, 4.9). We further assumed that chemotherapeutic induced necroptosis relies on executive signaling proteins in particular the RIPK1-RIPK3-MLKL axis similar to previously studied TNF induced necroptosis. We initially titrated eight chemotherapeutics using different concentrations for all three cell lines. We aimed to identify concentrations with efficient cell death induction and chemotherapeutics differing between investigated cell lines further favoring necroptosis competent or apoptosis competent cells.

All chemotherapeutic drugs were able to induce cell death in all the used human NSCLC-LUAD cell lines. For platin derivates cisplatin, carboplatin, and oxaliplatin, we did not observe a consistent difference of induced cell death levels between treated cell lines. This was as well the case for etoposide, gemcitabine, and vinorelbine (Figure 14 A-F). We assumed that these chemotherapeutic drugs were equally effective in activating apoptosis, necroptosis or cell death pathways not further discriminated.

In the paclitaxel and pemetrexed (Figure 14 G, H) treatment groups, we observed a consistently reduced ability to induce cell death in H23 compared to H1437 and HCC44. We have previously shown that H23 had lower susceptibility to TNF-induced cell death, thus we could assume that these pathways may be relevant in these therapeutic approaches. Paclitaxel was consistently more effective in inducing cell death in the H1437 cell line compared to the HCC44 cell line. This could relate to the increased necroptotic activity of H1437, which may undergo cell death more efficiently after paclitaxel treatment than the apoptotic competent cell line HCC44.

Taken together these data suggest that necroptotic competent cells are more susceptible to paclitaxel treatment. In pemetrexed treated cultures the induction of cell death in H1437 and HCC44 was not different for lower concentration regimes. For higher concentrations (> 5µM), the induction of cell death by pemetrexed was more effective in H1437 cell cultures. This suggests that apoptosis as well as necroptosis might contribute equally to an efficient cell death induction of pemetrexed.

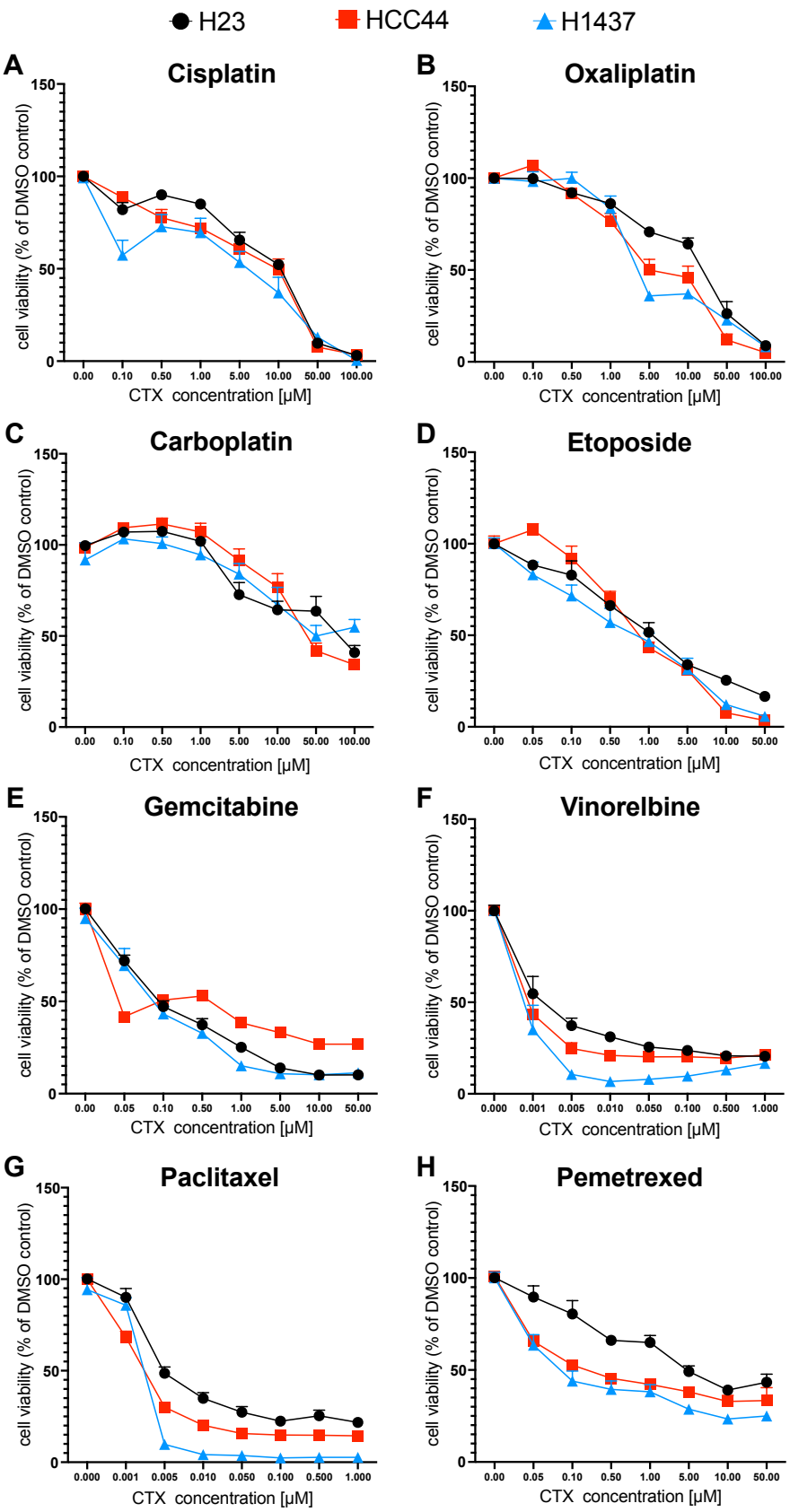

Figure 14: Titration curves of chemotherapeutic drugs in human NSCLC-LUAD cell lines. (A-H): Titration curves of cell cultures incubated with chemotherapeutic drugs in different concentrations for 72 hours. Cell viability measured by detection of ATP levels. Drug names, drug concentrations and cell lines as reported in each panel. Data points for each concentration are shown by mean ± SEM.

Based on the titration curves we chose effective drug concentrations for cisplatin, paclitaxel, and pemetrexed to further characterize cell death mechanisms.

We analyzed cisplatin because of chemotherapeutic regimes in NSCLC are often platin-based and we also used it as internal positive control. We therefore chose a high concentration of cisplatin which showed a clear reduction of viable cells in the titration curves (50µM) (Figure 15 A). This concertation induced a similar reduction of viable cells in H23, H1437, and HCC44 cell cultures (Figure 15 B).

We investigated paclitaxel because the necroptosis competent H1437 cell line was consistently more vulnerable to this treatment (Figure 15 C). This suggested that necroptosis has a relevant impact on treatment efficiency. We used a concentration of 0,01 µM, which showed a potent induction of cell death by reducing viable cells in all three cell lines by more than 50% and showed the biggest difference of induced cell death between H23, H1437 and HCC44. Using 0,01µM of paclitaxel showed a significant cell viability reduction in H1437 and HCC44 cell cultures compared to a weaker reduction in H23. Moreover, viable cells of the H1437 culture were significantly more reduced than treated HCC44 cells (Figure 15 D). We assumed that paclitaxel induced cell death benefits from a highly expressed necroptotic machinery.

Furthermore, we analyzed pemetrexed treatment groups, which had a continuously higher reduction of viable cells in H1437 and HCC44 cell cultures compared to H23 cultures (Figure 15 E). For further experiments we used a concentration of 1µM, which induced a strong reduction of viable cells in all three cell lines and showed the biggest difference between H23 and HCC44/H1437. Treating all three NSCLC-LUAD cell lines with 1µM pemetrexed induced a significant reduction of viable H1437 and HCC44 cells compared to H23 cells. This reduction was further equal for HCC44 and H1437, which suggests that both apoptosis and necroptosis may be induced by pemetrexed (Figure 15 F).

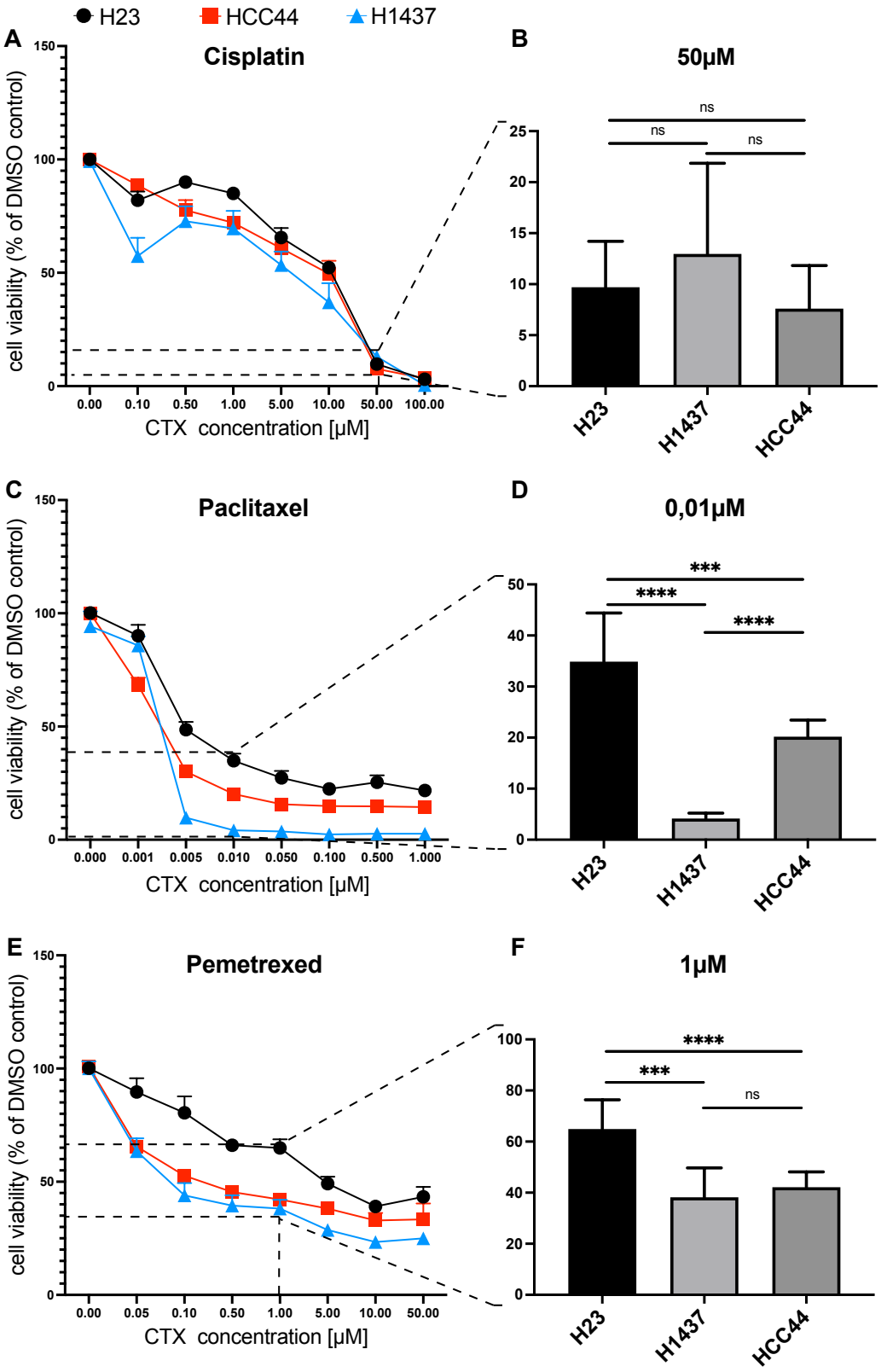

Figure 15: Validation of effective drug concentrations to elucidate induced necroptosis or apoptosis. (A-F): Cisplatin, pemetrexed, and paclitaxel titration curves for shown concentrations and comparison of cell viability for one chosen concentration of each drug reported in each panel. Cell viability measured by ATP detection and normalized to DMSO control cultures for each cell line. Each data point of titration curves is shown as mean ± SEM and by comparing chosen concentrations as mean ± SEM Data were analyzed by unpaired t-test and p-values are shown in each figure (ns $p>0,05$; ***$p\leq0,001$; ****$p\leq0,0001$).

4.11 Validation of chemotherapeutic induced apoptosis and necroptosis by flow cytometry

We analyzed cell death phenotypes in cisplatin and paclitaxel treated cell cultures by validating cell membrane characteristics known to occur in apoptosis or necroptosis. We therefore performed annexin V APC / PI flow cytometry analysis, in which annexin V APC detects phosphatidyl serin residues in the cell membrane showing high concentrations if apoptosis is activated. Propidium iodide is used to detect free DNA leaking out of cells, this often results from necrotic-like cell death, such as necroptosis and late apoptosis (Figure 16 A).

H23 cell cultures treated with cisplatin showed a dominant induction of apoptosis by increased annexin V signals. Cisplatin reduced viable cells to 23.3% after 48 hours of treatment compared to 95.6% of viable cells in the DMSO control culture. Apoptotic clusters increased after cisplatin treatment for 48 hours (75.1%) compared to apoptotic clusters in the DMSO control group (3.88%). The necrotic fraction with a low annexin V but high PI signal did not show a fractional increase. The same apoptotic signature was seen after 72 hours.
H23 treated with paclitaxel increased mainly the apoptotic fractions with a non-substantial increase of the necrotic cell fraction. Cisplatin and paclitaxel were therefore mainly inducing apoptosis in H23 (Figure 16 B).

In the H1437 cell line treated with cisplatin we observed a reduction of viable cells from 63.8% in the DMSO control group to 22.4% in the cisplatin treated group after 48 hours of incubation. Apoptotic cell fractions increased from 33.38% in untreated to 71,1% in treated cultures as well as the necrotic fraction from 2.85 % in untreated to 6.65 % in treated cultures. Both fractions have approximately doubled after 48 hours of cisplatin treatment. This was again the case after 72 hours. Apoptotic fractions increased from 15.9% in the DMSO control to 80,1% in cisplatin treated groups and necrotic cells increased from 2.62 % in the DMSO control to 5.17 % in cisplatin treated groups. These results showed that cisplatin dominantly induced apoptosis but also increased the necrotic fraction in H1437 cells.
In the paclitaxel treatment group 63.8% viable cells of the DMSO control were reduced to 11% in treated group after 48 hours. Of note, obtained reduction was more than half of the reduction in cisplatin treated cultures after 48 hours. The apoptotic fractions increased their size from 33,36% in the DSMO control group to 73% of the treatment group after 48 hours and the necrotic group increased from 2.85% of the untreated DMSO control to 16% of paclitaxel treated cells. Approximately the same fractional changes were observed after 72 hours. Therefore, paclitaxel treatment of H1437 induced apoptotic and moreover a dominant necrotic form of cell death. As H1437 was previously described as necroptosis sensitive it was assumed that necroptosis increases susceptibility to paclitaxel induced cell death (Figure 16 C).

Cisplatin treatment of HCC44 cells reduced 60,4% viable cells in the DMSO control to 34,5 % in the treatment group after 48 hours of incubation and 62.3% viable cells in the DMSO control to 13,9% in the treatment group after 72 hours of incubation. There was a dominant increase in the apoptotic fractions from 39,3% of the DMSO control to 62,2% in the cisplatin treatment group after 48 hours and from 37,1% in the DMSO control to 84.5 % in the cisplatin treatment group after 72 hours of incubation. The necrotic fraction weakly increased between DMSO control and treatment groups.

The same range of results were obtained for the paclitaxel treatment group, in which the apoptotic fraction showed a dominant increase after 48 and 72 hours compared to untreated cells. The necrotic fraction had no clear increase but showed a higher PI signal in the treatment groups. These results suggested that HCC44 cells favor apoptotic cell death induced by cisplatin and paclitaxel. This was in line with previous observations, in which TNF induced cell death in HCC44 relied on apoptosis and not on necroptosis (see chapter 4.9) (D).

Taken together, these results showed that apoptosis was the main cell death phenotype in HCC44 and H23. Only in the H1437 cell line, the necrotic cell death had a clear increase especially in the paclitaxel treatment, having a previously demonstrated capability to induce necroptosis (see chapter 4.9). These data confirmed that for H1437 cells the responses to chemotherapeutic treatments rely on the necroptosis pathway. Hence necroptosis is a relevant cell death pathway in therapeutic regimes, which induce executive proteins like the RIPK1-RIPK3-MLKL axis especially shown for paclitaxel induced cell death.

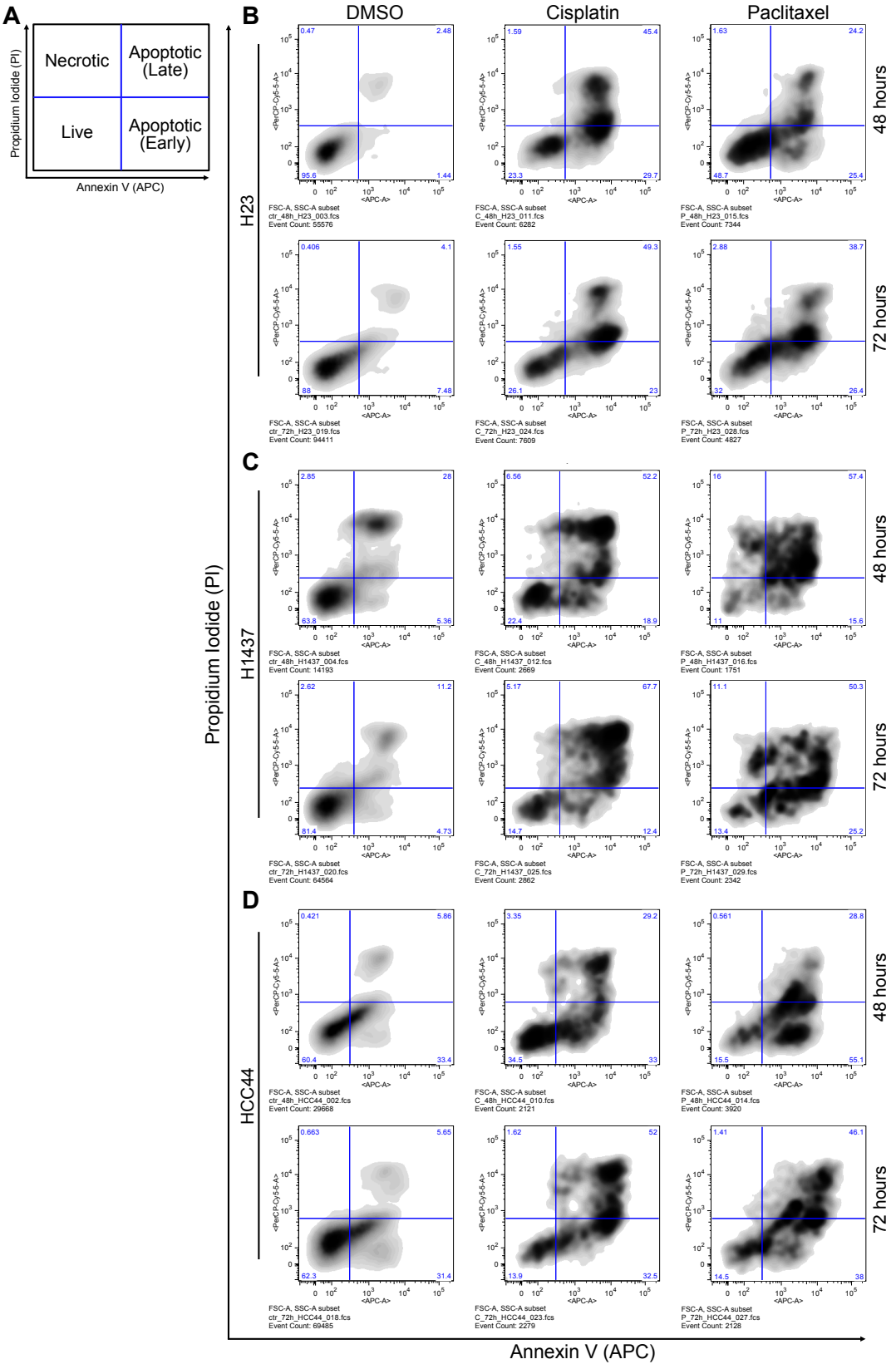

Figure 16: Analysis of chemotherapy induced cell death via annexin V-APC, PI flow cytometry. (A): Schematic illustration of the flow cytometry profile with APC staining on the x-axis and PI staining on the y-axis. Combined Annexin V/PI staining categorized detected cell signals in four quadrants to differentiate four phenotypes: necrotic cells, late apoptotic cells, early apoptotic cells, and viable cells. (B-D): Density blots showing the staining signals for APC and PI as density of dots on a grey scale. DMSO control or chemotherapeutic drug, investigated NSCLC-LUAD cell line and incubation time are shown in each panel. Proportion of cell counts for each phenotype are reported in the related quadrants.

4.12 Inhibition of apoptosis or necroptosis rescues from cisplatin, pemetrexed and paclitaxel induced cell death.

To elucidate whether chemotherapeutics, which showed different efficiencies in cell death induction for cell lines either favoring apoptotic or necroptotic cell death, do rely on apoptosis or necroptosis, we pharmaceutically antagonized either pathway by using Z-VAD-FMK, a pan-caspase antagonist, to inhibit apoptosis and Nec-1s, a RIPK1 antagonist, to inhibit necroptosis.

In the cisplatin treatment groups we observed a significantly reduced cell death induction if apoptosis was inhibited. This was the case for all three cell lines (H23, H1437 and HCC44) (Figure 17 A-C). Inhibition of necroptosis did not rescue from cisplatin induced cell death. These findings verify that cisplatin mainly induces apoptosis without a noticeable necroptotic pathway induction.

Pemetrexed induced cell death was reversed by either inhibiting apoptosis via Z-VAD-FMK or necroptosis by Nec-1s. Both pathway inhibitors significantly reduced the amount of dying cells in cultures of H23, H1437 and HCC44 (Figure 17 D-F). The combination of Z-VAD-FMK and Nec-1s showed the highest reduction of induced cell death in each LUAD cell culture. Therefore, the efficiency of cell death induction in LUAD cell lines treated with pemetrexed relied on apoptosis and necroptosis signaling pathways (Figure 17 D-F).

In the paclitaxel treatment groups the inhibition of apoptosis and necroptosis significantly rescued from induced cell death across all three cell lines (Figure 17 G-I). Z-VAD-FMK thereby showed a higher reduction of dying cells compared to treatments with Nec-1s. The combination of Z-VAD-FMK and Nec-1s had the biggest rescuing effect. These results showed that cell death induction by paclitaxel relied on functioning necroptosis and apoptosis.

Taken together these results underline that despite apoptosis, necroptosis is a relevant cell death pathway for therapeutic approaches because of increasing the efficiency of pemetrexed- and paclitaxel-initiated cell death in human NSCLC-LUAD cell lines.

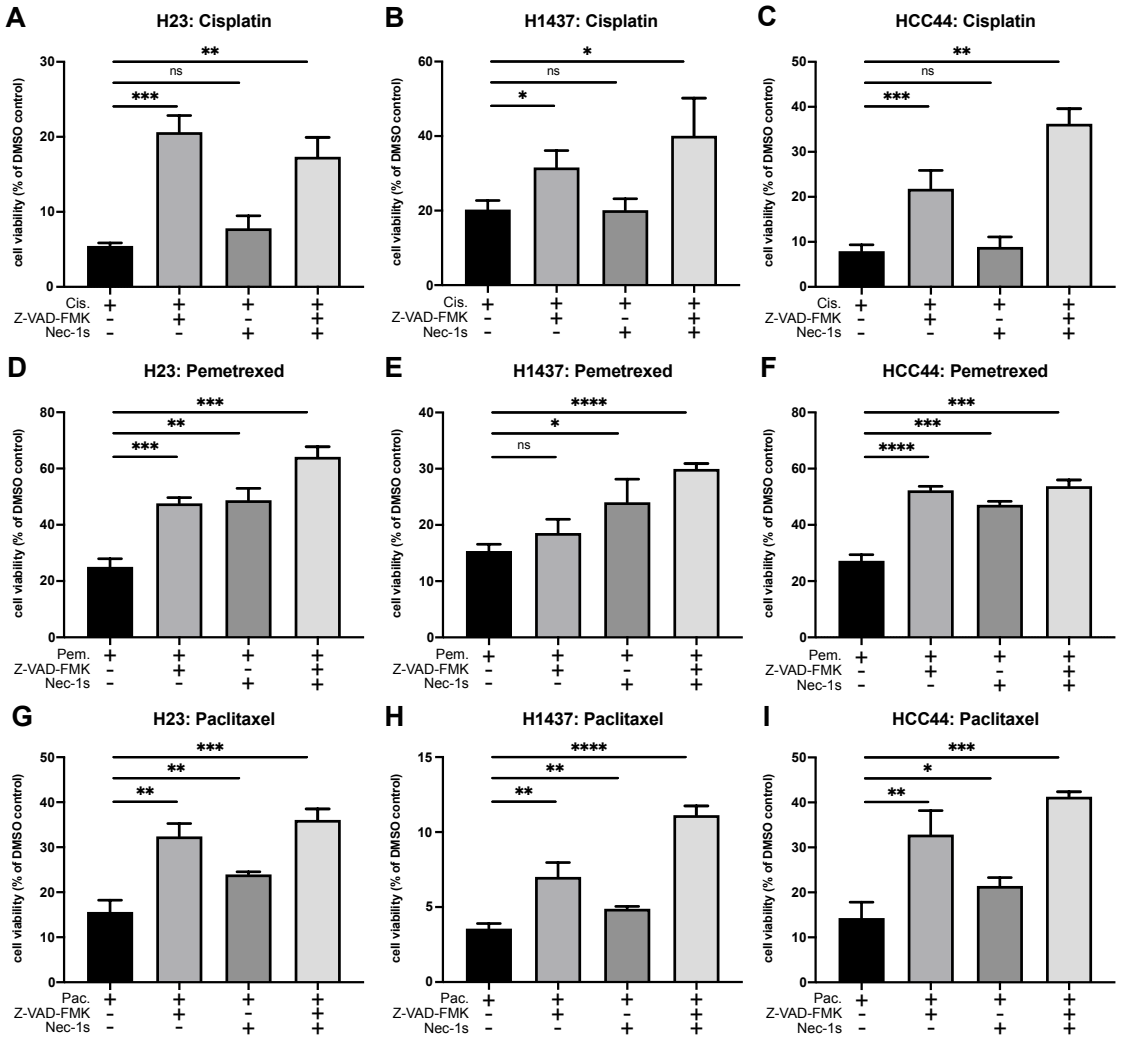

Figure 17: Inhibition of necroptosis or apoptosis reduced chemotherapy induced cell death. (A-I): Comparison of viable cells after treatment for 72 hours. Cell lines and treatment regimens as reported for each panel. Viable cells were detected by ATP-release assays (CellTiter-Glo) and normalized to untreated DMSO cultures. Experiments were performed in triplicates. Data are shown as mean ± SD and analyzed by unpaired t-tests. Significance is indicated by p-values in each figure (ns $p>0,05$; *$p\leq0,05$; ** $p\leq0,01$; ***$p\leq0,001$; ****$p\leq0,0001$).

5 Discussion

RIPK3 is the key regulating protein of necroptosis, the cell death pathway initiated by the RIPK1-RIPK3-MLKL axis. Necroptosis is a necrotic type of cell death and, as such, disrupts the cell membrane barrier, which delimitates cytosolic and extracellular contents, by increasing hydrogen influx due to membranous pore formation. Sustained cell swelling followed by membrane rupture and the release of cytosolic contents into the extracellular matrix establishes an inflammatory tissue environment. Necroptotic cells release immune cell recruiting signals, which in turn clear dead cell remnants and mediate immunogenic responses. Hence, if necroptosis induces immunogenic cell death in lung tumor tissue, immune cells may invade and recognize dead tumor cells by liberated antigens. Tumor primed effector cells might further attack tumor cells and clear remaining tumor tissue. This would be a novel tumor suppressive mechanism in lung cancer. Additionally, necroptosis might be a cell death cascade activated by chemotherapeutics, which would open the field for clinical studies.

The present doctoral thesis aimed to delineate the role of necroptosis in lung adenocarcinoma and investigated the following hypothesis:

(A) RIPK3 establishes an antitumoral immune signature in LUAD tissue

(B) RIPK3 acts as a tumor suppressor in LUAD

(C) Necroptosis can be induced by chemotherapeutics in a subgroup of NSCLC cell lines

We showed that in the TCGA cohort, LUAD tumors with high *RIPK3* mRNA levels have an increased expression of immunogenic genes and immune cell signals (A). We further observed that the expression of RIPK3 reduces tumor areas in LUAD mice and is downregulated during tumorigenesis (B). Furthermore, we showed that Paclitaxel and Pemetrexed induce cell death via necroptosis, to a similar or higher level than apoptotic cell death (C).

5.1 RIPK3 and its immunogenic role in regulating necroptosis

We compared human LUAD transcriptomes of samples with high and low *RIPK3* mRNA levels to depict differentially expressed genes and their biological function. This analysis outlined an increase of immunogenic gene transcription in LUAD samples with high *RIPK3* levels contributing to the stated immunogenic nature of necroptosis. Of note, the enriched biological processes associated with increased gene levels are regulating immune responses and the activation of the immune system. The transcriptomic results strengthened our hypothesis, that RIPK3 expression increase tumor immunogenicity, despite not explaining the underlying mechanism and pathway execution. We suggest that, on the one hand, high *RIPK3* levels increase the activity of downstream signaling pathways, which activate transcription factors of

immunogenic genes, and, on the other hand, necroptosis leads to accumulation of necrotic cell debris, which induce inflammatory pathways in bystander cells. Both results are relying on the RIPK1-RIPK3-MLKL axis, which is activated by cell death receptor signaling like TNFα in a low Caspase 8 state.

Activated RIPK3 phosphorylates MLKL, which causes a transformational change in the protein structure and exposure of the lipid binding 4HB domain (Cho et al., 2009; Li et al., 2012). Phospho-MLKL interacts with the plasma membrane and induces transmembrane pore formation by either oligomerization or recruiting of ion channels (Cai et al., 2014; X. Chen et al., 2014; Dondelinger et al., 2014; Murphy et al., 2013; Sun et al., 2012; Wang et al., 2014). Subsequently, the resulting hydrogen influx induce cell swelling, cell membrane rupture, and the release of DAMPs. Exposed DAMPs, such as DNA and interleukins, are recognized from pattern-recognition receptors (PRR) of cells in the nearby necrotic environment. PRRs induce inflammatory cytokine and chemokine transcription via Toll-like receptor signaling or interleukin receptor signaling (Alvarez-Diaz et al., 2016; Moriwaki et al., 2017). The paracrine release of DAMPs thereby elevates immunogenic and inflammatory gene transcription in investigated sequenced tumor bulk samples.

Furthermore, RIPK3 mediates cell intrinsic gene transcription with inflammatory functions by promoting NF-κB signaling. It remains unclear in which regulatory way RIPK3 impacts either mitogen-activated protein kinase cascade or NF-κB. Both pathways are upregulated in the presence of RIPK3 and increase the transcription of immunogenic genes such as coding for Interleukin-1β and NLR-family-pyrin-domain-containing 3 (NLRP3) (Moriwaki et al., 2014; Najjar et al., 2016). Additionally, RIPK3 induces the NLRP3 dependent inflammasome formation by either increasing the Caspase8-RIPK1 axis or by MLKL dependent potassium pores leading to potassium efflux. The inflammasome in turn executes Pro-Interleukin-1β cleavage and secretion, which mediates inflammation (Conos et al., 2017; Kang et al., 2013; Lawlor et al., 2015; Moriwaki, Bertin, Gough, & Chan, 2015). RIPK3 directly regulates the translation of cytokines by stabilizing the mRNA-ribosome complex at the endoplasmic reticulum. This effect even persists in necrotic cells after MLKL induced membrane rupture and cell death (Muendlein et al., 2020; Orozco et al., 2019).

The described biological functions of how RIPK3 acts immunogenic in the necroptotic cascade underlines our observed results that increased RIPK3 expression enhances tumor immunogenicity.

5.2 RIPK3 controlling cell cycle

We showed that tumor samples with low *RIPK3* levels have higher mRNA levels of genes involved in cell proliferation and cell cycle control. These genes and associated biological processes are downregulated in samples with high *RIPK3* mRNA counts. We assume, that RIPK3 as a cell-death-mediating protein silences the ongoing cell cycle to switch from cell proliferation in an RIPK3 low state to cell death in an RIPK3 high state.

It is known that the kinase activity of RIPK3 phosphorylates proteins, which regulate proliferation, cell division, and chromosome organization. This was shown in global *in vitro* phospho-proteomic and transcriptomic analysis and evolved the assumption that RIPK3 controls proliferation (Al-Moujahed et al., 2019; Wu et al., 2012). In more detail, molecular analysis delineated the interaction of RIPK3 with the mitotic ripoptosome formed by FADD, RIPK1, and Caspase 8. The ripoptosome degrades Polo-like-Kinase 1 (PLK1), which has regulatory functions in cell division. Furthermore, decreasing RIPK1 or Caspase 8 levels at the ripoptosome increases PLK1 and in turn destabilizes mitotic chromosomes (Liccardi et al., 2019). Of note, high RIPK3 levels are detected in the G2/M phase of the cell cycle, in which PLK1 dependent RIPK3 phosphorylation stabilizes RIPK3 in the ripoptosome complex. This further increases Caspase 8 activity, which induces apoptosis or in a Caspase 8 absent situation activates RIPK1-RIPK3 mediated necroptosis (Gupta & Liu, 2021). In the TCGA dataset of LUAD, we found *PLK1* significantly but only slightly increased in low *RIPK3* samples (RIPK3 high vs low: Fold change: -0.76; adjusted p-value (unpaired t-test): 1.22e-05), which does not correlate with *RIPK3* expression. We therefore assume that the RIPK3-PLK1 interaction is not depending on RIPK3 associated changes in gene transcription associated with high or low *RIPK3* mRNA states.

5.3 Antitumoral immune cell recruitment of RIPK3 dependent necroptosis

We investigated the tumor immune microenvironment by calculating immune scores based on marker gene expression levels, as published by Danaher *et al.* (Danaher et al., 2017). This method allowed the analysis of immune signals of different immune subpopulations in LUAD lesions with high or low *RIPK3* mRNA levels. Our analysis was based on TCGA LUAD datasets, where we observed an enrichment of immune cells from the lymphoid and myeloid lineage correlating with increased *RIPK3* expression. Interestingly, immune populations participating in antitumoral immune responses such as antigen presenting cells and effector immune cells reached significantly higher immune scores in LUAD bulk samples with high *RIPK3* levels.

Based on these results, we state that RIPK3 contributes to the immune cell recruitment into tumor lesions. Despite showing the coincidence of high immune scores for LUAD lesions with high *RIPK3* expression, we did not obtain evidence in how RIPK3 regulates immune cell recruitment. Our analysis was limited to sequenced tumor bulk samples consisting of diverse cell types such as tumor cells, normal cells as well as immune cells, which all influence the *RIPK3* expression

level. To impede the bias that immune cells themself dominate the *RIPK3* expression in sequenced bulk samples, we mapped immune scores to *RIPK3* mRNA levels and showed that even tumor lesions with high *RIPK3* had weak immune cell signals (Figure 18). This suggests that the *RIPK3* expression level was not mainly driven by immune cells and moreover relied on tumor- or normal lung cells in the sample.

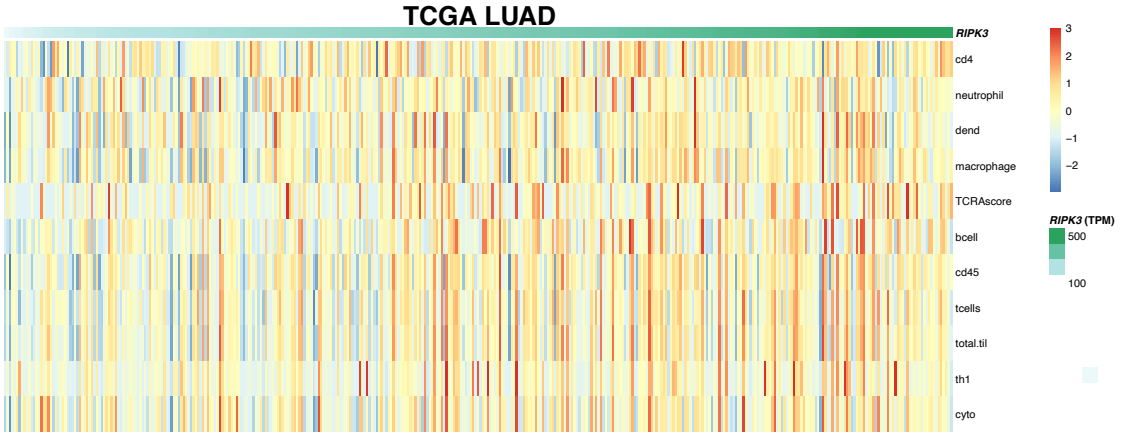

Figure 18: Immune cell enrichment associated with RIPK3 expression in human LUAD bulk samples: Immune scores of immune subpopulations for each sequenced patient sample sorted by RIPK3 expression (transcripts per million; TPM) and presented in heatmaps. Immune score published by Danaher et al. (Danaher et al., 2017) and calculated from the TCGA study. Bioinformatic analysis performed by Dr. Nicholas McGranahan and Dr. Michelle Dietzen.

Recent studies declare that inflammatory cell death such as necroptosis executes three processes necessary for recruiting immune cells. We here refer to stated processes as an explanation of observed immune signals.

First of all, dying tumor cells release antigens, which are recognized as foreign epitopes by bystander immune cells (DuPage et al., 2012). These tumor antigens can be divided into tumor associated antigens (TAAs) and tumor specific antigens (TSAs). TAAs are proteins transcribed in tumor cells, which are normally silenced in normal lung cells and TSAs summarize neoantigens resulting from mutated gene products (Alexandrov et al., 2013; Balachandran et al., 2017; Lawrence et al., 2013; Matsushita et al., 2012; D. Wang et al., 2019; Yadav et al., 2014). Both types can be processed by antigen presenting cells triggering an immune response (Ma et al., 2013; Zeelenberg et al., 2008). Of note, the immunogenic efficiency of TAAs was proven by vaccination studies relying on TAA expression. Vaccinated TAAs primed immune cells against cancer TAAs like the MAG-A3 protein in NSCLC tumor cells. The antitumoral effectivity was validated in the MAGRIT-trail (MAGE-A3 cancer immunotherapeutic as adjuvant therapy in patients with resected MAGE-A3-positive non-small-cell lung cancer) and showed a tumor clearing effect (Kenter et al., 2009; Vansteenkiste et al., 2013; Vansteenkiste et al., 2016). Furthermore, human LUAD tumors are among the highest mutated cancer entities with the highest tumor mutational burden. This leads to an increase of tumor neoantigens, which promote the activation of antitumoral immune cells. Tumor neoantigens further increase the efficiency of

immune checkpoint inhibitors (like PD-1) restoring the function of cytotoxic T-cells (Brown et al., 2014; McGrail et al., 2021). They are assumed to be of predicative value for an anti-PD-1 therapy.

The second process contributing to immune cell recruitment relies on the release of cytosolic, constitutive DAMPs (cDAMPs). Necroptosis liberates different damage signaling molecules like high-mobility-group-protein B1 (HMGB1), heat shock proteins (HSP70/80/90), ATP, IL1, and more (Martins et al., 2014; Spisek et al., 2007; Yamazaki et al., 2014), which are normally hidden from the immune system and therefore highly immunogenic if spilled into the extracellular matrix. Tissue resident antigen presenting cells like dendritic cells bind to immunostimulatory cDAMPs by receptors like toll-like receptors, NOD-like receptors, P2Y2-ATP receptors. Thereby activated signaling pathways lead to antigen processing and presentation, followed by antigen cross priming to effector immune cells (CD8+ T-cells) and B-cells in lymph nodes.

The third process depends on immune cells and necroptotic tumor cells, which transcribe chemokines and cytokines (inflammatory DAMPs/iDAMPs: IFN-α, IFN-β, CXCL1, CCL2, CXCL10) as a reaction to inflammatory stimuli. These iDAMPs promote immune cells to migrate into the inflammatory tissue and activate immune cells.

Taken together, RIPK3 dependent necroptosis as a form of inflammatory cell death releases tumor antigens as well as c- and iDAMPs, which attract resident APCs and in turn recruit as well as activate effector immune cells. Effector immune cells are of therapeutic importance as they kill tumor cells and clear the cancer burden. The observation of increased immune signals from APCs and T-/B-cells in *RIPK3* high LUAD-TCGA samples underlines that necroptosis contributes to the above-mentioned immunogenic steps without elucidating which antigens or DAMPs are responsible for the immune enrichment.

Functional analysis of how necroptotic cells recruit tumor killing CD8+ T-cells were performed by vaccinating tumor xenograft models with necroptotic cell remnants of cancer cell lines, fibroblasts, or cancer cell mimicries. These investigations showed that injecting necroptotic cells into the tumor tissue reduce the tumor size by increasing T-cell abundance (Aaes et al., 2016; Kang et al., 2018; Snyder et al., 2019; Yatim et al., 2015). It still remained controversial if either NF-κB induced immunogenic gene transcription and tumor antigens (Snyder et al., 2019; Yatim et al., 2015) or the release of DAMPs (Aaes et al., 2016) were mediating immune cell recruitment. The observed recruitment of antitumoral immune cells could rely on the release of DAMPs and tumor antigens from necrotic tumor cells, whereas utilized necroptotic fibroblasts by Snyder *et al.* (Snyder et al., 2019) were restricted to the release of DAMPs and thereby less immunogenic.

To validate RIPK3 dependent changes in the tumor associated immune microenvironment, we investigated the abundance of immune cells in K- and KP-LUAD mouse models. Here, we were able to analyze tumors, which seemed to downregulate *Ripk3* by themselves. We performed IHC staining of T-cells and macrophages. Our evaluations of CD3+ and CD8+ T-cells did not result in an enrichment of CD8+ T-cells in RIPK3 high lesions. As we assumed that CD8+ T-cells are a major tumor killing immune population further important for necroptosis induced immune responses, we could not relate tumor suppressive effects to invading cytotoxic T-cells. Further investigations are needed to delineate present T-cell subpopulations and supplement the IHC results to validate enriched T-cell phenotypes in detail by applying more T-cell specific markers. This possibly increases the understanding of T-cells in the TIME for example in FACS or single cell transcriptomic analysis, as published by Szabo *et al.* (Szabo et al., 2019).

We suggest that the investigation of immune cells in our mouse models are limited by a reduced capacity to accumulate mutations and mutated antigens during tumorigenesis. Validated models had strong and efficient oncogenic driver mutations using $Kras^{G12D}$ and $Kras^{G12D}$ *p53* leading to tumoral transformation in 16 to 24 weeks after tumor induction by AAV9 infection. This short duration may not lead to a sufficient accumulation of tumor neoantigens, especially as all mice were bread and hold in clean and sterile conditions. The inhalation of exogenic mutagens in our experimental mice was reduced to a very minimum, which is quite different to human conditions, where exogenic mutagens continuously challenge lung cell genomes increasing the lung mutational burden and neoantigens. In our mouse models, we aimed to be as precise as possible to obtain RIPK3 dependent effects without getting biased from non-detected random mutations. Consequently, we may have decreased the overall immunogenic potential of mice compared to human LUAD tumors.

5.4 Necroptosis influences macrophage polarization

In the human TCGA studies, we obtained higher immune signals (Danaher scores) for macrophages, dendritic cells, and mast cells in tumor lesions with high *RIPK3* expression. Especially for macrophages we show that the immune signal significantly increases in correlation with *RIPK3* levels. We assume that RIPK3 signaling attracts tumor invading macrophages, which in turn enrich in sequenced LUAD samples with high *RIPK3* expression. Our results of *RIPK3* associated differential gene expression underline that high *RIPK3* levels in TCGA-LUAD samples (RIPK3 mRNA levels > 75% of all samples) promote immunogenic functions, which positively mediate immune responses, defense responses (GO:0006955, GO:0050776, etc.), as well as activation of immune cells (GO:0002694, GO:0045321, etc.). Therefore, the obtained macrophage enrichment is likely initiated by RIPK3 dependent signaling and cell death, which induces immunogenic gene transcription, cytokine/chemokine production, and release of death/damage signals as shown for NF-κB and MLKL (Park et al., 2021; Snyder et al., 2019).

Invading macrophages possibly clear dead tumor cells in the lung tissue, which contributes to tumor antigen presentation. Macrophages phagocytize tumor cell remnants and present TAAs to effector immune cells. In the process of cross-priming the effector cells like cytotoxic T-cells get activated and primed to lung tumor cells, which express the related epitopes. This may result in an antitumoral immune respond initially triggered by occurring necroptosis.

The calculation of Danaher scores for macrophage abundance included four marker genes with only one (*CD163*) restricted to macrophages and monocytes (Fischer-Riepe et al., 2020; Lau et al., 2004). The other marker genes (*CD68, CD84* and *MS4A4A*) are highly but not only expressed in macrophages as they are detectable in other immune cells like dendritic cells (*CD68*) (Gottfried et al., 2008) or B-cells (*MS4A4A*) (Zuccolo et al., 2013). The combination of all 4 genes in a calculated score showed a high sensitivity for macrophage identification in pairwise similarity statistics for quantifying marker-like co-expression patterns published by Danaher *et al.* (Danaher et al., 2017). Stated macrophage identification was reproducible with additional methods not based on mRNA seq. datasets (Danaher et al., 2017). Therefore, we suggest that despite not relying on only macrophage specific genes, the here calculated Danaher scores sufficiently detect macrophage abundance rendering out signals from other immune cells (Rosenthal et al., 2019).

Moreover, we validated RIPK3 dependent macrophage enrichment in LUAD mouse models by IHC-staining of a macrophage marker protein (F4/80). We thereby verified the macrophage enrichment in human mRNA-based samples on protein level in mice to strengthen our hypothesis. Tumor-associated macrophages (TAMs) serve as orchestrators of cancer progression or suppression by regulating inflammation, growth, angiogenesis, structure of the extracellular matrix, and even metastasis. Hence, TAMs were of main interest in our investigations on necroptosis changing immune cells in the tumor area.

A functional spectrum has been described for macrophages, which differentiates either antitumoral/ proinflammatory (M1) or protumoral/ antiinflammatory (M2) phenotypes. In the present work, we further used our LUAD mouse models to verify RIPK3 associated macrophage polarization into either a pro- or antitumoral phenotype. Polarization analyses were restricted to mouse experiments because mRNA based immune scores from human datasets do not differentiate between M1 and M2 phenotypes. Established polarization marker genes such as *IL1, IL2, IL6, TLR2* are not exclusively expressed in macrophages, thus diminishing the gene expression signature in sequenced bulk samples. Therefore, we analyzed macrophage polarization by IHC-staining of iNOS for antitumoral (M1) macrophages and Arginase-1 for the protumoral (M2) macrophages. We utilized the iNOS/Arginase-1 based polarization system because of the metabolic and M1/M2 specific dichotomy of these enzymes. Arginase-1 and iNOS compete for the same substrate (L-arginine) but convert it into phenotype specific products with

opposite functions. Whereas iNOS produces cytotoxic, radical oxygen species by converting L-arginine into L-citrulline and nitric oxide, Arginase 1 produces L-ornithine and urea, which provide polyamines to promote cell proliferation as well as L-proline, which is essential for collagen assembly and supports tumor progression. However, as the M1/M2 classification oversimplifies the complex spectrum of various phenotypes, a more specific delineation may be achieved by analyzing metabolic, functional, and developmental differences. Our experimental design in evaluating IHC slides was limited by total number of slides depending on available tissue volume and tumor size. Analyzed tumor lesions had to be detected on various IHC slides to validate RIPK3 expression and match the tumor to the same lesion on immune IHC-staining.
In *Kras*^{G12D} *p53* LUAD mice we showed an enrichment of iNOS positive macrophages in tumor lesions with strong RIPK3 expression. The abundance of protumoral M2 macrophages did not change in RIPK3 strong compared to RIPK3 weak expressing tumors. We suggest that the RIPK3 associated increase of M1 macrophages underlines the stated antitumoral immune reaction induced by necroptosis. Furthermore, we differentiated between an M1 enrichment relying on the recruitment of antitumoral macrophages into the tumor environment or switching resident M2 to M1 macrophages by polarization. Therefore, we stained overall macrophages in the lung tissue slides by the pan-macrophage marker F4/80. We did not detect differences in the number of present macrophages comparing RIPK3 strong and weak tumor lesions, which speaks against a RIPK3 dependent macrophage recruitment. Subsequently, we estimated the proportion of iNOS positive and Arginase-1 positive macrophages from all staining positive macrophages (iNOS and Arginase-1). We obtained an increase in the iNOS positive proportion in tumors with strong RIPK3 expression, which points to macrophage polarization as the mechanism of M1 enrichment. We suggest that RIPK3 contributes to polarization, in which the M2 phenotype switches into a M1 phenotype.

Present IHC analysis were limited to single proteins and incapable for comprehensive analysis providing further mechanistic details of RIPK3 dependent polarization. We did not estimate and differentiate accountable DAMPs released by necroptosis and it remains elusive, which are key for M1 polarization, especially as spilled molecules from necrotic cells are diverse. We here refer to recently identified immunogenic compounds by Hu *et al.* (Hu et al., 2021), which must be validated for their impact on macrophage polarization. We also did not depict, whether M1-macrophages in the TIME increase RIPK3 expression by activating cell death and subsequently necroptosis. This process may generate a macrophage dependent anti-tumoral reaction initiating necroptosis as a tumor suppressive cell death pathway in LUAD. Future investigations will have to validate RIPK3 activation and the resulting recruitment of macrophage phenotypes in the TIME to further target necroptosis as a novel therapeutic approach. We suggest that a preserved RIPK1-RIPK3 axis is essential to increase necroptotic activity and immune cell recruitment in LUAD as published in melanoma xenograft models by Snyder *et al.* (Snyder et al., 2019).

5.5 Regulation of RIPK3 suppression in LUAD

Necroptosis induction is avoided by cancer cells to escape inflammatory cell death and sustain outgrowth. Cell death evasion is a fundamental principle of tumorigenesis and has been defined as hallmark of cancer, which was primarily related to caspase dependent apoptosis (Hanahan & Weinberg, 2000, 2011). Recent investigations of inflammatory cell death unraveled a similar tumor cell eliminating role often assumed as apoptotic backup, which therefore is as well silenced during cancer cell development (Hanahan & Weinberg, 2011). We stated that *RIPK3* is downregulated in LUAD to overcome necroptotic cell death.

To prove our hypothesis, we performed RIPK3 IHC-staining and semiquantitative validation of RIPK3 expression intensities. We showed that in LUAD mice advanced lesions (Adenoma and Adenocarcinoma) reduce the expression levels of RIPK3 compared to early lesions (bronchial hyperplasia). These results verified our hypothesis. Doing so, assumes a mechanistic background of RIPK3 regulation in tumor cells shown in recent manuscripts, which point to specific *RIPK3* regulating transcription factors and methylation mediating enzymes.

Specificity Protein 1 (SP1) was published by Yang *et al.* (Yang et al., 2017) as a *RIPK3* controlling transcription factor resulting from experiments, in which the inhibition or disruption of the *SP1* binding site in the promoter region decreased RIPK3 expression. The relevance of SP1 in regulating RIPK3 expression in lung cancer has yet been shown, but low SP1 levels in lung cancer cell lines decreased the necroptotic activity (Yang et al., 2017). This indicates a relevant expression mediating factor, which needs further validation in human lung cancer samples.

Furthermore, endothelial hypoxia increased RIPK3 expression and in turn promotes ischemic necrosis. Thereby, hypoxia induced factor 1α (HIF1α) and the nucleosome remodeling and deacetylase (NuRD) chromatin-remodeling complex were identified as transcription factors, which increased RIPK3 expression (Colijn et al., 2020; Huang et al., 2013). Interestingly, in our investigations of LUAD tumors, we observed a small, not further validated number of lesions, which showed elevated RIPK3 expression in the hypoxic core area surrounding a necrotic center (Figure 19. A, B). This phenomenon assumes that tissue hypoxia upregulates RIPK3 expression, which may initiate necroptosis. We suggest that theses tumor related changes in the lung tissue induce necroptosis to rescue from oncogenic transformation.

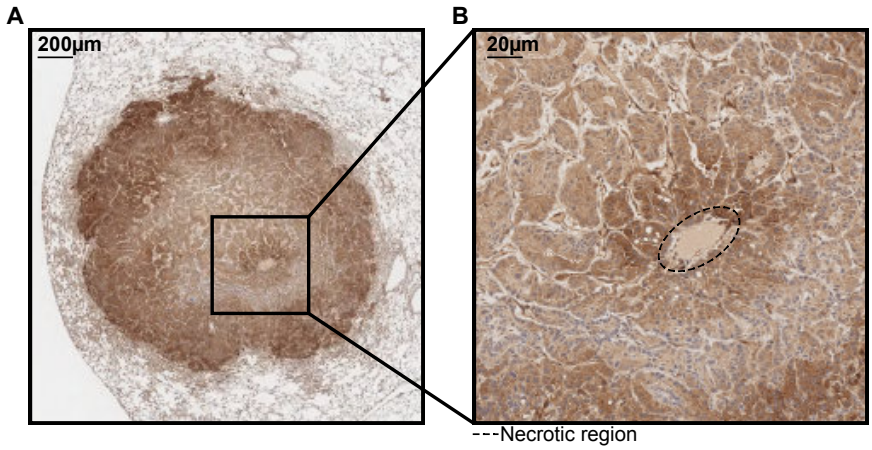

Figure 19: High RIPK3 expression in the necrotic core region of LUAD: A, B: Representative RIPK3 IHC-staining, which outline high RIPK3 expression in lung cancer cells from KP-LUAD mice, which surround a necrotic core region. Image scale as reported in each panel.

Other than the mentioned transcription factors, epigenetic modifications were reported to reduce RIPK3 expression. DNA (cytosine-5)-methyltransferase 1 (DNMT1) induced CpG-hypermethylation in the *RIPK3* promoter region, which reduced RIPK3 levels in colorectal carcinoma and breast cancer cell lines (Koo et al., 2015; Yang et al., 2017). Additionally, Wang *et al.* (Q. Wang et al., 2020) reported that hypermethylated *RIPK3* promoter regions decreased necroptotic activity in NSCLC cell lines. Gene silencing via methylation may be a favorable mechanism because the gene sequence is preserved and demethylating agents like 5-azacytidine may reverse *RIPK3* downregulation. This was proven for *in vitro* cell lines and *in vivo* mouse xenografts, in which restoring RIPK3 expression increased tumor cell death after treatment with chemotherapeutics (Koo et al., 2015).

These findings demand further investigations to prove whether restoring RIPK3 by hypomethylating agents can be beneficial in clinical implementations, especially if necroptosis resistance occurs.

5.6 Tumor suppressive function of RIPK3 in LUAD

Evasion of cell death promotes tumor progression by keeping malignant cells alive while suffering from cellular stress during rapid outgrowth and genetic instability. Functional cell death cascades such as necroptosis are of emerging scientific interest because death activation highly acts tumor suppressive. Cell death programs, also described as cell suicide programs, constitute rescue pathways, which shut down cells during irreversible oncogenic transformation to impede cancer development. Consequently, cancer cell surveillance crucially relies on overcoming cell death by inhibiting related cascades and key proteins. The caspase dependent apoptosis is affected by a high number of different aberrations in various cancer entities including lung adenocarcinoma, which are relevant for tumor progression (Munkhbaatar et al., 2020). Alternative cell death pathways, like necroptosis, are often stated as apoptosis back up and frequently downregulated in cancer. It remains elusive if alternative cell death pathways

sufficiently contribute to tumor suppression among different cancer entities like non-small cell lung cancer. In recent years, immunogenic forms of cell death evolved as promising death cascades, because immune stimulation leads to the recruitment and activation of immune cells. Especially, the activation of antitumoral immune cells, which identify and kill tumor cells causes a persistent antitumoral reaction. We assume that immunogenic cell death in particular necroptosis acts tumor suppressive in lung adenocarcinoma, because leveraging the antitumoral immune response by immune check point inhibitors was clinically successful and increased the overall patient survival (Hellmann et al., 2019). This underlines the critical role of the lung associated immune system, which may be further promoted by necroptosis.

The present results link the necrotic death cascade with immunogenic and tumor suppressive functions. The observed immunogenic nature of RIPK3 promoted inflammatory gene transcription, which initiate the NLRP3 inflammasome, release DAMPs and TAAs (see chapter 4.1). Our investigations on how necroptosis influences LUAD tumorigenesis focused on the RIPK3 protein, which is the key regulator of necroptosis and frequently absent in cancer cell lines to evade necroptotic cell death. This was the case as well for *RIPK3* mRNA levels in human LUAD cell lines. We did not investigate additional pathway mediators in detail because the upstream element RIPK1 is not restricted to necroptosis and participates in the execution of apoptosis. Furthermore, RIPK3 dependent necroptosis can be activated independently of RIPK1, as shown by Wang *et al.* (L. Wang et al., 2019), which underlines that RIPK1 is not necroptosis specific. Moreover, the downstream element MLKL, which forms transmembrane pores requires RIPK3-RHIM interaction, which leads to RIPK3 dependent phosphorylation and in turn activation (see chapter 1.5). Taken together, the execution of necroptosis critically relies on RIPK3.

We suggest that the antitumoral role of RIPK3 dependent necroptosis in lung adenocarcinoma is not only based on its death inducing properties, but is moreover related to the triggered immunogenic responses, as recruitment of T-cells and polarization of macrophages. It was shown that the composition of immune cells in lung cancer tissue is of importance for patient survival (Bentham et al., 2021; McGranahan et al., 2017). The immunogenic function of necroptosis changed the TIME in human LUAD samples by increasing antitumoral immune cells, especially CD8+ T-cells. These cells are critical in controlling tumorigenesis and have clinical relevance as patients' overall survival significantly increases if the inhibition of effector immune cells is reversed by immune checkpoint inhibitors (Reck et al., 2021).

Moreover, comprehensive datasets of large lung cancer cohorts outline that lung adenocarcinoma and squamous cell carcinoma are within the top cancer entities with the highest tumor mutational burden, further leading to an increase of tumor neoantigens. These neoantigens were described as

important for T-cell responses especially if reactivated by immune checkpoint inhibitors (McGrail et al., 2021). In the process of necroptosis, tumor associated antigens are released by dying cells, due to induced membrane rupture, and promote antitumoral immune cells. The tumor suppressive impact of necroptotic cells in lung cancer was also demonstrated by Snyder *et al.* (Snyder et al., 2019) utilizing mouse xenografts of Lewis-cell carcinoma of the lung (LL/2-OVA). Here, tumors injected with necroptotic fibroblasts resulted in smaller lesions than tumors injected with apoptotic cells or the vehicle control. Hence, to suppress LUAD tumorigenesis it is not only of importance that the tumor cells die but further that they do so in an immunogenic way. Especially, Snyder *et al.* (Snyder et al., 2019) reported that the immunogenic reaction resulting from necroptosis was more efficient in reducing the tumor volume than the induced cell death by apoptosis.

Furthermore, we suggest that necroptosis sustain cell death even if aberrations in the apoptotic pathway led to resistance in LUAD (Munkhbaatar et al., 2020). In the human lung cancer cell line NCI-H1437 the necroptotic RIPK1-RIPK3-MLKL axis was preserved and successfully induced necroptosis, whereas the apoptosis induction was inefficient. Hence, we suggest that the TNF induced death pathway shifts from apoptosis to necroptosis in condition of caspase 8 loss (Fritsch et al., 2019). This might also be the case for overexpression of antiapoptotic Bcl2-familiy members.

Among all investigated human LUAD cell lines *RIPK3* mRNA levels were frequently found undetectable by qRT-PCR. This resulted in necroptosis resistance even if apoptosis activation induced cell death. We assume that necroptosis can be beneficial for a defined cohort of LUAD patients with preserved expression of pathway mediators, especially RIPK3. Human LUAD cells overcome cell death by decreasing key proteins but do not restrict to apoptosis as we show that alternative death cascades like necroptosis are also frequently downregulated.

5.7 The role of RIPK3 in solid cancer entities

The tumor suppressive function of RIPK3 in cancer was controversially discussed as in contrast to antitumoral functions described by us and others, tumor promoting function were published for RIPK3 induced inflammation in pancreas cancer and colorectal carcinoma. We therefore depict differences in described RIPK3 mediated mechanisms, which differ in presented entities leading to conflicting outcomes. As we do not delineate the tumor suppressive pathways mediated by RIPK3 in detail but show a clear tumor suppressive phenotype including antitumoral immune cell signatures in LUAD, we here refer to published notions of others.

In the tumorigenesis of colorectal carcinoma (CRC) an either pro- or antitumoral role of RIPK3 was described. In human cancer datasets containing mRNA sequenced samples of colorectal

carcinoma *RIPK3* expression was overall reduced compared to normal and adjacent tissue. Furthermore, RIPK3 appears absent in most cancer cell lines (He et al., 2009; Koo et al., 2015; Moriwaki, Bertin, Gough, Orlowski, et al., 2015). This indicates that RIPK3 is downregulated during tumorigenesis of colorectal carcinoma. Moreover, a low expression of *RIPK3* in CRC was associated with a poor overall survival compared to patients with high *RIPK3* expression, and therefore of prognostic value (Conev et al., 2019). In the validation of various CRC models RIPK3 participated in differing mechanisms with conflicting outcomes (Alvarez-Diaz et al., 2021). RIPK3 mediated cancer formation in inflammatory induced carcinoma. Tumor development depends on epithelial mTOR hyperactivation in response to environmental exposure (microbiota and western diet), which increases the RIPK3-MLKL axis (Xie et al., 2020). Necroptosis in intestinal epithelial cells disrupts the colorectal barrier and feeds a continuous invasion of pathogens from the gut. Subsequently, this triggers inflammation and dysbiosis promoting inflammatory bowel diseases (Crohn's disease, ulcerative colitis). Necrotic epithelial cells additionally increase immunogenic JNK-signaling and regulate myeloid derived cells, which repress an adaptive immune response and release tumorigenic factors (Jayakumar & Bothwell, 2019; Z. Y. Liu et al., 2019). Resulting inflammatory signature induces genetic instability, evasion of apoptosis and increased proliferation, which leads to tumor formation (S. B. Lee et al., 2019).

In contrast to the protumoral role in inflammation induced CRC, RIPK3 was as well associated with tumor suppressive effects. In *Ripk3* knockout mice, intestinal epithelial cells showed an increase and uncontrolled activation of NF-κB, STAT3, AKT, and Wnt-β-catenin signaling causing highly proliferative cells, developing into colorectal carcinoma (Bozec et al., 2016). Sporadic intestinal tumors, which make up the majority of CRC, were initiated in $Apc^{min/+}$ mice and showed an increase of tumor burden after *Ripk3* knockout. These results were associated with enhanced STAT3 signaling and IL6 production, which was reversed in *Ripk3* wildtype $Apc^{min/+}$ *mice* (Zhao et al., 2021). The activation of necroptosis in CRC-xenograft models by either applying RIPK3 activating agents (HS-173) or RIPK3 expressing liposomes (mRIPK3-HA-P-LP) significantly reduced the tumor volume compared to control vehicles (Park et al., 2019; Snyder et al., 2019; Zhang et al., 2020).

Taken together, we assume that on the one hand RIPK3 mediated necroptosis promotes tumorigenesis in CRC if executed in vulnerable cells, which build up barriers to prevent pathogen invasion and dysbiosis.

On the other hand, necroptosis in colorectal cancer cells reduce tumor progression by inducing cell death and the release of tumor associated antigens, which further prime antitumoral immune cells to cancer cells. The declared antitumoral role would rely on the same principles stated by us for LUAD tumorigenesis.

In pancreatic ductal adenocarcinoma (PDA), Seifert *et al.* (Seifert et al., 2016) demonstrated a RIPK3 dependent tumor promoting effect, which challenged the previous stated antitumoral principles of necroptosis acting tumor suppressive. Investigated mouse models showed that inducing *Ripk3* knockouts in $Kras^{G12D}$ driven PDA rescued from tumor development and decreased tumor size. This effect was associated with reduced CXCL1 and Mincle signaling, which targets immune suppressive regulators in tumor associated immune cells. Loss of *Ripk3* increased T cells and antigen presenting TAMs (MHC II+ TAMs) and decreased immune blocking, PD-1 positive cells in the tumor environment. In contrast to the *in vivo* results Seifert *et al.* declared that blocking necroptosis *in vitro* increased PDA cell proliferation (Seifert et al., 2016). These results are not in line with the present results for LUAD tumors and in conflict with our understanding of RIPK3 dependent necroptosis in cancer. Hence, we assume that major differences rely on the tumorigenesis of LUAD and PDA, further leading to different outcomes after necroptosis inhibition.

We suggest that the lung resident immune system may be highly reactive due to the continuous exposure to the exogenic environment in contrast to the isolated immune system in the pancreas, which might be less inflammatory and immunogenic. Bronchial/Alveolar epithelial cells, which are the origin of LUAD, build up a barrier network to protect against the exogenic environment including foreign noxious substances (mutagens) and pulmonary microbiota. The continuous exposure to inhaled particles and pathogens is controlled by a reactive and well-regulated resident immune system, which inhibit pathogen invasion and clear foreign particles as well as mutated cells without destroying the lung barrier. This lung resident immune system facilitates cell death cascades as a response to arising tumorigenesis. Furthermore, necroptosis can be activated by inhaled viruses, which protects against viral replication in infected cells especially as viral pneumonia is the most frequent cause of lung infection (Upton et al., 2010).

In contrast to the lung tissue, the pancreas is not exposed to an exogenic environment and pancreas resident immune cells are not continuously activated by foreign substances and invading pathogens. Therefore, immunogenic cell death may not be capable to shape a reactive and antitumoral immune response. PDA tumors further have a lower tumor mutational burden than LUAD, which may result from the absent exposure to exogenic mutagens. This leads to a lower amount of tumor neoantigens, which in turn decrease the activation of antitumoral immune cells (McGrail et al., 2021; Yang et al., 2020). Furthermore, as the blockade of necroptosis in the PDA mouse model reduced cytokines, which enhance cell proliferation (CXCL1: C-X-C Motif Chemokine Ligand 1), RIPK3 mediated gene transcription might not induce the immunogenic and tumor suppressive signature we observed in human LUAD.

However, Seifert *et al.* showed increased cancer cell proliferation by inhibiting the necrosome *in vitro*, suggesting that the pancreatic environment *in vivo* contributes to the protumoral role of necroptosis in PDA (Seifert et al., 2016). The *in vitro* results support our presented mechanism of RIPK3 reducing cell proliferation.

Further investigations are required to clearly depict whether the resident immune structure or the originating cell of LUAD and PDA contribute to the difference in RIPK3 associated outcomes.

In hepatocellular carcinoma (HCC) Li *et al.* (Li et al., 2019) described an overall decreased *RIPK3* expression among investigated HCC samples compared to non-tumor hepatic tissue. Low *RIPK3* expression of HCC tumors were further associated with a worse prognostic outcome compared to high *RIPK3* expression in HCC patients. RIPK3 deficiency promoted the recruitment of immune suppressive MDSCs in human HCC samples and in mouse HCC-xenograft models. MDSCs reduced antitumoral CD8+ cells, which led to a decrease in antitumoral immune responses and an increase of HCC tumor sizes *in vivo*. Furthermore, Li *et al.* showed that *RIPK3* expression causes immunogenic changes, which relied on CXCL1, CXCL2 chemokines. Both increase immune suppressive MDSCs in HCC tumors (Li et al., 2019).
Moreover, Wu *et al.* (Wu et al., 2020) explained the tumor suppressive effect of RIPK3 with observed M1 TAM polarization. The antitumoral macrophage polarization depended on metabolic changes in the tumor tissue of HCC. Tumor associated macrophages with loss of *Ripk3* decreased ROS production, which enhanced M2 polarization through peroxisome proliferator-activated receptor (PPAR) activation and increased lipolysis. Additionally, RIPK3 deficiency blocked the ROS controlled inflammasome, in turn reducing immunogenic gene expression necessary for antitumoral responses (Wu et al., 2020).
Taken together, the tumor suppressive role of RIPK3 in HCC was mediated by an antitumoral immune microenvironment. Furthermore, RIPK3 expression caused sustained aerobic glycolysis, which did not saturate growing tumor cells and disrupted cancer cell proliferation. These results were similar to the presented function of RIPK3 in LUAD samples, despite not observing RIPK3 dependent changes in tumor cell metabolism. The nutritional deprivation of highly proliferative tumor cells in a hypoxic environment is critical, so that we suggest that RIPK3 is a potential inhibitor of tumor related metabolic adjustments in HCC, which reveals novel benefits in inhibiting tumorigenesis.

Wang *et al.* (K. J. Wang et al., 2020) showed that RIPK3 serves as a potent suppressor of prostate cancer, if being genetically overexpressed. Thereby, the RIPK3 role in tumorigenesis was investigated *in vitro* by prostate cancer cell lines and *in vivo* by using mouse xenograft models injected with PC3-cells. Additional to prostatic cancer, *RIPK3* was found repressed in human prostate cancer samples compared to normal samples, which is similar to described *RIPK3* levels in LUAD, CRC, and HCC. *RIPK3* expression was further of prognostic value as patients with high *RIPK3* expression in prostate cancer had an overall increased survival compared to patients with low *RIPK3* expression. Wang *et al.* observed that an increased expression of RIPK3 inhibits remodeling of the extracellular matrix by reducing matrix-metalloproteases (MMP2/9) expression and increases cellular adhesion molecules like cadherin-E. Both processes contributed

to the inhibition of prostate cancer growth. Furthermore, Wang *et al.* depicted a RIPK3 dependent decrease of proteins involved in cell cycle control, by inducing G2/M-phase transition.
This supports the presented results of RIPK3 reducing cell proliferation and controlling cell cycle, as shown by us for human LUAD samples (K. J. Wang et al., 2020).

Summarized, these manuscripts elucidated different functional roles of RIPK3 in suppressing or promoting tumorigeneses. Of note, despite inducing cell death the main impact of necroptosis relied on shaping a tumor associated immune system with antitumoral or protumoral functions. An antitumoral impact was suggested by us in LUAD and is supported from cited manuscripts of other cancer entities. Interestingly, RIPK3 dependent necroptosis did not only mediate immunogenic gene transcription, but moreover reorganized the extracellular matrix or cell metabolism. However, RIPK3 has an ambivalent role in cancer as protumoral functions were shown in CRC and PDA. Here, the necroptotic pathway resulted in a tumor promoting immune structure and increased tumor growth. Hence, it must be evaluated, which tumor related differences are responsible for RIPK3 being tumor suppressive or promoting. A clear mechanism behind each role of RIPK3 has yet not been shown in recent manuscripts.

5.8 Necroptosis as an alternative cell death pathway is induced by chemotherapeutics

An urgent observation in clinical oncology is the acquisition of resistance to cell death inducing agents like chemotherapeutics. Inefficient cancer therapies are often associated with the blockage of apoptosis (Zhu et al., 2017). Therefore, alternative cell death pathways bypassing inhibited apoptosis are of critical relevance for sufficient treatment approaches. Necroptosis is a promising death inducing option because frequent aberrations in the caspase dependent pathway (BCL2, MCL1, TP53) preserve the function of non-caspase dependent cell death.

In the present work we show that necroptotic cell death can be induced in a defined subset of LUAD cell lines, which maintain the RIPK1-RIPK3-MLKL axis, even if apoptosis is blocked (see chapter 4.12). We identified paclitaxel and pemetrexed as two chemotherapeutics used in NSCLC regimes, which activate necroptosis in cell lines with high *RIPK3* mRNA levels. These results suggest that necroptosis is a relevant cell death pathway in the treatment of LUAD. As we characterized RIPK3 dependent necroptosis as a tumor suppressive pathway by inducing cell death and promoting antitumoral immune responses, we suggest that necroptosis induction might further be beneficial in LUAD therapy. Clinical trials outlined that immune checkpoint inhibitors increase the overall survival of LUAD patients due to induced antitumoral immune responses (Hellmann et al., 2019). The occurrence of immunogenic cell death might contribute to this antitumoral reaction.
Besides paclitaxel and pemetrexed other chemotherapeutic agents such as cisplatin, oxaliplatin, etoposide or gemcitabine induce necroptosis (Akara-Amornthum et al., 2020; Y. Liu et al., 2019;

Wu et al., 2015; Xu et al., 2017). In the present investigations, we analyzed chemotherapeutics in different cell lines, which were either resistant to apoptosis, necroptosis, or both. By our observations we suggest that apoptosis and necroptosis are initiated cell death pathways by these drugs as stated in the mentioned literature. Hence, we suggest that necroptosis was either activated via accumulation of RIPK1 in a caspase 8 deficient situation (Fritsch et al., 2019) or dying cells released necroptosis-activating molecules like cell death receptor ligands (e.g., TNF), which indirectly activated necroptosis in bystander cells. Human LUAD cell lines which were competent for necroptosis induced necroptotic cell death equally efficient as apoptotic cell death. This underlines that necroptosis seems an efficient alternative cell death cascade to apoptosis.

Moreover, the successful initiation of cell death relies on functional death pathways and the expression of their executive proteins. Regarding our findings that RIPK3 is downregulated in LUAD tumorigenesis and often absent in human LUAD cell lines, necroptosis and its related benefits are restricted to a defined cohort of patients with preserved necroptotic signaling.

Taken together, necroptosis can be a cell death backup in apoptosis resistant cells. Necroptosis contributes to cell death initiation by a group of chemotherapeutic agents and has the potential to induce an immunogenic tissue signature opening new treatment options in the emerging era of immune system-based therapy approaches.

5.9 Scientific impact and limitations

The identification of genomic aberrations impacting or resulting in oncogenic transformation is of importance, as these molecular changes enable targeted therapies in emerging precision medicine.

We here identify RIPK3 as a tumor suppressor in LUAD by showing that *RIPK3* expression correlates with global genomic changes, in which the transcription of genes promoting cell proliferation is reduced and immunogenic gene transcription is increased. Immunogenic changes associated with differential *RIPK3* expression impacted immune cell abundance. LUAD tumors with high *RIPK3* mRNA levels increased immune cell signals for antigen-presenting cells and effector immune cells. Furthermore, LUAD mice with reduced *RIPK3* expression promoted tumor growth and changed the associated immune system to a protumoral phenotype. Taken together, RIPK3 dependent necroptosis acted tumor suppressive in LUAD by initiating immunogenic cell death. Hence, we consider RIPK3 as a relevant antitumoral target and suggest that RIPK3 activation is promising for new therapeutic evaluations. Especially as we show that necroptosis can be activated by chemotherapeutic agents like pemetrexed and paclitaxel.

Our present analyses are subject of methodical limitations, which we discuss in the following section. Results of human datasets originated from large scale patient transcriptomic studies published by the TCGA consortium. Besides providing a high amount of sequenced LUAD samples, the patient heterogeneity is dominated by white people with only a small amount of American Indian, Alaska native, Black, or African American. This inequality in race might distort the overall genomic background as not reflecting all human adequately. As we here restrict our analyses to conserved coding regions and not to variant non – coding regions like SNPs any non-repeating differences in the validated sequence are seen as mutational changes (promoter, intron, exon) and not as cultural polymorphisms or variants. Further validated mRNA levels were identified by their preserved sequence independently of race differences. We expect that observed genomic changes follow principle biological mechanisms and thereby can be extrapolated to the whole human species, despite admitting that environmental differences on mutation frequency and epigenetic alterations cannot be excluded. We did not observe a relevant difference in patient gender and distribution of age. In the sample acquisition of the TCGA cohort a strict procedure was followed in which each sample had to fulfill predefined criteria for preserving the highest possible standards of quality. Further details and reviewing instances can be obtained through the Genomic Data Commons Data Portal: (https://portal.gdc.cancer.gov/projects/TCGA-LUAD [last access: 20.01.2022]). We assume that to date the TCGA dataset provide state of the art large scale transcriptomic data for human LUAD cohorts, which allow comprehensive gene expression analysis as demonstrated by the TCGA-LUAD landmark manuscript (Cancer Genome Atlas Research, 2014). We were not in control of identifying background noise across samples and therefore did not apply preprocessing filters to sort out nonmatching or outlying patient samples. Every available LUAD transcriptome was included in the presented analysis. We further declare that we did not analyze the quality of provided samples and that we were not in charge of accessing pathologic reports to verify the diagnosis of LUAD. In our validation of RIPK3 in human LUAD, we observed changes in gene expression, which originate from RNA sequenced tumor bulks samples containing heterogenous cell clusters (tumor cells, epithelial cells, glandular cells, alveolar cells, immune cells, etc.). We could not separate tumor cell transcriptomes from the transcriptome of other cells.

Just with the protocol of Danaher *et al.* (Danaher et al., 2017) relying on multiple immune cell marker genes, we were able to delineate the presence of immune cells in tumor bulk samples. Further, we could not refer tumoral heterogeneity evolving though differences in tumor cell development to *RIPK3* expression. We did not subdivide the LUAD cohort according to any aberrational clusters recognized from TCGA.

Taken together, we here provide insight in global transcriptomic changes associated with different *RIPK3* expression levels in LUAD bulk samples. We assume that RIPK3 dependent necroptosis as a form of immunogenic cell death impacts tumor cells as well as normal cells and results in an inflammatory tumor environment.

Our *in vivo* experiments relied on genetic engineered mouse models containing inducible oncogenic driver mutations to initiate LUAD tumors. The use of experimental animals allowed the implementation of genetic tools, here the Cre/LoxP- system. To study the biology of RIPK3 in LUAD, we simplified the genetic background to one or two strong oncogenic driver mutations frequently used to generate LUAD in mice (*Kras*^{G12D} and *p53*). We thereby reduced confounding influences of unvalidated aberrations arising in complex and heterogenous genetic backgrounds. Complex tumor genomes are generated in mutagen induced LUAD models (Westcott et al., 2015), which match more closely to the high mutational burden of human lung cancer. However, these models lose the controllability by inducing random oncogenic mutations or passenger mutations, which may suppress or promote tumor growth. Therefore, the advantage of obtaining a strong phenotypical association related to RIPK3 in a simplified LUAD GEMM is on the other hand subject to limitations as its genetic background is not as complex as in human LUAD. We do not claim that our results in LUAD GEMMs moreover identify a tumor suppressive gene in human but validate our observations from human transcriptomic datasets pointing to a general immunogenic and tumor suppressive nature of RIPK3 in LUAD. Of note, the *RIPK3* gene sequence is homologue for mouse and human, as shown by the Mouse Genome Informatics (http://www.informatics.jax.org/downloads/reports/HOM_MouseHumanSequence.rpt [last access: 04.01.2022]). It is known that in both species (mouse and human), RIPK3 regulates necroptotic cell death, which leads to tissue inflammation. We assume that in both organisms the biology of necroptosis is preserved, which relies on its critical role in the embryonic development (Zhao et al., 2017), but might also be essential for inducing apoptosis independent cell death as a backup mechanism. These similarities make the mouse a suitable model to evaluate the biology of necroptosis, further improving our understanding in human disease. Especially as not all protein coding genes are preserved between human and mouse, the species inequalities should not affect the investigated genes. We further validated our results in mouse and human to reduce species dependent bias and strengthen our hypothesis. We assume that we have minimized the biological differences affecting the necroptotic pathway between mouse and human as much as possible. Frequent human mutations observed in lung adenocarcinoma were successfully implemented in mouse genomes to generate LUAD models.

In our GEMMs we used genetic inserts, which are most common for LUAD induction and moreover strong oncogenic driver mutations These LUAD-GEMMs were validated for their efficiency in initiating LUAD transformation from alveolar type 2 cells in a group of manuscripts, and our observed LUAD lesions were again validated by histologic criteria and IHC-staining of LUAD cells of origin: CC10/SPC IHC-staining (Zhao et al., 2017). We admit that the pathologic criteria to identify LUAD lesions differ between human and mouse tumors, and we therefore apply mouse specific criteria to define LUAD published by Nikitin *et al.* (Nikitin et al., 2004)

(see chapter 3.7.1). As defined pathological differences between adenomas and more aggressive adenocarcinomas appeared not precise enough for clear differentiations, we summarized both grades in one group. In mouse, we evaluated LUAD adenoma and adenocarcinoma, whereas LUAD in human datasets was restricted to adenocarcinoma. This definition of LUAD limits the comparability of the two species, but we assume only for advanced stage lesions and not for RIPK3 impacting LUAD tumorigenesis in general. We as well did not define mixed tumor lesions with shared histological features of adenocarcinoma and squamous cell carcinoma, which are observed as a minority of generated lesions in *Kras*^{G12D} based LUAD-GEMMs (Marjanovic et al., 2020).

Our present results are also influenced by the differing structure of the immune system of mice and human. Whereas in human lung tissue neutrophiles make up the majority of immune cells, mouse lungs are dominated by lymphocytes (Mestas & Hughes, 2004). All experimental mice were bread under sterile, pathogen free conditions and thereby might not have established a highly reactive resident immune system in the lung, which defends against invading pathogens, as it is the case for human lungs. Furthermore, the simplified genetic background of mice based on two oncogenic modifications may not generate a high amount of tumor antigens needed for antitumoral responses. Taken together; we assume that the immunogenic reaction triggered by necroptotic cell death might be attenuated from the naïve mouse immune system.

Notably, Acebes *et al.* (Casanova-Acebes et al., 2021) analyzed macrophage clusters in human and mouse NSCLC based on unique molecular identifiers (scRNA-seq). The manuscript shows that human and mouse NSCLC resident macrophages of both species share the expression of many genes defining the same clusters. This observation suggests that mouse and human have conserved macrophages with homologue phenotypes, which is further relevant to the present interpretation of macrophage enrichment and polarization in LUAD GEMMs. We assume that the obtained influence depending on *RIPK3* expression in mouse is further relevant for human macrophages as the conserved necroptotic pathway may induce antitumoral macrophage phenotypes in human as well. Despite the shown enrichment of macrophages associated to high *RIPK3* expression in human LUAD samples, delineating macrophage phenotypes will be of further interest.

Our here declared limitations of the presented results must be considered before drawing further conclusions on RIPK3 dependent necroptosis in LUAD. We restrict the general assumption that RIPK3 acts as an immunogenic tumor suppressor to the here presented experimental design of human and mouse LUAD. The suggested biology of RIPK3 must be validated in other LUAD models to strengthen the assumed tumor suppressive potential.

5.10 Outlook

The present results point to a tumor suppressive role of RIPK3 dependent necroptosis in LUAD, which we aim to evaluate for novel therapeutic approaches.

As we observed that the RIPK3 expression is reduced during tumorigenesis, we will implement multiomic LUAD datasets to evaluate different regulating mechanisms, which possibly contribute to the downregulation of *RIPK3*.

Preliminary data pointed to an epigenetic modification in the *RIPK3* promoter region. This would preserve a functional copy of the *RIPK3* gene, whose expression might be restored if the epigenetic modification is reversed. We will focus on methylation of CpG islands as experiments from our laboratory as well as published manuscripts showed that demethylating agents restored RIPK3 expression *in vitro* (Koo et al., 2015; Q. Wang et al., 2020). We will also investigate different transcription factors binding to the *RIPK3* promoter region and validate if these transcription factors enhance or silence *RIPK3* expression.

With the successful introduction of immune checkpoint inhibitors in the therapeutic spectrum of lung cancer, we assume that leveraging the immunogenic crosstalk between immunogenic cell death and activation of antitumoral immune cells may be a potential improvement of immune system-based therapies in LUAD. It is necessary to elucidate which tumor parameters point to a lung associated immune system benefiting from inducing an immunogenic tissue environment. Especially, as current analyses are restricted to predict the responses to immune checkpoint inhibitors with PD-1 positivity scores.

It is further necessary to differentiate which executing function of necroptosis is critical to generate a potent antitumoral immune response. An important impact might rely on the evaluated interplay of increased immunogenic gene transcription and necrotic cell death. Of further importance is the discovery of specific transcription mediating proteins, like NF-κB, which are activated by necroptosis and regulate the expression of distinct cytokines and chemokines.

6 Summary

The induction of cell death is critical for cells vulnerable to oncogenic transformation by continuous accumulation of genomic aberrations. Effective disruption of tumorigenesis requires functioning programmed cell death cascades to inhibit uncontrolled tumor outgrowth. Whereas classic cell death cascades based on caspase dependent apoptosis are frequently downregulated to counteract cell stress, alternative cell death cascades may overcome death resistance in cancer. The importance of identifying additional cell death mechanisms emerges as cancer entities, which escape treatment induced death, reach high related mortality rates. Lung cancer is the cancer entity with the highest mortality, thus requiring the identification of potent therapeutic regimes and relevant death cascades for suppressing tumor growth. Here, we report that Receptor-Interacting Serin/Threonin-Protein Kinase 3 (RIPK3) acts as a tumor suppressor in lung adenocarcinoma (LUAD) by regulating an alternative immunogenic cell death cascade, namely necroptosis. Necroptosis is activated by death signals like TNF and induces cell death via the RIPK1-RIPK3-MLKL signaling axis. The key regulator RIPK3 controls MLKL dependent pore formation in the cell membrane, subsequently resulting in cell swelling and membrane rupture, but additionally increases immunogenic gene transcription to attract and activate immune cells. The immunogenic role of necroptosis contributes to the death induced reduction of tumor cells by shaping an antitumoral immune response. Leveraging the crosstalk between inflammatory cell death and immune micro-environment is a promising new immunogenic therapeutic approach. Within death cascades, necroptosis releases warning signals to highlight the accumulation of damaged cells in the tissue. These signals are recognized by the immune cells, especially phagocytes, which clear left cell remnants. The initiation of necroptosis in tumor cells may release tumor associated antigens as part of damage associated molecules. These TAAs could be utilized by antigen presenting cells to prime immune effector cells and generate an antitumoral immune reaction.

To investigate this biological hypothesis of RIPK3 dependent necroptosis, we evaluated associated differences in gene expression by analyzing mRNA seq. LUAD datasets from the TCGA cohort. We observed that high *RIPK3* mRNA levels were associated with increased immunogenic gene transcription, whereas low *RIPK3* levels increased genes promoting cell proliferation. Furthermore, LUAD tumor bulk samples with high *RIPK3* mRNA levels had a higher immune cell abundance compared to bulk samples with low *RIPK3* mRNA levels. These results were pointing to a tumor suppressive role of RIPK3 in human LUAD.

We delineated the phenotypical impact of necroptosis on LUAD tumorigenesis in genetically engineered mouse models, which induced LUAD lesions by $Kras^{G12D}$ or $Kras^{G12D}$*; p53* driver mutations. The use of animal models allowed the observation of RIPK3 dependent effects on

tumor growth. Lung specific tumor induction was achieved by intratracheal administration of adeno-associated viruses, which infected LUAD cells of origin. AAVs liberated plasmid vectors carrying the sequences coding for the Cre-Recombinase to induce LUAD driver mutations. At 16- or 24- weeks post infection LUAD mice showed a reduced expression of RIPK3 in advanced-stage lesions (Adenoma, Adenocarcinoma) compared to early-stage lesions (Bronchial Hyperplasia). Within the advanced LUAD lesions weak RIPK3 expression resulted in increased tumor areas compared to lesions with high RIPK3 expression. Furthermore, high RIPK3 levels induced an antitumoral macrophage polarization by the enrichment of antitumoral (iNOS)-positive macrophages (M1-phenotype).

A critical complication for lung cancer patients is the development of therapy resistance, which can be due to cell death evasion. We assumed that the detected antitumoral effect of necroptosis in LUAD could be beneficial for therapeutic regimes. We hypothesized that in defined cell lines with a functional RIPK1-RIPK3-MLKL axis, necroptosis can activate and replace apoptosis as a backup mechanism. Furthermore, we evaluated if necroptosis is a relevant cell death cascade activated by chemotherapeutics. Therefore, we detected the expression of necroptosis executing proteins and activated necroptosis as well as apoptosis in human NSCLC-LUAD cell lines. We show that most cell lines had no detectable *RIPK3* mRNA levels, suggesting a tumor-suppressed target to escape immunogenic death, which is in line with the observed RIPK3 depression in LUAD-GEMMs. Of note, we detected necroptosis in cell lines with preserved *RIPK3* expression, even if the cell line was resistant to apoptosis. Additionally, we induced necroptosis by treating competent cells with paclitaxel or pemetrexed.

Taken together, we show that *RIPK3* is reduced among most validated LUAD cell lines but, when preserved, mediates necroptosis execution, which can backup apoptosis. Necroptosis is also initiated by paclitaxel or pemetrexed, which offers a therapeutic approach to activate immunogenic cell death by chemotherapy.

Further investigations are needed to show mechanistic details on how *RIPK3* is repressed during tumorigenesis and if these processes can be reversed. It will be necessary to validate necroptosis activation in cancer to identify critical steps and target genes shaping an antitumoral tumor immune microenvironment. These experiments will need to be expanded across different cancer entities as not all may benefit from immunogenic cell death.

7 Zusammenfassung

Zelltodmechanismen führen zum Untergang von sich maligne transformierenden Zellen und sind daher eine kritische Instanz, um der Entwicklung von Malignomen entgegenzuwirken. Um diesen Schutzmechanismus zu umgehen, reduzieren Krebszellen die Expression von Schlüsselproteinen der klassischer Zelltodkaskaden, wie der Apoptose. Alternative Zelltodsignalkaskaden sind in der Lage, transformierte Zellen unabhängig der klassischen Kaskaden zum Zelltod zu führen. Dies stellt einen neuen Ansatz für Zelltod induzierende Therapeutika in der Onkologie da. Lungenkrebs hat unter allen Krebserkrankungen die größte Mortalität und zeichnet sich durch einen Mangel an effektiven therapeutischen Möglichkeiten in fortgeschrittenen Stadien aus. Im Rahmen dieser Dissertation wird über die Rezeptor-interagierende Serin/Threonin-Protein-Kinase 3 (RIPK3) und über dem von ihr regulierten immunogenen Zelltod (Nekroptose) als neuen Tumorsuppressor im Adenokarzinom der Lunge berichtet. TNF Faktoren induzieren den nekroptotischen Zelltod durch die Assemblierung der intrazelluläre RIPK1-RIPK3-MLKL Signalachse. Das Schlüsselprotein RIPK3 führt über MLKL zur transmembranösen Porenbildung und durch den entstehenden osmotischen Gradienten zum Anschwellen und Platzen der Zellen. Weiterhin etabliert RIPK3 ein immungenes Transkriptionsprofil in der sterbenden Zelle, was zur Rekrutierung von Immunzellen sowie dem Umbau des Tumor-assoziiertem Immunsystems führt. Durch den nekrotischen Verlust der Membranintegrität kommt es zur Sekretion des intrazellulären Inhalts in die umliegende extrazelluläre Matrix. Unter diesen freigesetzten Molekülen befinden sich Warnstoffe, welche Immunzellen wie gewebeständige Phagozyten rekrutieren und diese zum Abbau der verbleibenden Zellkörper stimulieren. Hierunter fallen auch Tumor-assoziierte Antigene, welche durch Phagozyten als Antigen präsentierende Zellen den Immun-Effektorzellen (T-Zellen, B-Zellen) präsentiert werden. Diese erkennen die Tumorantigene und bauen verbliebene Tumorzellen im Rahmen einer antitumoralen Immunreaktion ab.

Die aufgestellte Hypothese der antitumoralen Nekroptose in LUAD wurde innerhalb RNA sequenzierter, humaner LUAD Datensätze (LUAD-TCGA) und durch LUAD Mausmodelle analysiert. Mittels der TCGA Studienkohorte konnte gezeigt werden, dass hohe *RIPK3* mRNA Level mit einer gesteigerten Expression von Immunsystem regulierenden Genen assoziiert ist. Des Weiteren waren niedrige *RIPK3* mRNA Spiegel mit einer gesteigerten Expression Zellzyklus kontrollierender Gene assoziiert. Durch die Erhebung immunzellspezifischer Scores (Danaher Scores) konnte eine Anreicherung von Immunzellsubpopulationen (Antigen präsentierende Zellen und Effektor Immunzellen) in den Tumorproben mit hoher *RIPK3* Expression

nachgewiesen werden. Zusammenfassend wiesen die Ergebnisse der humanen LUAD Datensätze auf eine tumorsuppressive, immunzellrekrutierende Funktion des *RIPK3* hin.

Im LUAD Mausmodel konnte gezeigt werden, dass fortgeschrittene Dysplasien (Adenome und Adenokarzinome) zumeist eine niedrige RIPK3 Expression zeigen. Dem entgegen hatten frühe Stadien (Bronchiale Hyperplasien) eine überwiegend hohe RIPK3 Expression. In den Adenomen und Adenokarzinomen zeigten Tumore mit niedriger RIPK3 Expression eine größere Tumorfläche als diejenigen mit hoher RIPK3 Expression. Eine hohe RIPK3 Expression führte ebenso zu einer Anreicherung von antitumoralen (iNOS)-positiven Makrophagen (M1-Phänotyp) in den LUAD Tumoren.

Die RIPK3 abhängige Nekroptose wurde als möglicher Ansatzpunkt für Chemotherapeutika evaluiert, um diesen tumorsuppressiven Zelltod therapeutisch nutzbar zu machen. Hierfür wurde vorerst die Expression der nekroptotischen Kaskade (RIPK1-RIPK3-MLKL) auf mRNA und Proteinebene überprüft und Nekroptose in humanen LUAD Zelllinien durch Pharmazeutika und Chemotherapeutika induziert. Es konnte gezeigt werden, dass die meisten LUAD Ziellinien keine detektierbare *RIPK3* mRNA besitzen. Dies spricht für eine Reduktion des Zelltodapparates, um das Überleben der Tumorzellen sicherzustellen. In den Zelllinien mit vorhandener *RIPK3* Expression konnte ein nekroptotischer Zelltod induziert werden. Dies gelang auch in Zelllinien mit einer Apoptose Resistenz. Folglich stellt Nekroptose einen alternativen Zelltod in LUAD dar, welcher durch die Chemotherapeutika Paclitaxel und Pemetrexed induziert werden kann. Dies könnte ein therapeutischer Ansatz zur Induktion der immunogenen Nekroptose als Alternative zur Apoptose sein.

Weitere Untersuchungen sind notwendig, um molekulare Mechanismen der RIPK3 Expression in den Adenokarzinomen aufzudecken und mögliche Ansatzpunkte zur RIPK3 Reexpression zu finden. Auch die gezielte Nekroptoseaktivation *in vivo* ist weiterhin wichtig, um mechanistische Details über suppressive Zellvorgänge und exprimierte Zielgene für antitumorale Immunreaktionen ausfindig zu machen. Die hier präsentierte Dissertation zeigt einen tumorsuppressiven Phänotyp der RIPK3 abhängigen Nekroptose in LUAD, vermittelt durch die Induktion von Zelltod und einer immunogenen Umstrukturierung des tumorassoziierten Immunsystems. Dies könnte einen neuen Ansatz für Immuntherapien im Adenokarzinom der Lunge darstellen, insbesondere da Chemotherapeutika Nekroptose induzieren können.

Abbreviations

A

AAH: Atypical adenomatous hyperplasia

AAV: Adeno-associated virus

AC: Adenocarcinoma

Ad: Adenoma

APC: Antigen-presenting cells

ATP: Adenosine triphosphate

B

BCA: Bicinchoninic acid

BCL2: B-cell lymphoma 2

BH: Bronchial hypoplasia

C

CC10: Club cell protein

CD: Cluster of differentiation

cDNA: Cytosolic Desoxyribonucleic acid

CRC: Colorectal carcinoma

CXCL1: C-X-C Motif Chemokine Ligand 1)

CYLD: Cylindromatosis lysine 63 deubiquitinase

D

DAMP: Damage associated molecular patterns

DC: Dendritic cells

DNMT1: DNA (cytosine-5)-methyltransferase 1

E

EF-1α: Elongation factor 1α

EGFR: Epidermal growth factor receptor

F

F4/80: EGF-like module-containing mucin-like hormone receptor-like 1

FACS: Fluorescence-activated cell sorting

FADD: Fas-associated protein with death domain

G

gDNA: Genomic Desoxyribonucleic acid

GDP: Guanine diphosphate

GEMM: Genetic engineered mouse models

GTP: Guanine triphosphate

GTPase: Guanine triphosphatase

H

HBEC: Human bronchial epithelial cells

HCC: Hepatocellular carcinoma

HE: Hematoxylin and eosin

HRP: Horseradish peroxidase

I

IAP: Inhibitor of apoptosis

IHC: Immunohistochemistry

IL: Interleukin

iNOS: Inducible Nitric Oxidase Synthase

K

KRAS: Kristen rat sarcoma

L

LB media: Luria-Bertani media

LCC: Large cell carcinoma

LUAD: Lung adenocarcinoma

LUSC: Lung squamous cell carcinoma

M

MAPK: Mitogen-activated protein kinase

MDSC: Myeloid derived suppressor cell

MHC: Major histocompatibility complexes

MLKL: Mixed-lineage kinase domain like protein

N

Nec1s: Necrostatin-1s

NF-κB: Nuclear factor kappa B

NLRP3: NLR-family-pyrin-domain-containing 3

NSCLC: Non-small-cell lung cancer

P

PBS: Phosphate buffered saline

PCR: Polymerase chain reaction

PD-L1: Programmed cell death receptor ligand 1

PD1: Programmed cell death 1 receptor

PDA: Pancreatic ductal adenocarcinoma

PI: Propidium Iodide

PLK1: Polo-like-Kinase 1

PRR: Pattern-recognition receptors

R

RHIM: receptor interacting protein homotypic interaction motif

RIPA: Radio-immune precipitation assay

RIPK1/3: Receptor-interacting serine/threonine-protein kinase 1/3

ROS: Reactive oxygen species proto-oncogene

RTK: Receptor tyrosine kinases

S

SCLC: Small-cell lung cancer

SDS-PAGE: Sodium dodecyl sulfate polyacrylamide gel electrophoresis

SMAC: Second mitochondria derived activator of caspase

SOC-media: Super Optimal Broth with Catabolite repression media

SP1: Specificity Protein 1

SPC: Surfactant protein C

STE: Sodium chloride-tris-EDTA buffer

T

TAA: Tumor associated antigen

TAE: Tris-Acetate-EDTA buffer

TAM: Tumor associated macrophage

TBST: Tris-buffered saline with Tween20

TCGA: The cancer genome atlas program

TGF: Tumor growth factor

TIME: Tumor immune microenvironment

TLR: Toll like receptor

TME: Tumor microenvironment

TNF: Tumor necrosis factor

TNFR: Tumor necrosis factor receptor

TP53: Tumor protein P53

TRIF: Toll-interleukin-domain containing adapter inducing interferon-β

TSA: Tumor specific antigen

TSZ: TNF, SMAC, Z-VAD-FMK

W

WPRE: Woodchuck hepatitis virus posttranscriptional regulatory element

Z

Z-VAD-FMK: Carbobenzoxy-valyl-alanyl-aspartyl-[O-methyl]- fluoromethylketone

Reference list

Aaes, T. L., Kaczmarek, A., Delvaeye, T., De Craene, B., De Koker, S., Heyndrickx, L., Delrue, I., Taminau, J., Wiernicki, B., De Groote, P., Garg, A. D., Leybaert, L., Grooten, J., Bertrand, M. J., Agostinis, P., Berx, G., Declercq, W., Vandenabeele, P., & Krysko, D. V. (2016, Apr 12). Vaccination with Necroptotic Cancer Cells Induces Efficient Anti-tumor Immunity. *Cell Rep, 15*(2), 274-287. https://doi.org/10.1016/j.celrep.2016.03.037

Akara-Amornthum, P., Lomphithak, T., Choksi, S., Tohtong, R., & Jitkaew, S. (2020). Key necroptotic proteins are required for Smac mimetic-mediated sensitization of cholangiocarcinoma cells to TNF-alpha and chemotherapeutic gemcitabine-induced necroptosis. *PLoS One, 15*(1), e0227454. https://doi.org/10.1371/journal.pone.0227454

Al-Moujahed, A., Tian, B., Efstathiou, N. E., Konstantinou, E. K., Hoang, M., Lin, H., Miller, J. W., & Vavvas, D. G. (2019, Mar). Receptor interacting protein kinase 3 (RIP3) regulates iPSCs generation through modulating cell cycle progression genes. *Stem Cell Res, 35*, 101387. https://doi.org/10.1016/j.scr.2019.101387

Alexandrov, L. B., Nik-Zainal, S., Wedge, D. C., Aparicio, S. A., Behjati, S., Biankin, A. V., Bignell, G. R., Bolli, N., Borg, A., Borresen-Dale, A. L., Boyault, S., Burkhardt, B., Butler, A. P., Caldas, C., Davies, H. R., Desmedt, C., Eils, R., Eyfjord, J. E., Foekens, J. A., Greaves, M., Hosoda, F., Hutter, B., Ilicic, T., Imbeaud, S., Imielinski, M., Jager, N., Jones, D. T., Jones, D., Knappskog, S., Kool, M., Lakhani, S. R., Lopez-Otin, C., Martin, S., Munshi, N. C., Nakamura, H., Northcott, P. A., Pajic, M., Papaemmanuil, E., Paradiso, A., Pearson, J. V., Puente, X. S., Raine, K., Ramakrishna, M., Richardson, A. L., Richter, J., Rosenstiel, P., Schlesner, M., Schumacher, T. N., Span, P. N., Teague, J. W., Totoki, Y., Tutt, A. N., Valdes-Mas, R., van Buuren, M. M., van 't Veer, L., Vincent-Salomon, A., Waddell, N., Yates, L. R., Australian Pancreatic Cancer Genome, I., Consortium, I. B. C., Consortium, I. M.-S., PedBrain, I., Zucman-Rossi, J., Futreal, P. A., McDermott, U., Lichter, P., Meyerson, M., Grimmond, S. M., Siebert, R., Campo, E., Shibata, T., Pfister, S. M., Campbell, P. J., & Stratton, M. R. (2013, Aug 22). Signatures of mutational processes in human cancer. *Nature, 500*(7463), 415-421. https://doi.org/10.1038/nature12477

Alvarez-Diaz, S., Dillon, C. P., Lalaoui, N., Tanzer, M. C., Rodriguez, D. A., Lin, A., Lebois, M., Hakem, R., Josefsson, E. C., O'Reilly, L. A., Silke, J., Alexander, W. S., Green, D. R., & Strasser, A. (2016, Sep 20). The Pseudokinase MLKL and the Kinase RIPK3 Have Distinct Roles in Autoimmune Disease Caused by Loss of Death-Receptor-Induced Apoptosis. *Immunity, 45*(3), 513-526. https://doi.org/10.1016/j.immuni.2016.07.016

Alvarez-Diaz, S., Preaudet, A., Samson, A. L., Nguyen, P. M., Fung, K. Y., Garnham, A. L., Alexander, W. S., Strasser, A., Ernst, M., Putoczki, T. L., & Murphy, J. M. (2021, May). Necroptosis is dispensable for the development of inflammation-associated or sporadic colon cancer in mice. *Cell Death Differ, 28*(5), 1466-1476. https://doi.org/10.1038/s41418-020-00673-z

Atolia, E., Cesar, S., Arjes, H. A., Rajendram, M., Shi, H., Knapp, B. D., Khare, S., Aranda-Diaz, A., Lenski, R. E., & Huang, K. C. (2020, Oct 20). Environmental and Physiological Factors Affecting High-Throughput Measurements of Bacterial Growth. *mBio, 11*(5). https://doi.org/10.1128/mBio.01378-20

Balachandran, V. P., Luksza, M., Zhao, J. N., Makarov, V., Moral, J. A., Remark, R., Herbst, B., Askan, G., Bhanot, U., Senbabaoglu, Y., Wells, D. K., Cary, C. I. O., Grbovic-Huezo, O., Attiyeh, M., Medina, B., Zhang, J., Loo, J., Saglimbeni, J., Abu-Akeel, M., Zappasodi, R., Riaz, N., Smoragiewicz, M., Kelley, Z. L., Basturk, O., Australian Pancreatic Cancer Genome, I., Garvan Institute of Medical, R., Prince of Wales, H., Royal North Shore, H., University of, G., St Vincent's, H., Institute, Q. B. M. R., University of Melbourne, C. f. C. R., University of Queensland, I. f. M. B., Bankstown, H., Liverpool, H., Royal Prince Alfred Hospital, C. O. B. L., Westmead, H., Fremantle, H., St John of God, H., Royal Adelaide, H., Flinders Medical, C., Envoi, P., Princess Alexandria, H., Austin, H., Johns Hopkins Medical, I., Cancer, A. R.-N. C. f. A. R. o., Gonen, M., Levine, A. J., Allen, P. J., Fearon, D. T., Merad, M., Gnjatic, S., Iacobuzio-

Donahue, C. A., Wolchok, J. D., DeMatteo, R. P., Chan, T. A., Greenbaum, B. D., Merghoub, T., & Leach, S. D. (2017, Nov 23). Identification of unique neoantigen qualities in long-term survivors of pancreatic cancer. *Nature, 551*(7681), 512-516. https://doi.org/10.1038/nature24462

Bentham, R., Litchfield, K., Watkins, T. B. K., Lim, E. L., Rosenthal, R., Martinez-Ruiz, C., Hiley, C. T., Bakir, M. A., Salgado, R., Moore, D. A., Jamal-Hanjani, M., Consortium, T. R., Swanton, C., & McGranahan, N. (2021, Sep). Using DNA sequencing data to quantify T cell fraction and therapy response. *Nature, 597*(7877), 555-560. https://doi.org/10.1038/s41586-021-03894-5

Bergmans, H. E., van Die, I. M., & Hoekstra, W. P. (1981, May). Transformation in Escherichia coli: stages in the process. *J Bacteriol, 146*(2), 564-570. https://doi.org/10.1128/JB.146.2.564-570.1981

Birnboim, H. C., & Doly, J. (1979, Nov 24). A rapid alkaline extraction procedure for screening recombinant plasmid DNA. *Nucleic Acids Res, 7*(6), 1513-1523. https://doi.org/10.1093/nar/7.6.1513

Bozec, D., Iuga, A. C., Roda, G., Dahan, S., & Yeretssian, G. (2016, Jul 19). Critical function of the necroptosis adaptor RIPK3 in protecting from intestinal tumorigenesis. *Oncotarget, 7*(29), 46384-46400. https://doi.org/10.18632/oncotarget.10135

Brown, S. D., Warren, R. L., Gibb, E. A., Martin, S. D., Spinelli, J. J., Nelson, B. H., & Holt, R. A. (2014, May). Neo-antigens predicted by tumor genome meta-analysis correlate with increased patient survival. *Genome Res, 24*(5), 743-750. https://doi.org/10.1101/gr.165985.113

Cai, Z., Jitkaew, S., Zhao, J., Chiang, H. C., Choksi, S., Liu, J., Ward, Y., Wu, L. G., & Liu, Z. G. (2014, Jan). Plasma membrane translocation of trimerized MLKL protein is required for TNF-induced necroptosis. *Nat Cell Biol, 16*(1), 55-65. https://doi.org/10.1038/ncb2883

Cai, Z., Zhang, A., Choksi, S., Li, W., Li, T., Zhang, X. M., & Liu, Z. G. (2016, Aug). Activation of cell-surface proteases promotes necroptosis, inflammation and cell migration. *Cell Res, 26*(8), 886-900. https://doi.org/10.1038/cr.2016.87

Campbell, J. D., Alexandrov, A., Kim, J., Wala, J., Berger, A. H., Pedamallu, C. S., Shukla, S. A., Guo, G., Brooks, A. N., Murray, B. A., Imielinski, M., Hu, X., Ling, S., Akbani, R., Rosenberg, M., Cibulskis, C., Ramachandran, A., Collisson, E. A., Kwiatkowski, D. J., Lawrence, M. S., Weinstein, J. N., Verhaak, R. G., Wu, C. J., Hammerman, P. S., Cherniack, A. D., Getz, G., Cancer Genome Atlas Research, N., Artyomov, M. N., Schreiber, R., Govindan, R., & Meyerson, M. (2016, Jun). Distinct patterns of somatic genome alterations in lung adenocarcinomas and squamous cell carcinomas. *Nat Genet, 48*(6), 607-616. https://doi.org/10.1038/ng.3564

Cancer Genome Atlas Research, N. (2014, Jul 31). Comprehensive molecular profiling of lung adenocarcinoma. *Nature, 511*(7511), 543-550. https://doi.org/10.1038/nature13385

Casanova-Acebes, M., Dalla, E., Leader, A. M., LeBerichel, J., Nikolic, J., Morales, B. M., Brown, M., Chang, C., Troncoso, L., Chen, S. T., Sastre-Perona, A., Park, M. D., Tabachnikova, A., Dhainaut, M., Hamon, P., Maier, B., Sawai, C. M., Agullo-Pascual, E., Schober, M., Brown, B. D., Reizis, B., Marron, T., Kenigsberg, E., Moussion, C., Benaroch, P., Aguirre-Ghiso, J. A., & Merad, M. (2021, Jul). Tissue-resident macrophages provide a pro-tumorigenic niche to early NSCLC cells. *Nature, 595*(7868), 578-584. https://doi.org/10.1038/s41586-021-03651-8

Chen, W. J., Ho, C. C., Chang, Y. L., Chen, H. Y., Lin, C. A., Ling, T. Y., Yu, S. L., Yuan, S. S., Chen, Y. J., Lin, C. Y., Pan, S. H., Chou, H. Y., Chen, Y. J., Chang, G. C., Chu, W. C., Lee, Y. M., Lee, J. Y., Lee, P. J., Li, K. C., Chen, H. W., & Yang, P. C. (2014, Mar 25). Cancer-associated fibroblasts regulate the plasticity of lung cancer stemness via paracrine signalling. *Nat Commun, 5*, 3472. https://doi.org/10.1038/ncomms4472

Chen, X., Li, W., Ren, J., Huang, D., He, W. T., Song, Y., Yang, C., Li, W., Zheng, X., Chen, P., & Han, J. (2014, Jan). Translocation of mixed lineage kinase domain-like protein to plasma membrane leads to necrotic cell death. *Cell Res, 24*(1), 105-121. https://doi.org/10.1038/cr.2013.171

Cho, Y. S., Challa, S., Moquin, D., Genga, R., Ray, T. D., Guildford, M., & Chan, F. K. (2009, Jun 12). Phosphorylation-driven assembly of the RIP1-RIP3 complex regulates programmed necrosis and virus-induced inflammation. *Cell, 137*(6), 1112-1123. https://doi.org/10.1016/j.cell.2009.05.037

Chomczynski, P., & Sacchi, N. (1987, Apr). Single-step method of RNA isolation by acid guanidinium thiocyanate-phenol-chloroform extraction. *Anal Biochem, 162*(1), 156-159. https://doi.org/10.1006/abio.1987.9999

Chung, F. T., Lee, K. Y., Wang, C. W., Heh, C. C., Chan, Y. F., Chen, H. W., Kuo, C. H., Feng, P. H., Lin, T. Y., Wang, C. H., Chou, C. L., Chen, H. C., Lin, S. M., & Kuo, H. P. (2012, Aug 1). Tumor-associated macrophages correlate with response to epidermal growth factor receptor-tyrosine kinase inhibitors in advanced non-small cell lung cancer. *Int J Cancer, 131*(3), E227-235. https://doi.org/10.1002/ijc.27403

Colbert, L. E., Fisher, S. B., Hardy, C. W., Hall, W. A., Saka, B., Shelton, J. W., Petrova, A. V., Warren, M. D., Pantazides, B. G., Gandhi, K., Kowalski, J., Kooby, D. A., El-Rayes, B. F., Staley, C. A., 3rd, Adsay, N. V., Curran, W. J., Jr., Landry, J. C., Maithel, S. K., & Yu, D. S. (2013, Sep 1). Pronecrotic mixed lineage kinase domain-like protein expression is a prognostic biomarker in patients with early-stage resected pancreatic adenocarcinoma. *Cancer, 119*(17), 3148-3155. https://doi.org/10.1002/cncr.28144

Colijn, S., Gao, S., Ingram, K. G., Menendez, M., Muthukumar, V., Silasi-Mansat, R., Chmielewska, J. J., Hinsdale, M., Lupu, F., & Griffin, C. T. (2020, Feb). The NuRD chromatin-remodeling complex enzyme CHD4 prevents hypoxia-induced endothelial Ripk3 transcription and murine embryonic vascular rupture. *Cell Death Differ, 27*(2), 618-631. https://doi.org/10.1038/s41418-019-0376-8

Conev, N. V., Dimitrova, E. G., Bogdanova, M. K., Kashlov, Y. K., Chaushev, B. G., Radanova, M. A., Petrov, D. P., Georgiev, K. D., Bachvarov, C. H., Todorov, G. N., Kalchev, K. P., Popov, H. B., Manev, R. R., & Donev, I. S. (2019, Mar 23). RIPK3 expression as a potential predictive and prognostic marker in metastatic colon cancer. *Clin Invest Med, 42*(1), E31-E38. https://doi.org/10.25011/cim.v42i1.32390

Conos, S. A., Chen, K. W., De Nardo, D., Hara, H., Whitehead, L., Nunez, G., Masters, S. L., Murphy, J. M., Schroder, K., Vaux, D. L., Lawlor, K. E., Lindqvist, L. M., & Vince, J. E. (2017, Feb 7). Active MLKL triggers the NLRP3 inflammasome in a cell-intrinsic manner. *Proc Natl Acad Sci U S A, 114*(6), E961-E969. https://doi.org/10.1073/pnas.1613305114

Dai, F., Liu, L., Che, G., Yu, N., Pu, Q., Zhang, S., Ma, J., Ma, L., & You, Z. (2010, May 20). The number and microlocalization of tumor-associated immune cells are associated with patient's survival time in non-small cell lung cancer. *BMC Cancer, 10*, 220. https://doi.org/10.1186/1471-2407-10-220

Danaher, P., Warren, S., Dennis, L., D'Amico, L., White, A., Disis, M. L., Geller, M. A., Odunsi, K., Beechem, J., & Fling, S. P. (2017). Gene expression markers of Tumor Infiltrating Leukocytes. *J Immunother Cancer, 5*, 18. https://doi.org/10.1186/s40425-017-0215-8

Desai, T. J., Brownfield, D. G., & Krasnow, M. A. (2014, Mar 13). Alveolar progenitor and stem cells in lung development, renewal and cancer. *Nature, 507*(7491), 190-194. https://doi.org/10.1038/nature12930

Devesa, S. S., Bray, F., Vizcaino, A. P., & Parkin, D. M. (2005, Nov 1). International lung cancer trends by histologic type: male:female differences diminishing and adenocarcinoma rates rising. *Int J Cancer, 117*(2), 294-299. https://doi.org/10.1002/ijc.21183

Dimitrova, N., Gocheva, V., Bhutkar, A., Resnick, R., Jong, R. M., Miller, K. M., Bendor, J., & Jacks, T. (2016, Feb). Stromal Expression of miR-143/145 Promotes Neoangiogenesis in Lung Cancer Development. *Cancer Discov, 6*(2), 188-201. https://doi.org/10.1158/2159-8290.CD-15-0854

Ding, L., Getz, G., Wheeler, D. A., Mardis, E. R., McLellan, M. D., Cibulskis, K., Sougnez, C., Greulich, H., Muzny, D. M., Morgan, M. B., Fulton, L., Fulton, R. S., Zhang, Q., Wendl, M. C., Lawrence, M. S., Larson, D. E., Chen, K., Dooling, D. J., Sabo, A., Hawes, A. C., Shen, H., Jhangiani, S. N., Lewis, L. R., Hall, O., Zhu, Y., Mathew, T., Ren, Y., Yao, J., Scherer, S. E., Clerc, K., Metcalf, G. A., Ng, B., Milosavljevic, A., Gonzalez-Garay, M. L., Osborne, J. R., Meyer, R., Shi, X., Tang, Y., Koboldt, D. C., Lin, L., Abbott, R., Miner, T. L., Pohl, C., Fewell, G., Haipek, C., Schmidt, H., Dunford-Shore, B. H., Kraja, A., Crosby, S. D., Sawyer, C. S., Vickery, T., Sander, S., Robinson, J., Winckler, W., Baldwin, J., Chirieac, L. R., Dutt, A., Fennell, T., Hanna, M., Johnson, B. E., Onofrio, R. C., Thomas, R. K., Tonon, G., Weir, B. A., Zhao, X., Ziaugra, L., Zody, M. C.,

Giordano, T., Orringer, M. B., Roth, J. A., Spitz, M. R., Wistuba, II, Ozenberger, B., Good, P. J., Chang, A. C., Beer, D. G., Watson, M. A., Ladanyi, M., Broderick, S., Yoshizawa, A., Travis, W. D., Pao, W., Province, M. A., Weinstock, G. M., Varmus, H. E., Gabriel, S. B., Lander, E. S., Gibbs, R. A., Meyerson, M., & Wilson, R. K. (2008, Oct 23). Somatic mutations affect key pathways in lung adenocarcinoma. *Nature, 455*(7216), 1069-1075. https://doi.org/10.1038/nature07423

Dondelinger, Y., Declercq, W., Montessuit, S., Roelandt, R., Goncalves, A., Bruggeman, I., Hulpiau, P., Weber, K., Sehon, C. A., Marquis, R. W., Bertin, J., Gough, P. J., Savvides, S., Martinou, J. C., Bertrand, M. J., & Vandenabeele, P. (2014, May 22). MLKL compromises plasma membrane integrity by binding to phosphatidylinositol phosphates. *Cell Rep, 7*(4), 971-981. https://doi.org/10.1016/j.celrep.2014.04.026

DuPage, M., Mazumdar, C., Schmidt, L. M., Cheung, A. F., & Jacks, T. (2012, Feb 8). Expression of tumour-specific antigens underlies cancer immunoediting. *Nature, 482*(7385), 405-409. https://doi.org/10.1038/nature10803

Ertao, Z., Jianhui, C., Kang, W., Zhijun, Y., Hui, W., Chuangqi, C., Changjiang, Q., Sile, C., Yulong, H., & Shirong, C. (2016, Oct). Prognostic value of mixed lineage kinase domain-like protein expression in the survival of patients with gastric caner. *Tumour Biol, 37*(10), 13679-13685. https://doi.org/10.1007/s13277-016-5229-1

Feng, X., Song, Q., Yu, A., Tang, H., Peng, Z., & Wang, X. (2015). Receptor-interacting protein kinase 3 is a predictor of survival and plays a tumor suppressive role in colorectal cancer. *Neoplasma, 62*(4), 592-601. https://doi.org/10.4149/neo_2015_071

Ferlay, J., Colombet, M., Soerjomataram, I., Mathers, C., Parkin, D. M., Pineros, M., Znaor, A., & Bray, F. (2019, Apr 15). Estimating the global cancer incidence and mortality in 2018: GLOBOCAN sources and methods. *Int J Cancer, 144*(8), 1941-1953. https://doi.org/10.1002/ijc.31937

Ferlay, J., Soerjomataram, I., Dikshit, R., Eser, S., Mathers, C., Rebelo, M., Parkin, D. M., Forman, D., & Bray, F. (2015, Mar 1). Cancer incidence and mortality worldwide: sources, methods and major patterns in GLOBOCAN 2012. *Int J Cancer, 136*(5), E359-386. https://doi.org/10.1002/ijc.29210

Fetics, S. K., Guterres, H., Kearney, B. M., Buhrman, G., Ma, B., Nussinov, R., & Mattos, C. (2015, Mar 3). Allosteric effects of the oncogenic RasQ61L mutant on Raf-RBD. *Structure, 23*(3), 505-516. https://doi.org/10.1016/j.str.2014.12.017

Fischer-Riepe, L., Daber, N., Schulte-Schrepping, J., Veras De Carvalho, B. C., Russo, A., Pohlen, M., Fischer, J., Chasan, A. I., Wolf, M., Ulas, T., Glander, S., Schulz, C., Skryabin, B., Wollbrink Dipl-Ing, A., Steingraeber, N., Stremmel, C., Koehle, M., Gartner, F., Vettorazzi, S., Holzinger, D., Gross, J., Rosenbauer, F., Stoll, M., Niemann, S., Tuckermann, J., Schultze, J. L., Roth, J., & Barczyk-Kahlert, K. (2020, Nov). CD163 expression defines specific, IRF8-dependent, immune-modulatory macrophages in the bone marrow. *J Allergy Clin Immunol, 146*(5), 1137-1151. https://doi.org/10.1016/j.jaci.2020.02.034

Freeman, B. E., Meyer, C., & Slifka, M. K. (2014, Jul). Anti-inflammatory cytokines directly inhibit innate but not adaptive CD8+ T cell functions. *J Virol, 88*(13), 7474-7484. https://doi.org/10.1128/JVI.00658-14

Fritsch, M., Gunther, S. D., Schwarzer, R., Albert, M. C., Schorn, F., Werthenbach, J. P., Schiffmann, L. M., Stair, N., Stocks, H., Seeger, J. M., Lamkanfi, M., Kronke, M., Pasparakis, M., & Kashkar, H. (2019, Nov). Caspase-8 is the molecular switch for apoptosis, necroptosis and pyroptosis. *Nature, 575*(7784), 683-687. https://doi.org/10.1038/s41586-019-1770-6

Galluzzi, L., Vitale, I., Aaronson, S. A., Abrams, J. M., Adam, D., Agostinis, P., Alnemri, E. S., Altucci, L., Amelio, I., Andrews, D. W., Annicchiarico-Petruzzelli, M., Antonov, A. V., Arama, E., Baehrecke, E. H., Barlev, N. A., Bazan, N. G., Bernassola, F., Bertrand, M. J. M., Bianchi, K., Blagosklonny, M. V., Blomgren, K., Borner, C., Boya, P., Brenner, C., Campanella, M., Candi, E., Carmona-Gutierrez, D., Cecconi, F., Chan, F. K., Chandel, N. S., Cheng, E. H., Chipuk, J. E., Cidlowski, J. A., Ciechanover, A., Cohen, G. M., Conrad, M., Cubillos-Ruiz, J. R., Czabotar, P. E., D'Angiolella, V., Dawson, T. M., Dawson, V. L., De Laurenzi, V., De Maria, R., Debatin, K. M., DeBerardinis, R. J., Deshmukh, M., Di Daniele, N., Di Virgilio, F., Dixit, V. M., Dixon, S. J.,

Duckett, C. S., Dynlacht, B. D., El-Deiry, W. S., Elrod, J. W., Fimia, G. M., Fulda, S., Garcia-Saez, A. J., Garg, A. D., Garrido, C., Gavathiotis, E., Golstein, P., Gottlieb, E., Green, D. R., Greene, L. A., Gronemeyer, H., Gross, A., Hajnoczky, G., Hardwick, J. M., Harris, I. S., Hengartner, M. O., Hetz, C., Ichijo, H., Jaattela, M., Joseph, B., Jost, P. J., Juin, P. P., Kaiser, W. J., Karin, M., Kaufmann, T., Kepp, O., Kimchi, A., Kitsis, R. N., Klionsky, D. J., Knight, R. A., Kumar, S., Lee, S. W., Lemasters, J. J., Levine, B., Linkermann, A., Lipton, S. A., Lockshin, R. A., Lopez-Otin, C., Lowe, S. W., Luedde, T., Lugli, E., MacFarlane, M., Madeo, F., Malewicz, M., Malorni, W., Manic, G., Marine, J. C., Martin, S. J., Martinou, J. C., Medema, J. P., Mehlen, P., Meier, P., Melino, S., Miao, E. A., Molkentin, J. D., Moll, U. M., Munoz-Pinedo, C., Nagata, S., Nunez, G., Oberst, A., Oren, M., Overholtzer, M., Pagano, M., Panaretakis, T., Pasparakis, M., Penninger, J. M., Pereira, D. M., Pervaiz, S., Peter, M. E., Piacentini, M., Pinton, P., Prehn, J. H. M., Puthalakath, H., Rabinovich, G. A., Rehm, M., Rizzuto, R., Rodrigues, C. M. P., Rubinsztein, D. C., Rudel, T., Ryan, K. M., Sayan, E., Scorrano, L., Shao, F., Shi, Y., Silke, J., Simon, H. U., Sistigu, A., Stockwell, B. R., Strasser, A., Szabadkai, G., Tait, S. W. G., Tang, D., Tavernarakis, N., Thorburn, A., Tsujimoto, Y., Turk, B., Vanden Berghe, T., Vandenabeele, P., Vander Heiden, M. G., Villunger, A., Virgin, H. W., Vousden, K. H., Vucic, D., Wagner, E. F., Walczak, H., Wallach, D., Wang, Y., Wells, J. A., Wood, W., Yuan, J., Zakeri, Z., Zhivotovsky, B., Zitvogel, L., Melino, G., & Kroemer, G. (2018, Mar). Molecular mechanisms of cell death: recommendations of the Nomenclature Committee on Cell Death 2018. *Cell Death Differ, 25*(3), 486-541. https://doi.org/10.1038/s41418-017-0012-4

Geserick, P., Wang, J., Schilling, R., Horn, S., Harris, P. A., Bertin, J., Gough, P. J., Feoktistova, M., & Leverkus, M. (2015, Sep 10). Absence of RIPK3 predicts necroptosis resistance in malignant melanoma. *Cell Death Dis, 6*, e1884. https://doi.org/10.1038/cddis.2015.240

Goldstraw, P., Chansky, K., Crowley, J., Rami-Porta, R., Asamura, H., Eberhardt, W. E., Nicholson, A. G., Groome, P., Mitchell, A., Bolejack, V., International Association for the Study of Lung Cancer, S., Prognostic Factors Committee, A. B., Participating, I., International Association for the Study of Lung Cancer, S., Prognostic Factors Committee Advisory, B., & Participating, I. (2016, Jan). The IASLC Lung Cancer Staging Project: Proposals for Revision of the TNM Stage Groupings in the Forthcoming (Eighth) Edition of the TNM Classification for Lung Cancer. *J Thorac Oncol, 11*(1), 39-51. https://doi.org/10.1016/j.jtho.2015.09.009

Gottfried, E., Kunz-Schughart, L. A., Weber, A., Rehli, M., Peuker, A., Muller, A., Kastenberger, M., Brockhoff, G., Andreesen, R., & Kreutz, M. (2008, May). Expression of CD68 in non-myeloid cell types. *Scand J Immunol, 67*(5), 453-463. https://doi.org/10.1111/j.1365-3083.2008.02091.x

Guerra, C., Mijimolle, N., Dhawahir, A., Dubus, P., Barradas, M., Serrano, M., Campuzano, V., & Barbacid, M. (2003, Aug). Tumor induction by an endogenous K-ras oncogene is highly dependent on cellular context. *Cancer Cell, 4*(2), 111-120. https://doi.org/10.1016/s1535-6108(03)00191-0

Gupta, K., & Liu, B. (2021, Apr 23). PLK1-mediated S369 phosphorylation of RIPK3 during G2 and M phases enables its ripoptosome incorporation and activity. *iScience, 24*(4), 102320. https://doi.org/10.1016/j.isci.2021.102320

Hanahan, D. (1983, Jun 5). Studies on transformation of Escherichia coli with plasmids. *J Mol Biol, 166*(4), 557-580. https://doi.org/10.1016/s0022-2836(83)80284-8

Hanahan, D., & Weinberg, R. A. (2000, Jan 7). The hallmarks of cancer. *Cell, 100*(1), 57-70. https://doi.org/10.1016/s0092-8674(00)81683-9

Hanahan, D., & Weinberg, R. A. (2011, Mar 4). Hallmarks of cancer: the next generation. *Cell, 144*(5), 646-674. https://doi.org/10.1016/j.cell.2011.02.013

He, S., Liang, Y., Shao, F., & Wang, X. (2011, Dec 13). Toll-like receptors activate programmed necrosis in macrophages through a receptor-interacting kinase-3-mediated pathway. *Proc Natl Acad Sci U S A, 108*(50), 20054-20059. https://doi.org/10.1073/pnas.1116302108

He, S., Wang, L., Miao, L., Wang, T., Du, F., Zhao, L., & Wang, X. (2009, Jun 12). Receptor interacting protein kinase-3 determines cellular necrotic response to TNF-alpha. *Cell, 137*(6), 1100-1111. https://doi.org/10.1016/j.cell.2009.05.021

Hellmann, M. D., Paz-Ares, L., Bernabe Caro, R., Zurawski, B., Kim, S. W., Carcereny Costa, E., Park, K., Alexandru, A., Lupinacci, L., de la Mora Jimenez, E., Sakai, H., Albert, I., Vergnenegre, A., Peters, S., Syrigos, K., Barlesi, F., Reck, M., Borghaei, H., Brahmer, J. R., O'Byrne, K. J., Geese, W. J., Bhagavatheeswaran, P., Rabindran, S. K., Kasinathan, R. S., Nathan, F. E., & Ramalingam, S. S. (2019, Nov 21). Nivolumab plus Ipilimumab in Advanced Non-Small-Cell Lung Cancer. *N Engl J Med, 381*(21), 2020-2031. https://doi.org/10.1056/NEJMoa1910231

Hu, G., Su, Y., Kang, B. H., Fan, Z., Dong, T., Brown, D. R., Cheah, J., Wittrup, K. D., & Chen, J. (2021, Feb 3). High-throughput phenotypic screen and transcriptional analysis identify new compounds and targets for macrophage reprogramming. *Nat Commun, 12*(1), 773. https://doi.org/10.1038/s41467-021-21066-x

Huang, C. Y., Kuo, W. T., Huang, Y. C., Lee, T. C., & Yu, L. C. (2013, May 2). Resistance to hypoxia-induced necroptosis is conferred by glycolytic pyruvate scavenging of mitochondrial superoxide in colorectal cancer cells. *Cell Death Dis, 4*, e622. https://doi.org/10.1038/cddis.2013.149

Huang, D., Zheng, X., Wang, Z. A., Chen, X., He, W. T., Zhang, Y., Xu, J. G., Zhao, H., Shi, W., Wang, X., Zhu, Y., & Han, J. (2017, Mar 1). The MLKL Channel in Necroptosis Is an Octamer Formed by Tetramers in a Dyadic Process. *Mol Cell Biol, 37*(5). https://doi.org/10.1128/MCB.00497-16

Jackson, E. L., Willis, N., Mercer, K., Bronson, R. T., Crowley, D., Montoya, R., Jacks, T., & Tuveson, D. A. (2001, Dec 15). Analysis of lung tumor initiation and progression using conditional expression of oncogenic K-ras. *Genes Dev, 15*(24), 3243-3248. https://doi.org/10.1101/gad.943001

Jamal-Hanjani, M., Wilson, G. A., McGranahan, N., Birkbak, N. J., Watkins, T. B. K., Veeriah, S., Shafi, S., Johnson, D. H., Mitter, R., Rosenthal, R., Salm, M., Horswell, S., Escudero, M., Matthews, N., Rowan, A., Chambers, T., Moore, D. A., Turajlic, S., Xu, H., Lee, S. M., Forster, M. D., Ahmad, T., Hiley, C. T., Abbosh, C., Falzon, M., Borg, E., Marafioti, T., Lawrence, D., Hayward, M., Kolvekar, S., Panagiotopoulos, N., Janes, S. M., Thakrar, R., Ahmed, A., Blackhall, F., Summers, Y., Shah, R., Joseph, L., Quinn, A. M., Crosbie, P. A., Naidu, B., Middleton, G., Langman, G., Trotter, S., Nicolson, M., Remmen, H., Kerr, K., Chetty, M., Gomersall, L., Fennell, D. A., Nakas, A., Rathinam, S., Anand, G., Khan, S., Russell, P., Ezhil, V., Ismail, B., Irvin-Sellers, M., Prakash, V., Lester, J. F., Kornaszewska, M., Attanoos, R., Adams, H., Davies, H., Dentro, S., Taniere, P., O'Sullivan, B., Lowe, H. L., Hartley, J. A., Iles, N., Bell, H., Ngai, Y., Shaw, J. A., Herrero, J., Szallasi, Z., Schwarz, R. F., Stewart, A., Quezada, S. A., Le Quesne, J., Van Loo, P., Dive, C., Hackshaw, A., Swanton, C., & Consortium, T. R. (2017, Jun 1). Tracking the Evolution of Non-Small-Cell Lung Cancer. *N Engl J Med, 376*(22), 2109-2121. https://doi.org/10.1056/NEJMoa1616288

Janne, P. A., Yang, J. C., Kim, D. W., Planchard, D., Ohe, Y., Ramalingam, S. S., Ahn, M. J., Kim, S. W., Su, W. C., Horn, L., Haggstrom, D., Felip, E., Kim, J. H., Frewer, P., Cantarini, M., Brown, K. H., Dickinson, P. A., Ghiorghiu, S., & Ranson, M. (2015, Apr 30). AZD9291 in EGFR inhibitor-resistant non-small-cell lung cancer. *N Engl J Med, 372*(18), 1689-1699. https://doi.org/10.1056/NEJMoa1411817

Jayakumar, A., & Bothwell, A. L. M. (2019, Apr 1). RIPK3-Induced Inflammation by I-MDSCs Promotes Intestinal Tumors. *Cancer Res, 79*(7), 1587-1599. https://doi.org/10.1158/0008-5472.CAN-18-2153

Ji, H. (2010, Aug 1). Lysis of cultured cells for immunoprecipitation. *Cold Spring Harb Protoc, 2010*(8), pdb prot5466. https://doi.org/10.1101/pdb.prot5466

Kadota, K., Nitadori, J., Rekhtman, N., Jones, D. R., Adusumilli, P. S., & Travis, W. D. (2015, Sep). Reevaluation and reclassification of resected lung carcinomas originally diagnosed as squamous cell carcinoma using immunohistochemical analysis. *Am J Surg Pathol, 39*(9), 1170-1180. https://doi.org/10.1097/PAS.0000000000000439

Kadota, K., Nitadori, J., Woo, K. M., Sima, C. S., Finley, D. J., Rusch, V. W., Adusumilli, P. S., & Travis, W. D. (2014, Aug). Comprehensive pathological analyses in lung squamous cell carcinoma: single cell invasion, nuclear diameter, and tumor budding are independent prognostic factors for worse outcomes. *J Thorac Oncol, 9*(8), 1126-1139. https://doi.org/10.1097/JTO.0000000000000253

Kaiser, W. J., Sridharan, H., Huang, C., Mandal, P., Upton, J. W., Gough, P. J., Sehon, C. A., Marquis, R. W., Bertin, J., & Mocarski, E. S. (2013, Oct 25). Toll-like receptor 3-mediated necrosis via TRIF, RIP3, and MLKL. *J Biol Chem, 288*(43), 31268-31279. https://doi.org/10.1074/jbc.M113.462341

Kaiser, W. J., Upton, J. W., Long, A. B., Livingston-Rosanoff, D., Daley-Bauer, L. P., Hakem, R., Caspary, T., & Mocarski, E. S. (2011, Mar 17). RIP3 mediates the embryonic lethality of caspase-8-deficient mice. *Nature, 471*(7338), 368-372. https://doi.org/10.1038/nature09857

Kang, T., Huang, Y., Zhu, Q., Cheng, H., Pei, Y., Feng, J., Xu, M., Jiang, G., Song, Q., Jiang, T., Chen, H., Gao, X., & Chen, J. (2018, May). Necroptotic cancer cells-mimicry nanovaccine boosts anti-tumor immunity with tailored immune-stimulatory modality. *Biomaterials, 164*, 80-97. https://doi.org/10.1016/j.biomaterials.2018.02.033

Kang, T. B., Yang, S. H., Toth, B., Kovalenko, A., & Wallach, D. (2013, Jan 24). Caspase-8 blocks kinase RIPK3-mediated activation of the NLRP3 inflammasome. *Immunity, 38*(1), 27-40. https://doi.org/10.1016/j.immuni.2012.09.015

Kangas, L., Gronroos, M., & Nieminen, A. L. (1984). Bioluminescence of cellular ATP: a new method for evaluating cytotoxic agents in vitro. *Med Biol, 62*(6), 338-343. https://www.ncbi.nlm.nih.gov/pubmed/6543460

Karanikas, V., Tsochas, S., Boukas, K., Kerenidi, T., Nakou, M., Dahabreh, J., Poularakis, T., Gourgoulianis, K. I., & Germenis, A. E. (2008, Mar). Co-expression patterns of tumor-associated antigen genes by non-small cell lung carcinomas: implications for immunotherapy. *Cancer Biol Ther, 7*(3), 345-352. https://doi.org/10.4161/cbt.7.3.5424

Ke, H., Augustine, C. K., Gandham, V. D., Jin, J. Y., Tyler, D. S., Akiyama, S. K., Hall, R. P., & Zhang, J. Y. (2013, Jan). CYLD inhibits melanoma growth and progression through suppression of the JNK/AP-1 and beta1-integrin signaling pathways. *J Invest Dermatol, 133*(1), 221-229. https://doi.org/10.1038/jid.2012.253

Kenter, G. G., Welters, M. J., Valentijn, A. R., Lowik, M. J., Berends-van der Meer, D. M., Vloon, A. P., Essahsah, F., Fathers, L. M., Offringa, R., Drijfhout, J. W., Wafelman, A. R., Oostendorp, J., Fleuren, G. J., van der Burg, S. H., & Melief, C. J. (2009, Nov 5). Vaccination against HPV-16 oncoproteins for vulvar intraepithelial neoplasia. *N Engl J Med, 361*(19), 1838-1847. https://doi.org/10.1056/NEJMoa0810097

Kim, C. F., Jackson, E. L., Woolfenden, A. E., Lawrence, S., Babar, I., Vogel, S., Crowley, D., Bronson, R. T., & Jacks, T. (2005, Jun 17). Identification of bronchioalveolar stem cells in normal lung and lung cancer. *Cell, 121*(6), 823-835. https://doi.org/10.1016/j.cell.2005.03.032

Kim, D. W., Min, H. S., Lee, K. H., Kim, Y. J., Oh, D. Y., Jeon, Y. K., Lee, S. H., Im, S. A., Chung, D. H., Kim, Y. T., Kim, T. Y., Bang, Y. J., Sung, S. W., Kim, J. H., & Heo, D. S. (2008, Mar 25). High tumour islet macrophage infiltration correlates with improved patient survival but not with EGFR mutations, gene copy number or protein expression in resected non-small cell lung cancer. *Br J Cancer, 98*(6), 1118-1124. https://doi.org/10.1038/sj.bjc.6604256

Koo, G. B., Morgan, M. J., Lee, D. G., Kim, W. J., Yoon, J. H., Koo, J. S., Kim, S. I., Kim, S. J., Son, M. K., Hong, S. S., Levy, J. M., Pollyea, D. A., Jordan, C. T., Yan, P., Frankhouser, D., Nicolet, D., Maharry, K., Marcucci, G., Choi, K. S., Cho, H., Thorburn, A., & Kim, Y. S. (2015, Jun). Methylation-dependent loss of RIP3 expression in cancer represses programmed necrosis in response to chemotherapeutics. *Cell Res, 25*(6), 707-725. https://doi.org/10.1038/cr.2015.56

Kwon, M. C., & Berns, A. (2013, Apr). Mouse models for lung cancer. *Mol Oncol, 7*(2), 165-177. https://doi.org/10.1016/j.molonc.2013.02.010

Laemmli, U. K. (1970, Aug 15). Cleavage of structural proteins during the assembly of the head of bacteriophage T4. *Nature, 227*(5259), 680-685. https://doi.org/10.1038/227680a0

Laird, P. W., Zijderveld, A., Linders, K., Rudnicki, M. A., Jaenisch, R., & Berns, A. (1991, Aug 11). Simplified mammalian DNA isolation procedure. *Nucleic Acids Res, 19*(15), 4293. https://doi.org/10.1093/nar/19.15.4293

Lau, S. K., Chu, P. G., & Weiss, L. M. (2004, Nov). CD163: a specific marker of macrophages in paraffin-embedded tissue samples. *Am J Clin Pathol, 122*(5), 794-801. https://doi.org/10.1309/QHD6-YFN8-1KQX-UUH6

Lawlor, K. E., Khan, N., Mildenhall, A., Gerlic, M., Croker, B. A., D'Cruz, A. A., Hall, C., Kaur Spall, S., Anderton, H., Masters, S. L., Rashidi, M., Wicks, I. P., Alexander, W. S., Mitsuuchi, Y., Benetatos, C. A., Condon, S. M., Wong, W. W., Silke, J., Vaux, D. L., & Vince, J. E. (2015, Feb 18). RIPK3 promotes cell death and NLRP3 inflammasome activation in the absence of MLKL. *Nat Commun, 6*, 6282. https://doi.org/10.1038/ncomms7282

Lawrence, M. S., Stojanov, P., Polak, P., Kryukov, G. V., Cibulskis, K., Sivachenko, A., Carter, S. L., Stewart, C., Mermel, C. H., Roberts, S. A., Kiezun, A., Hammerman, P. S., McKenna, A., Drier, Y., Zou, L., Ramos, A. H., Pugh, T. J., Stransky, N., Helman, E., Kim, J., Sougnez, C., Ambrogio, L., Nickerson, E., Shefler, E., Cortes, M. L., Auclair, D., Saksena, G., Voet, D., Noble, M., DiCara, D., Lin, P., Lichtenstein, L., Heiman, D. I., Fennell, T., Imielinski, M., Hernandez, B., Hodis, E., Baca, S., Dulak, A. M., Lohr, J., Landau, D. A., Wu, C. J., Melendez-Zajgla, J., Hidalgo-Miranda, A., Koren, A., McCarroll, S. A., Mora, J., Crompton, B., Onofrio, R., Parkin, M., Winckler, W., Ardlie, K., Gabriel, S. B., Roberts, C. W. M., Biegel, J. A., Stegmaier, K., Bass, A. J., Garraway, L. A., Meyerson, M., Golub, T. R., Gordenin, D. A., Sunyaev, S., Lander, E. S., & Getz, G. (2013, Jul 11). Mutational heterogeneity in cancer and the search for new cancer-associated genes. *Nature, 499*(7457), 214-218. https://doi.org/10.1038/nature12213

Lee, C., Jeong, H., Bae, Y., Shin, K., Kang, S., Kim, H., Oh, J., & Bae, H. (2019, Jun 7). Targeting of M2-like tumor-associated macrophages with a melittin-based pro-apoptotic peptide. *J Immunother Cancer, 7*(1), 147. https://doi.org/10.1186/s40425-019-0610-4

Lee, S. B., Kim, J. J., Han, S. A., Fan, Y., Guo, L. S., Aziz, K., Nowsheen, S., Kim, S. S., Park, S. Y., Luo, Q., Chung, J. O., Choi, S. I., Aziz, A., Yin, P., Tong, S. Y., Fiesel, F. C., Springer, W., Zhang, J. S., & Lou, Z. (2019, Aug). The AMPK-Parkin axis negatively regulates necroptosis and tumorigenesis by inhibiting the necrosome. *Nat Cell Biol, 21*(8), 940-951. https://doi.org/10.1038/s41556-019-0356-8

Lewis, D. R., Check, D. P., Caporaso, N. E., Travis, W. D., & Devesa, S. S. (2014, Sep 15). US lung cancer trends by histologic type. *Cancer, 120*(18), 2883-2892. https://doi.org/10.1002/cncr.28749

Li, J., McQuade, T., Siemer, A. B., Napetschnig, J., Moriwaki, K., Hsiao, Y. S., Damko, E., Moquin, D., Walz, T., McDermott, A., Chan, F. K., & Wu, H. (2012, Jul 20). The RIP1/RIP3 necrosome forms a functional amyloid signaling complex required for programmed necrosis. *Cell, 150*(2), 339-350. https://doi.org/10.1016/j.cell.2012.06.019

Li, Y. M., Liu, Z. Y., Wang, J. C., Yu, J. M., Li, Z. C., Yang, H. J., Tang, J., & Chen, Z. N. (2019, Nov). Receptor-Interacting Protein Kinase 3 Deficiency Recruits Myeloid-Derived Suppressor Cells to Hepatocellular Carcinoma Through the Chemokine (C-X-C Motif) Ligand 1-Chemokine (C-X-C Motif) Receptor 2 Axis. *Hepatology, 70*(5), 1564-1581. https://doi.org/10.1002/hep.30676

Liccardi, G., Ramos Garcia, L., Tenev, T., Annibaldi, A., Legrand, A. J., Robertson, D., Feltham, R., Anderton, H., Darding, M., Peltzer, N., Dannappel, M., Schunke, H., Fava, L. L., Haschka, M. D., Glatter, T., Nesvizhskii, A., Schmidt, A., Harris, P. A., Bertin, J., Gough, P. J., Villunger, A., Silke, J., Pasparakis, M., Bianchi, K., & Meier, P. (2019, Feb 7). RIPK1 and Caspase-8 Ensure Chromosome Stability Independently of Their Role in Cell Death and Inflammation. *Mol Cell, 73*(3), 413-428 e417. https://doi.org/10.1016/j.molcel.2018.11.010

Lin, J., Kumari, S., Kim, C., Van, T. M., Wachsmuth, L., Polykratis, A., & Pasparakis, M. (2016, Dec 1). RIPK1 counteracts ZBP1-mediated necroptosis to inhibit inflammation. *Nature, 540*(7631), 124-128. https://doi.org/10.1038/nature20558

Liu, S., Liu, H., Johnston, A., Hanna-Addams, S., Reynoso, E., Xiang, Y., & Wang, Z. (2017, Sep 5). MLKL forms disulfide bond-dependent amyloid-like polymers to induce necroptosis. *Proc Natl Acad Sci U S A, 114*(36), E7450-E7459. https://doi.org/10.1073/pnas.1707531114

Liu, Y., Chen, P., Xu, L., Ouyang, M., Wang, D., Tang, D., Yang, L., Xie, M., Cao, L., & Yang, M. (2019, Apr). Extracellular HMGB1 prevents necroptosis in acute myeloid leukemia cells. *Biomed Pharmacother, 112*, 108714. https://doi.org/10.1016/j.biopha.2019.108714

Liu, Z. Y., Zheng, M., Li, Y. M., Fan, X. Y., Wang, J. C., Li, Z. C., Yang, H. J., Yu, J. M., Cui, J., Jiang, J. L., Tang, J., & Chen, Z. N. (2019). RIP3 promotes colitis-associated colorectal cancer by controlling tumor cell proliferation and CXCL1-induced immune suppression. *Theranostics, 9*(12), 3659-3673. https://doi.org/10.7150/thno.32126

Livak, K. J., & Schmittgen, T. D. (2001, Dec). Analysis of relative gene expression data using real-time quantitative PCR and the 2(-Delta Delta C(T)) Method. *Methods, 25*(4), 402-408. https://doi.org/10.1006/meth.2001.1262

Ma, J., Liu, L., Che, G., Yu, N., Dai, F., & You, Z. (2010, Mar 25). The M1 form of tumor-associated macrophages in non-small cell lung cancer is positively associated with survival time. *BMC Cancer, 10*, 112. https://doi.org/10.1186/1471-2407-10-112

Ma, Y., Adjemian, S., Mattarollo, S. R., Yamazaki, T., Aymeric, L., Yang, H., Portela Catani, J. P., Hannani, D., Duret, H., Steegh, K., Martins, I., Schlemmer, F., Michaud, M., Kepp, O., Sukkurwala, A. Q., Menger, L., Vacchelli, E., Droin, N., Galluzzi, L., Krzysiek, R., Gordon, S., Taylor, P. R., Van Endert, P., Solary, E., Smyth, M. J., Zitvogel, L., & Kroemer, G. (2013, Apr 18). Anticancer chemotherapy-induced intratumoral recruitment and differentiation of antigen-presenting cells. *Immunity, 38*(4), 729-741. https://doi.org/10.1016/j.immuni.2013.03.003

Maemondo, M., Inoue, A., Kobayashi, K., Sugawara, S., Oizumi, S., Isobe, H., Gemma, A., Harada, M., Yoshizawa, H., Kinoshita, I., Fujita, Y., Okinaga, S., Hirano, H., Yoshimori, K., Harada, T., Ogura, T., Ando, M., Miyazawa, H., Tanaka, T., Saijo, Y., Hagiwara, K., Morita, S., Nukiwa, T., & North-East Japan Study, G. (2010, Jun 24). Gefitinib or chemotherapy for non-small-cell lung cancer with mutated EGFR. *N Engl J Med, 362*(25), 2380-2388. https://doi.org/10.1056/NEJMoa0909530

Mainardi, S., Mijimolle, N., Francoz, S., Vicente-Duenas, C., Sanchez-Garcia, I., & Barbacid, M. (2014, Jan 7). Identification of cancer initiating cells in K-Ras driven lung adenocarcinoma. *Proc Natl Acad Sci U S A, 111*(1), 255-260. https://doi.org/10.1073/pnas.1320383110

Marchetti, A., Martella, C., Felicioni, L., Barassi, F., Salvatore, S., Chella, A., Camplese, P. P., Iarussi, T., Mucilli, F., Mezzetti, A., Cuccurullo, F., Sacco, R., & Buttitta, F. (2005, Feb 1). EGFR mutations in non-small-cell lung cancer: analysis of a large series of cases and development of a rapid and sensitive method for diagnostic screening with potential implications on pharmacologic treatment. *J Clin Oncol, 23*(4), 857-865. https://doi.org/10.1200/JCO.2005.08.043

Marino, S., Vooijs, M., van Der Gulden, H., Jonkers, J., & Berns, A. (2000, Apr 15). Induction of medulloblastomas in p53-null mutant mice by somatic inactivation of Rb in the external granular layer cells of the cerebellum. *Genes Dev, 14*(8), 994-1004. https://www.ncbi.nlm.nih.gov/pubmed/10783170

Marjanovic, N. D., Hofree, M., Chan, J. E., Canner, D., Wu, K., Trakala, M., Hartmann, G. G., Smith, O. C., Kim, J. Y., Evans, K. V., Hudson, A., Ashenberg, O., Porter, C. B. M., Bejnood, A., Subramanian, A., Pitter, K., Yan, Y., Delorey, T., Phillips, D. R., Shah, N., Chaudhary, O., Tsankov, A., Hollmann, T., Rekhtman, N., Massion, P. P., Poirier, J. T., Mazutis, L., Li, R., Lee, J. H., Amon, A., Rudin, C. M., Jacks, T., Regev, A., & Tammela, T. (2020, Aug 10). Emergence of a High-Plasticity Cell State during Lung Cancer Evolution. *Cancer Cell, 38*(2), 229-246 e213. https://doi.org/10.1016/j.ccell.2020.06.012

Martins, I., Wang, Y., Michaud, M., Ma, Y., Sukkurwala, A. Q., Shen, S., Kepp, O., Metivier, D., Galluzzi, L., Perfettini, J. L., Zitvogel, L., & Kroemer, G. (2014, Jan). Molecular mechanisms of ATP secretion during immunogenic cell death. *Cell Death Differ, 21*(1), 79-91. https://doi.org/10.1038/cdd.2013.75

Matsushita, H., Vesely, M. D., Koboldt, D. C., Rickert, C. G., Uppaluri, R., Magrini, V. J., Arthur, C. D., White, J. M., Chen, Y. S., Shea, L. K., Hundal, J., Wendl, M. C., Demeter, R., Wylie, T., Allison, J. P., Smyth, M. J., Old, L. J., Mardis, E. R., & Schreiber, R. D. (2012, Feb 8). Cancer exome analysis reveals a T-cell-dependent mechanism of cancer immunoediting. *Nature, 482*(7385), 400-404. https://doi.org/10.1038/nature10755

McClelland, M. R., Carskadon, S. L., Zhao, L., White, E. S., Beer, D. G., Orringer, M. B., Pickens, A., Chang, A. C., & Arenberg, D. A. (2007, Mar). Diversity of the angiogenic phenotype in non-small cell lung cancer. *Am J Respir Cell Mol Biol, 36*(3), 343-350. https://doi.org/10.1165/rcmb.2006-0311OC

McGrail, D. J., Pilie, P. G., Rashid, N. U., Voorwerk, L., Slagter, M., Kok, M., Jonasch, E., Khasraw, M., Heimberger, A. B., Lim, B., Ueno, N. T., Litton, J. K., Ferrarotto, R., Chang, J. T., Moulder, S. L., & Lin, S. Y. (2021, May). High tumor mutation burden fails to predict immune checkpoint blockade response across all cancer types. *Ann Oncol, 32*(5), 661-672. https://doi.org/10.1016/j.annonc.2021.02.006

McGranahan, N., Rosenthal, R., Hiley, C. T., Rowan, A. J., Watkins, T. B. K., Wilson, G. A., Birkbak, N. J., Veeriah, S., Van Loo, P., Herrero, J., Swanton, C., & Consortium, T. R. (2017, Nov 30). Allele-Specific HLA Loss and Immune Escape in Lung Cancer Evolution. *Cell, 171*(6), 1259-1271 e1211. https://doi.org/10.1016/j.cell.2017.10.001

Mestas, J., & Hughes, C. C. (2004, Mar 1). Of mice and not men: differences between mouse and human immunology. *J Immunol, 172*(5), 2731-2738. https://doi.org/10.4049/jimmunol.172.5.2731

Mitsudomi, T., Morita, S., Yatabe, Y., Negoro, S., Okamoto, I., Tsurutani, J., Seto, T., Satouchi, M., Tada, H., Hirashima, T., Asami, K., Katakami, N., Takada, M., Yoshioka, H., Shibata, K., Kudoh, S., Shimizu, E., Saito, H., Toyooka, S., Nakagawa, K., Fukuoka, M., & West Japan Oncology, G. (2010, Feb). Gefitinib versus cisplatin plus docetaxel in patients with non-small-cell lung cancer harbouring mutations of the epidermal growth factor receptor (WJTOG3405): an open label, randomised phase 3 trial. *Lancet Oncol, 11*(2), 121-128. https://doi.org/10.1016/S1470-2045(09)70364-X

Moatti, A., Debesset, A., Pilon, C., Beldi-Ferchiou, A., Leclerc, M., Redjoul, R., Charlotte, F., To, N. H., Bak, A., Belkacemi, Y., Salomon, B. L., Issa, F., Michonneau, D., Maury, S., Cohen, J. L., & Thiolat, A. (2022, Apr). TNFR2 blockade of regulatory T cells unleashes an antitumor immune response after hematopoietic stem-cell transplantation. *J Immunother Cancer, 10*(4). https://doi.org/10.1136/jitc-2021-003508

Mok, T. S., Wu, Y. L., Thongprasert, S., Yang, C. H., Chu, D. T., Saijo, N., Sunpaweravong, P., Han, B., Margono, B., Ichinose, Y., Nishiwaki, Y., Ohe, Y., Yang, J. J., Chewaskulyong, B., Jiang, H., Duffield, E. L., Watkins, C. L., Armour, A. A., & Fukuoka, M. (2009, Sep 3). Gefitinib or carboplatin-paclitaxel in pulmonary adenocarcinoma. *N Engl J Med, 361*(10), 947-957. https://doi.org/10.1056/NEJMoa0810699

Moriwaki, K., Balaji, S., Bertin, J., Gough, P. J., & Chan, F. K. (2017, Mar 7). Distinct Kinase-Independent Role of RIPK3 in CD11c(+) Mononuclear Phagocytes in Cytokine-Induced Tissue Repair. *Cell Rep, 18*(10), 2441-2451. https://doi.org/10.1016/j.celrep.2017.02.015

Moriwaki, K., Balaji, S., McQuade, T., Malhotra, N., Kang, J., & Chan, F. K. (2014, Oct 16). The necroptosis adaptor RIPK3 promotes injury-induced cytokine expression and tissue repair. *Immunity, 41*(4), 567-578. https://doi.org/10.1016/j.immuni.2014.09.016

Moriwaki, K., Bertin, J., Gough, P. J., & Chan, F. K. (2015, Feb 15). A RIPK3-caspase 8 complex mediates atypical pro-IL-1beta processing. *J Immunol, 194*(4), 1938-1944. https://doi.org/10.4049/jimmunol.1402167

Moriwaki, K., Bertin, J., Gough, P. J., Orlowski, G. M., & Chan, F. K. (2015, Feb 12). Differential roles of RIPK1 and RIPK3 in TNF-induced necroptosis and chemotherapeutic agent-induced cell death. *Cell Death Dis, 6*, e1636. https://doi.org/10.1038/cddis.2015.16

Mouse Genome Sequencing, C., Waterston, R. H., Lindblad-Toh, K., Birney, E., Rogers, J., Abril, J. F., Agarwal, P., Agarwala, R., Ainscough, R., Alexandersson, M., An, P., Antonarakis, S. E., Attwood, J., Baertsch, R., Bailey, J., Barlow, K., Beck, S., Berry, E., Birren, B., Bloom, T., Bork, P., Botcherby, M., Bray, N., Brent, M. R., Brown, D. G., Brown, S. D., Bult, C., Burton, J., Butler, J., Campbell, R. D., Carninci, P., Cawley, S., Chiaromonte, F., Chinwalla, A. T., Church, D. M., Clamp, M., Clee, C., Collins, F. S., Cook, L. L., Copley, R. R., Coulson, A., Couronne, O., Cuff, J., Curwen, V., Cutts, T., Daly, M., David, R., Davies, J., Delehaunty, K. D., Deri, J., Dermitzakis, E. T., Dewey, C., Dickens, N. J., Diekhans, M., Dodge, S., Dubchak, I., Dunn, D. M., Eddy, S. R.,

Elnitski, L., Emes, R. D., Eswara, P., Eyras, E., Felsenfeld, A., Fewell, G. A., Flicek, P., Foley, K., Frankel, W. N., Fulton, L. A., Fulton, R. S., Furey, T. S., Gage, D., Gibbs, R. A., Glusman, G., Gnerre, S., Goldman, N., Goodstadt, L., Grafham, D., Graves, T. A., Green, E. D., Gregory, S., Guigo, R., Guyer, M., Hardison, R. C., Haussler, D., Hayashizaki, Y., Hillier, L. W., Hinrichs, A., Hlavina, W., Holzer, T., Hsu, F., Hua, A., Hubbard, T., Hunt, A., Jackson, I., Jaffe, D. B., Johnson, L. S., Jones, M., Jones, T. A., Joy, A., Kamal, M., Karlsson, E. K., Karolchik, D., Kasprzyk, A., Kawai, J., Keibler, E., Kells, C., Kent, W. J., Kirby, A., Kolbe, D. L., Korf, I., Kucherlapati, R. S., Kulbokas, E. J., Kulp, D., Landers, T., Leger, J. P., Leonard, S., Letunic, I., Levine, R., Li, J., Li, M., Lloyd, C., Lucas, S., Ma, B., Maglott, D. R., Mardis, E. R., Matthews, L., Mauceli, E., Mayer, J. H., McCarthy, M., McCombie, W. R., McLaren, S., McLay, K., McPherson, J. D., Meldrim, J., Meredith, B., Mesirov, J. P., Miller, W., Miner, T. L., Mongin, E., Montgomery, K. T., Morgan, M., Mott, R., Mullikin, J. C., Muzny, D. M., Nash, W. E., Nelson, J. O., Nhan, M. N., Nicol, R., Ning, Z., Nusbaum, C., O'Connor, M. J., Okazaki, Y., Oliver, K., Overton-Larty, E., Pachter, L., Parra, G., Pepin, K. H., Peterson, J., Pevzner, P., Plumb, R., Pohl, C. S., Poliakov, A., Ponce, T. C., Ponting, C. P., Potter, S., Quail, M., Reymond, A., Roe, B. A., Roskin, K. M., Rubin, E. M., Rust, A. G., Santos, R., Sapojnikov, V., Schultz, B., Schultz, J., Schwartz, M. S., Schwartz, S., Scott, C., Seaman, S., Searle, S., Sharpe, T., Sheridan, A., Shownkeen, R., Sims, S., Singer, J. B., Slater, G., Smit, A., Smith, D. R., Spencer, B., Stabenau, A., Stange-Thomann, N., Sugnet, C., Suyama, M., Tesler, G., Thompson, J., Torrents, D., Trevaskis, E., Tromp, J., Ucla, C., Ureta-Vidal, A., Vinson, J. P., Von Niederhausern, A. C., Wade, C. M., Wall, M., Weber, R. J., Weiss, R. B., Wendl, M. C., West, A. P., Wetterstrand, K., Wheeler, R., Whelan, S., Wierzbowski, J., Willey, D., Williams, S., Wilson, R. K., Winter, E., Worley, K. C., Wyman, D., Yang, S., Yang, S. P., Zdobnov, E. M., Zody, M. C., & Lander, E. S. (2002, Dec 5). Initial sequencing and comparative analysis of the mouse genome. *Nature, 420*(6915), 520-562. https://doi.org/10.1038/nature01262

Muendlein, H. I., Sarhan, J., Liu, B. C., Connolly, W. M., Schworer, S. A., Smirnova, I., Tang, A. Y., Ilyukha, V., Pietruska, J., Tahmasebi, S., Sonenberg, N., Degterev, A., & Poltorak, A. (2020, Jan 21). Constitutive Interferon Attenuates RIPK1/3-Mediated Cytokine Translation. *Cell Rep, 30*(3), 699-713 e694. https://doi.org/10.1016/j.celrep.2019.12.073

Mukhopadhyay, S., & Katzenstein, A. L. (2011, Jan). Subclassification of non-small cell lung carcinomas lacking morphologic differentiation on biopsy specimens: Utility of an immunohistochemical panel containing TTF-1, napsin A, p63, and CK5/6. *Am J Surg Pathol, 35*(1), 15-25. https://doi.org/10.1097/PAS.0b013e3182036d05

Munkhbaatar, E., Dietzen, M., Agrawal, D., Anton, M., Jesinghaus, M., Boxberg, M., Pfarr, N., Bidola, P., Uhrig, S., Hockendorf, U., Meinhardt, A. L., Wahida, A., Heid, I., Braren, R., Mishra, R., Warth, A., Muley, T., Poh, P. S. P., Wang, X., Frohling, S., Steiger, K., Slotta-Huspenina, J., van Griensven, M., Pfeiffer, F., Lange, S., Rad, R., Spella, M., Stathopoulos, G. T., Ruland, J., Bassermann, F., Weichert, W., Strasser, A., Branca, C., Heikenwalder, M., Swanton, C., McGranahan, N., & Jost, P. J. (2020, Sep 10). MCL-1 gains occur with high frequency in lung adenocarcinoma and can be targeted therapeutically. *Nat Commun, 11*(1), 4527. https://doi.org/10.1038/s41467-020-18372-1

Murphy, J. M., Czabotar, P. E., Hildebrand, J. M., Lucet, I. S., Zhang, J. G., Alvarez-Diaz, S., Lewis, R., Lalaoui, N., Metcalf, D., Webb, A. I., Young, S. N., Varghese, L. N., Tannahill, G. M., Hatchell, E. C., Majewski, I. J., Okamoto, T., Dobson, R. C., Hilton, D. J., Babon, J. J., Nicola, N. A., Strasser, A., Silke, J., & Alexander, W. S. (2013, Sep 19). The pseudokinase MLKL mediates necroptosis via a molecular switch mechanism. *Immunity, 39*(3), 443-453. https://doi.org/10.1016/j.immuni.2013.06.018

Najjar, M., Saleh, D., Zelic, M., Nogusa, S., Shah, S., Tai, A., Finger, J. N., Polykratis, A., Gough, P. J., Bertin, J., Whalen, M., Pasparakis, M., Balachandran, S., Kelliher, M., Poltorak, A., & Degterev, A. (2016, Jul 19). RIPK1 and RIPK3 Kinases Promote Cell-Death-Independent Inflammation by Toll-like Receptor 4. *Immunity, 45*(1), 46-59. https://doi.org/10.1016/j.immuni.2016.06.007

Navab, R., Strumpf, D., To, C., Pasko, E., Kim, K. S., Park, C. J., Hai, J., Liu, J., Jonkman, J., Barczyk, M., Bandarchi, B., Wang, Y. H., Venkat, K., Ibrahimov, E., Pham, N. A., Ng, C., Radulovich, N., Zhu, C. Q., Pintilie, M., Wang, D., Lu, A., Jurisica, I., Walker, G. C., Gullberg, D., & Tsao, M. S. (2016, Apr 14). Integrin alpha11beta1 regulates cancer stromal stiffness and promotes tumorigenicity and metastasis in non-small cell lung cancer. *Oncogene, 35*(15), 1899-1908. https://doi.org/10.1038/onc.2015.254

Newton, K., Wickliffe, K. E., Maltzman, A., Dugger, D. L., Strasser, A., Pham, V. C., Lill, J. R., Roose-Girma, M., Warming, S., Solon, M., Ngu, H., Webster, J. D., & Dixit, V. M. (2016, Dec 1). RIPK1 inhibits ZBP1-driven necroptosis during development. *Nature, 540*(7631), 129-133. https://doi.org/10.1038/nature20559

Nikitin, A. Y., Alcaraz, A., Anver, M. R., Bronson, R. T., Cardiff, R. D., Dixon, D., Fraire, A. E., Gabrielson, E. W., Gunning, W. T., Haines, D. C., Kaufman, M. H., Linnoila, R. I., Maronpot, R. R., Rabson, A. S., Reddick, R. L., Rehm, S., Rozengurt, N., Schuller, H. M., Shmidt, E. N., Travis, W. D., Ward, J. M., & Jacks, T. (2004, Apr 1). Classification of proliferative pulmonary lesions of the mouse: recommendations of the mouse models of human cancers consortium. *Cancer Res, 64*(7), 2307-2316. https://doi.org/10.1158/0008-5472.can-03-3376

Ohri, C. M., Shikotra, A., Green, R. H., Waller, D. A., & Bradding, P. (2009, Jan). Macrophages within NSCLC tumour islets are predominantly of a cytotoxic M1 phenotype associated with extended survival. *Eur Respir J, 33*(1), 118-126. https://doi.org/10.1183/09031936.00065708

Orozco, S. L., Daniels, B. P., Yatim, N., Messmer, M. N., Quarato, G., Chen-Harris, H., Cullen, S. P., Snyder, A. G., Ralli-Jain, P., Frase, S., Tait, S. W. G., Green, D. R., Albert, M. L., & Oberst, A. (2019, Aug 27). RIPK3 Activation Leads to Cytokine Synthesis that Continues after Loss of Cell Membrane Integrity. *Cell Rep, 28*(9), 2275-2287 e2275. https://doi.org/10.1016/j.celrep.2019.07.077

Park, H. H., Kim, H. R., Park, S. Y., Hwang, S. M., Hong, S. M., Park, S., Kang, H. C., Morgan, M. J., Cha, J. H., Lee, D., Roe, J. S., & Kim, Y. S. (2021, Aug 21). RIPK3 activation induces TRIM28 derepression in cancer cells and enhances the anti-tumor microenvironment. *Mol Cancer, 20*(1), 107. https://doi.org/10.1186/s12943-021-01399-3

Park, J. E., Lee, J. H., Lee, S. Y., Hong, M. J., Choi, J. E., Park, S., Jeong, J. Y., Lee, E. B., Choi, S. H., Lee, Y. H., Seo, H. W., Yoo, S. S., Lee, J., Cha, S. I., Kim, C. H., & Park, J. Y. (2020). Expression of key regulatory genes in necroptosis and its effect on the prognosis in non-small cell lung cancer. *J Cancer, 11*(18), 5503-5510. https://doi.org/10.7150/jca.46172

Park, J. H., Jung, K. H., Kim, S. J., Yoon, Y. C., Yan, H. H., Fang, Z., Lee, J. E., Lim, J. H., Mah, S., Hong, S., Kim, Y. S., & Hong, S. S. (2019, Mar 1). HS-173 as a novel inducer of RIP3-dependent necroptosis in lung cancer. *Cancer Lett, 444*, 94-104. https://doi.org/10.1016/j.canlet.2018.12.006

Platt, R. J., Chen, S., Zhou, Y., Yim, M. J., Swiech, L., Kempton, H. R., Dahlman, J. E., Parnas, O., Eisenhaure, T. M., Jovanovic, M., Graham, D. B., Jhunjhunwala, S., Heidenreich, M., Xavier, R. J., Langer, R., Anderson, D. G., Hacohen, N., Regev, A., Feng, G., Sharp, P. A., & Zhang, F. (2014, Oct 9). CRISPR-Cas9 knockin mice for genome editing and cancer modeling. *Cell, 159*(2), 440-455. https://doi.org/10.1016/j.cell.2014.09.014

Postmus, P. E., Kerr, K. M., Oudkerk, M., Senan, S., Waller, D. A., Vansteenkiste, J., Escriu, C., Peters, S., & Committee, E. G. (2017, Jul 1). Early and locally advanced non-small-cell lung cancer (NSCLC): ESMO Clinical Practice Guidelines for diagnosis, treatment and follow-up. *Ann Oncol, 28*(suppl_4), iv1-iv21. https://doi.org/10.1093/annonc/mdx222

Quarato, G., Guy, C. S., Grace, C. R., Llambi, F., Nourse, A., Rodriguez, D. A., Wakefield, R., Frase, S., Moldoveanu, T., & Green, D. R. (2016, Feb 18). Sequential Engagement of Distinct MLKL Phosphatidylinositol-Binding Sites Executes Necroptosis. *Mol Cell, 61*(4), 589-601. https://doi.org/10.1016/j.molcel.2016.01.011

Rahib, L., Smith, B. D., Aizenberg, R., Rosenzweig, A. B., Fleshman, J. M., & Matrisian, L. M. (2014, Jun 1). Projecting cancer incidence and deaths to 2030: the unexpected burden of thyroid, liver, and pancreas cancers in the United States. *Cancer Res, 74*(11), 2913-2921. https://doi.org/10.1158/0008-5472.CAN-14-0155

Reck, M., Rodriguez-Abreu, D., Robinson, A. G., Hui, R., Csoszi, T., Fulop, A., Gottfried, M., Peled, N., Tafreshi, A., Cuffe, S., O'Brien, M., Rao, S., Hotta, K., Leal, T. A., Riess, J. W., Jensen, E., Zhao, B., Pietanza, M. C., & Brahmer, J. R. (2021, Jul 20). Five-Year Outcomes With Pembrolizumab Versus Chemotherapy for Metastatic Non-Small-Cell Lung Cancer With PD-L1 Tumor Proportion Score >/= 50. *J Clin Oncol, 39*(21), 2339-2349. https://doi.org/10.1200/JCO.21.00174

Reck, M., Rodriguez-Abreu, D., Robinson, A. G., Hui, R., Csoszi, T., Fulop, A., Gottfried, M., Peled, N., Tafreshi, A., Cuffe, S., O'Brien, M., Rao, S., Hotta, K., Vandormael, K., Riccio, A., Yang, J., Pietanza, M. C., & Brahmer, J. R. (2019, Mar 1). Updated Analysis of KEYNOTE-024: Pembrolizumab Versus Platinum-Based Chemotherapy for Advanced Non-Small-Cell Lung Cancer With PD-L1 Tumor Proportion Score of 50% or Greater. *J Clin Oncol, 37*(7), 537-546. https://doi.org/10.1200/JCO.18.00149

Red Brewer, M., Yun, C. H., Lai, D., Lemmon, M. A., Eck, M. J., & Pao, W. (2013, Sep 17). Mechanism for activation of mutated epidermal growth factor receptors in lung cancer. *Proc Natl Acad Sci U S A, 110*(38), E3595-3604. https://doi.org/10.1073/pnas.1220050110

Rekhtman, N., Ang, D. C., Sima, C. S., Travis, W. D., & Moreira, A. L. (2011, Oct). Immunohistochemical algorithm for differentiation of lung adenocarcinoma and squamous cell carcinoma based on large series of whole-tissue sections with validation in small specimens. *Mod Pathol, 24*(10), 1348-1359. https://doi.org/10.1038/modpathol.2011.92

Rosell, R., Carcereny, E., Gervais, R., Vergnenegre, A., Massuti, B., Felip, E., Palmero, R., Garcia-Gomez, R., Pallares, C., Sanchez, J. M., Porta, R., Cobo, M., Garrido, P., Longo, F., Moran, T., Insa, A., De Marinis, F., Corre, R., Bover, I., Illiano, A., Dansin, E., de Castro, J., Milella, M., Reguart, N., Altavilla, G., Jimenez, U., Provencio, M., Moreno, M. A., Terrasa, J., Munoz-Langa, J., Valdivia, J., Isla, D., Domine, M., Molinier, O., Mazieres, J., Baize, N., Garcia-Campelo, R., Robinet, G., Rodriguez-Abreu, D., Lopez-Vivanco, G., Gebbia, V., Ferrera-Delgado, L., Bombaron, P., Bernabe, R., Bearz, A., Artal, A., Cortesi, E., Rolfo, C., Sanchez-Ronco, M., Drozdowskyj, A., Queralt, C., de Aguirre, I., Ramirez, J. L., Sanchez, J. J., Molina, M. A., Taron, M., Paz-Ares, L., Spanish Lung Cancer Group in collaboration with Groupe Francais de, P.-C., & Associazione Italiana Oncologia, T. (2012, Mar). Erlotinib versus standard chemotherapy as first-line treatment for European patients with advanced EGFR mutation-positive non-small-cell lung cancer (EURTAC): a multicentre, open-label, randomised phase 3 trial. *Lancet Oncol, 13*(3), 239-246. https://doi.org/10.1016/S1470-2045(11)70393-X

Rosenthal, R., Cadieux, E. L., Salgado, R., Bakir, M. A., Moore, D. A., Hiley, C. T., Lund, T., Tanic, M., Reading, J. L., Joshi, K., Henry, J. Y., Ghorani, E., Wilson, G. A., Birkbak, N. J., Jamal-Hanjani, M., Veeriah, S., Szallasi, Z., Loi, S., Hellmann, M. D., Feber, A., Chain, B., Herrero, J., Quezada, S. A., Demeulemeester, J., Van Loo, P., Beck, S., McGranahan, N., Swanton, C., & consortium, T. R. (2019, Mar). Neoantigen-directed immune escape in lung cancer evolution. *Nature, 567*(7749), 479-485. https://doi.org/10.1038/s41586-019-1032-7

Scheffzek, K., Ahmadian, M. R., Kabsch, W., Wiesmuller, L., Lautwein, A., Schmitz, F., & Wittinghofer, A. (1997, Jul 18). The Ras-RasGAP complex: structural basis for GTPase activation and its loss in oncogenic Ras mutants. *Science, 277*(5324), 333-338. https://doi.org/10.1126/science.277.5324.333

Seifert, L., Werba, G., Tiwari, S., Giao Ly, N. N., Alothman, S., Alqunaibit, D., Avanzi, A., Barilla, R., Daley, D., Greco, S. H., Torres-Hernandez, A., Pergamo, M., Ochi, A., Zambirinis, C. P., Pansari, M., Rendon, M., Tippens, D., Hundeyin, M., Mani, V. R., Hajdu, C., Engle, D., & Miller, G. (2016, Apr 14). The necrosome promotes pancreatic oncogenesis via CXCL1 and Mincle-induced immune suppression. *Nature, 532*(7598), 245-249. https://doi.org/10.1038/nature17403

Sequist, L. V., Yang, J. C., Yamamoto, N., O'Byrne, K., Hirsh, V., Mok, T., Geater, S. L., Orlov, S., Tsai, C. M., Boyer, M., Su, W. C., Bennouna, J., Kato, T., Gorbunova, V., Lee, K. H., Shah, R., Massey, D., Zazulina, V., Shahidi, M., & Schuler, M. (2013, Sep 20). Phase III study of afatinib or cisplatin plus pemetrexed in patients with metastatic lung adenocarcinoma with EGFR mutations. *J Clin Oncol, 31*(27), 3327-3334. https://doi.org/10.1200/JCO.2012.44.2806

Siegel, R. L., Miller, K. D., & Jemal, A. (2020, Jan). Cancer statistics, 2020. *CA Cancer J Clin, 70*(1), 7-30. https://doi.org/10.3322/caac.21590

Snyder, A. G., Hubbard, N. W., Messmer, M. N., Kofman, S. B., Hagan, C. E., Orozco, S. L., Chiang, K., Daniels, B. P., Baker, D., & Oberst, A. (2019, Jun 21). Intratumoral activation of the necroptotic pathway components RIPK1 and RIPK3 potentiates antitumor immunity. *Sci Immunol, 4*(36). https://doi.org/10.1126/sciimmunol.aaw2004

Soria, J. C., Ohe, Y., Vansteenkiste, J., Reungwetwattana, T., Chewaskulyong, B., Lee, K. H., Dechaphunkul, A., Imamura, F., Nogami, N., Kurata, T., Okamoto, I., Zhou, C., Cho, B. C., Cheng, Y., Cho, E. K., Voon, P. J., Planchard, D., Su, W. C., Gray, J. E., Lee, S. M., Hodge, R., Marotti, M., Rukazenkov, Y., Ramalingam, S. S., & Investigators, F. (2018, Jan 11). Osimertinib in Untreated EGFR-Mutated Advanced Non-Small-Cell Lung Cancer. *N Engl J Med, 378*(2), 113-125. https://doi.org/10.1056/NEJMoa1713137

Spisek, R., Charalambous, A., Mazumder, A., Vesole, D. H., Jagannath, S., & Dhodapkar, M. V. (2007, Jun 1). Bortezomib enhances dendritic cell (DC)-mediated induction of immunity to human myeloma via exposure of cell surface heat shock protein 90 on dying tumor cells: therapeutic implications. *Blood, 109*(11), 4839-4845. https://doi.org/10.1182/blood-2006-10-054221

Stoll, G., Ma, Y., Yang, H., Kepp, O., Zitvogel, L., & Kroemer, G. (2017). Pro-necrotic molecules impact local immunosurveillance in human breast cancer. *Oncoimmunology, 6*(4), e1299302. https://doi.org/10.1080/2162402X.2017.1299302

Sun, L., Wang, H., Wang, Z., He, S., Chen, S., Liao, D., Wang, L., Yan, J., Liu, W., Lei, X., & Wang, X. (2012, Jan 20). Mixed lineage kinase domain-like protein mediates necrosis signaling downstream of RIP3 kinase. *Cell, 148*(1-2), 213-227. https://doi.org/10.1016/j.cell.2011.11.031

Szabo, P. A., Levitin, H. M., Miron, M., Snyder, M. E., Senda, T., Yuan, J., Cheng, Y. L., Bush, E. C., Dogra, P., Thapa, P., Farber, D. L., & Sims, P. A. (2019, Oct 17). Single-cell transcriptomics of human T cells reveals tissue and activation signatures in health and disease. *Nat Commun, 10*(1), 4706. https://doi.org/10.1038/s41467-019-12464-3

Tacha, D., Yu, C., Bremer, R., Qi, W., & Haas, T. (2012, May). A 6-antibody panel for the classification of lung adenocarcinoma versus squamous cell carcinoma. *Appl Immunohistochem Mol Morphol, 20*(3), 201-207. https://doi.org/10.1097/PAI.0b013e31823d7f0e

The, L. (2018, Sep 22). GLOBOCAN 2018: counting the toll of cancer. *Lancet, 392*(10152), 985. https://doi.org/10.1016/S0140-6736(18)32252-9

Travis, W. D., Brambilla, E., Burke, A. P., Marx, A., & Nicholson, A. G. (2015, Sep). Introduction to The 2015 World Health Organization Classification of Tumors of the Lung, Pleura, Thymus, and Heart. *J Thorac Oncol, 10*(9), 1240-1242. https://doi.org/10.1097/JTO.0000000000000663

Travis, W. D., Brambilla, E., Nicholson, A. G., Yatabe, Y., Austin, J. H. M., Beasley, M. B., Chirieac, L. R., Dacic, S., Duhig, E., Flieder, D. B., Geisinger, K., Hirsch, F. R., Ishikawa, Y., Kerr, K. M., Noguchi, M., Pelosi, G., Powell, C. A., Tsao, M. S., Wistuba, I., & Panel, W. H. O. (2015, Sep). The 2015 World Health Organization Classification of Lung Tumors: Impact of Genetic, Clinical and Radiologic Advances Since the 2004 Classification. *J Thorac Oncol, 10*(9), 1243-1260. https://doi.org/10.1097/JTO.0000000000000630

Upton, J. W., Kaiser, W. J., & Mocarski, E. S. (2010, Apr 22). Virus inhibition of RIP3-dependent necrosis. *Cell Host Microbe, 7*(4), 302-313. https://doi.org/10.1016/j.chom.2010.03.006

van Die, I. M., Bergmans, H. E., & Hoekstra, W. P. (1983, Mar). Transformation in Escherichia coli: studies on the role of the heat shock in induction of competence. *J Gen Microbiol, 129*(3), 663-670. https://doi.org/10.1099/00221287-129-3-663

Vansteenkiste, J., Zielinski, M., Linder, A., Dahabreh, J., Gonzalez, E. E., Malinowski, W., Lopez-Brea, M., Vanakesa, T., Jassem, J., Kalofonos, H., Perdeus, J., Bonnet, R., Basko, J., Janilionis, R., Passlick, B., Treasure, T., Gillet, M., Lehmann, F. F., & Brichard, V. G. (2013, Jul 1). Adjuvant MAGE-A3 immunotherapy in resected non-small-cell lung cancer: phase II randomized study results. *J Clin Oncol, 31*(19), 2396-2403. https://doi.org/10.1200/JCO.2012.43.7103

Vansteenkiste, J. F., Cho, B. C., Vanakesa, T., De Pas, T., Zielinski, M., Kim, M. S., Jassem, J., Yoshimura, M., Dahabreh, J., Nakayama, H., Havel, L., Kondo, H., Mitsudomi, T., Zarogoulidis, K., Gladkov, O. A., Udud, K., Tada, H., Hoffman, H., Bugge, A., Taylor, P., Gonzalez, E. E., Liao, M. L., He, J., Pujol, J. L., Louahed, J., Debois, M., Brichard, V., Debruyne, C., Therasse, P., & Altorki, N. (2016, Jun). Efficacy of the MAGE-A3 cancer immunotherapeutic as adjuvant therapy in patients with resected MAGE-A3-positive non-small-cell lung cancer (MAGRIT): a randomised, double-

blind, placebo-controlled, phase 3 trial. *Lancet Oncol, 17*(6), 822-835. https://doi.org/10.1016/S1470-2045(16)00099-1

Vatansever, S., Erman, B., & Gumus, Z. H. (2020). Comparative effects of oncogenic mutations G12C, G12V, G13D, and Q61H on local conformations and dynamics of K-Ras. *Comput Struct Biotechnol J, 18*, 1000-1011. https://doi.org/10.1016/j.csbj.2020.04.003

Vogelstein, B., & Gillespie, D. (1979, Feb). Preparative and analytical purification of DNA from agarose. *Proc Natl Acad Sci U S A, 76*(2), 615-619. https://doi.org/10.1073/pnas.76.2.615

Wang, D., Pham, N. A., Freeman, T. M., Raghavan, V., Navab, R., Chang, J., Zhu, C. Q., Ly, D., Tong, J., Wouters, B. G., Pintilie, M., Moran, M. F., Liu, G., Shepherd, F. A., & Tsao, M. S. (2019, Jul 19). Somatic Alteration Burden Involving Non-Cancer Genes Predicts Prognosis in Early-Stage Non-Small Cell Lung Cancer. *Cancers (Basel), 11*(7). https://doi.org/10.3390/cancers11071009

Wang, H., Sun, L., Su, L., Rizo, J., Liu, L., Wang, L. F., Wang, F. S., & Wang, X. (2014, Apr 10). Mixed lineage kinase domain-like protein MLKL causes necrotic membrane disruption upon phosphorylation by RIP3. *Mol Cell, 54*(1), 133-146. https://doi.org/10.1016/j.molcel.2014.03.003

Wang, K. J., Wang, K. Y., Zhang, H. Z., Meng, X. Y., Chen, J. F., Wang, P., Jiang, J. H., & Ma, Q. (2020). Up-Regulation of RIP3 Alleviates Prostate Cancer Progression by Activation of RIP3/MLKL Signaling Pathway and Induction of Necroptosis. *Front Oncol, 10*, 1720. https://doi.org/10.3389/fonc.2020.01720

Wang, L., Chang, X., Feng, J., Yu, J., & Chen, G. (2019). TRADD Mediates RIPK1-Independent Necroptosis Induced by Tumor Necrosis Factor. *Front Cell Dev Biol, 7*, 393. https://doi.org/10.3389/fcell.2019.00393

Wang, Q., Chen, W., Xu, X., Li, B., He, W., Padilla, M. T., Jang, J. H., Nyunoya, T., Amin, S., Wang, X., & Lin, Y. (2013, Sep). RIP1 potentiates BPDE-induced transformation in human bronchial epithelial cells through catalase-mediated suppression of excessive reactive oxygen species. *Carcinogenesis, 34*(9), 2119-2128. https://doi.org/10.1093/carcin/bgt143

Wang, Q., Wang, P., Zhang, L., Tessema, M., Bai, L., Xu, X., Li, Q., Zheng, X., Saxton, B., Chen, W., Willink, R., Li, Z., Zhang, L., Belinsky, S. A., Wang, X., Zhou, B., & Lin, Y. (2020, Feb). Epigenetic Regulation of RIP3 Suppresses Necroptosis and Increases Resistance to Chemotherapy in NonSmall Cell Lung Cancer. *Transl Oncol, 13*(2), 372-382. https://doi.org/10.1016/j.tranon.2019.11.011

Wang, X. W., Yeh, H., Schaeffer, L., Roy, R., Moncollin, V., Egly, J. M., Wang, Z., Freidberg, E. C., Evans, M. K., Taffe, B. G., & et al. (1995, Jun). p53 modulation of TFIIH-associated nucleotide excision repair activity. *Nat Genet, 10*(2), 188-195. https://doi.org/10.1038/ng0695-188

Wang, Z., Longo, P. A., Tarrant, M. K., Kim, K., Head, S., Leahy, D. J., & Cole, P. A. (2011, Nov 20). Mechanistic insights into the activation of oncogenic forms of EGF receptor. *Nat Struct Mol Biol, 18*(12), 1388-1393. https://doi.org/10.1038/nsmb.2168

Wei, R., Xu, L. W., Liu, J., Li, Y., Zhang, P., Shan, B., Lu, X., Qian, L., Wu, Z., Dong, K., Zhu, H., Pan, L., Yuan, J., & Pan, H. (2017, Jun 1). SPATA2 regulates the activation of RIPK1 by modulating linear ubiquitination. *Genes Dev, 31*(11), 1162-1176. https://doi.org/10.1101/gad.299776.117

Welsh, T. J., Green, R. H., Richardson, D., Waller, D. A., O'Byrne, K. J., & Bradding, P. (2005, Dec 10). Macrophage and mast-cell invasion of tumor cell islets confers a marked survival advantage in non-small-cell lung cancer. *J Clin Oncol, 23*(35), 8959-8967. https://doi.org/10.1200/JCO.2005.01.4910

Westcott, P. M., Halliwill, K. D., To, M. D., Rashid, M., Rust, A. G., Keane, T. M., Delrosario, R., Jen, K. Y., Gurley, K. E., Kemp, C. J., Fredlund, E., Quigley, D. A., Adams, D. J., & Balmain, A. (2015, Jan 22). The mutational landscapes of genetic and chemical models of Kras-driven lung cancer. *Nature, 517*(7535), 489-492. https://doi.org/10.1038/nature13898

Wu, L., Zhang, X., Zheng, L., Zhao, H., Yan, G., Zhang, Q., Zhou, Y., Lei, J., Zhang, J., Wang, J., Xin, R., Jiang, L., Peng, J., Chen, Q., Lam, S. M., Shui, G., Miao, H., & Li, Y. (2020, May). RIPK3

Orchestrates Fatty Acid Metabolism in Tumor-Associated Macrophages and Hepatocarcinogenesis. *Cancer Immunol Res, 8*(5), 710-721. https://doi.org/10.1158/2326-6066.CIR-19-0261

Wu, P., Zhu, X., Jin, W., Hao, S., Liu, Q., & Zhang, L. (2015, May 1). Oxaliplatin triggers necrosis as well as apoptosis in gastric cancer SGC-7901 cells. *Biochem Biophys Res Commun, 460*(2), 183-190. https://doi.org/10.1016/j.bbrc.2015.03.003

Wu, X., Tian, L., Li, J., Zhang, Y., Han, V., Li, Y., Xu, X., Li, H., Chen, X., Chen, J., Jin, W., Xie, Y., Han, J., & Zhong, C. Q. (2012, Dec). Investigation of receptor interacting protein (RIP3)-dependent protein phosphorylation by quantitative phosphoproteomics. *Mol Cell Proteomics, 11*(12), 1640-1651. https://doi.org/10.1074/mcp.M112.019091

Xiao, H., Guo, Y., Li, B., Li, X., Wang, Y., Han, S., Cheng, D., & Shuai, X. (2020, Jul 22). M2-Like Tumor-Associated Macrophage-Targeted Codelivery of STAT6 Inhibitor and IKKbeta siRNA Induces M2-to-M1 Repolarization for Cancer Immunotherapy with Low Immune Side Effects. *ACS Cent Sci, 6*(7), 1208-1222. https://doi.org/10.1021/acscentsci.9b01235

Xie, M., Liu, M., & He, C. S. (2012). SIRT1 regulates endothelial Notch signaling in lung cancer. *PLoS One, 7*(9), e45331. https://doi.org/10.1371/journal.pone.0045331

Xie, Y., Zhao, Y., Shi, L., Li, W., Chen, K., Li, M., Chen, X., Zhang, H., Li, T., Matsuzawa-Ishimoto, Y., Yao, X., Shao, D., Ke, Z., Li, J., Chen, Y., Zhang, X., Cui, J., Cui, S., Leng, Q., Cadwell, K., Li, X., Wei, H., Zhang, H., Li, H., & Xiao, H. (2020, Apr 1). Gut epithelial TSC1/mTOR controls RIPK3-dependent necroptosis in intestinal inflammation and cancer. *J Clin Invest, 130*(4), 2111-2128. https://doi.org/10.1172/JCI133264

Xu, X., Rock, J. R., Lu, Y., Futtner, C., Schwab, B., Guinney, J., Hogan, B. L., & Onaitis, M. W. (2012, Mar 27). Evidence for type II cells as cells of origin of K-Ras-induced distal lung adenocarcinoma. *Proc Natl Acad Sci U S A, 109*(13), 4910-4915. https://doi.org/10.1073/pnas.1112499109

Xu, Y., Ma, H. B., Fang, Y. L., Zhang, Z. R., Shao, J., Hong, M., Huang, C. J., Liu, J., & Chen, R. Q. (2017, Feb). Cisplatin-induced necroptosis in TNFalpha dependent and independent pathways. *Cell Signal, 31*, 112-123. https://doi.org/10.1016/j.cellsig.2017.01.004

Yadav, M., Jhunjhunwala, S., Phung, Q. T., Lupardus, P., Tanguay, J., Bumbaca, S., Franci, C., Cheung, T. K., Fritsche, J., Weinschenk, T., Modrusan, Z., Mellman, I., Lill, J. R., & Delamarre, L. (2014, Nov 27). Predicting immunogenic tumour mutations by combining mass spectrometry and exome sequencing. *Nature, 515*(7528), 572-576. https://doi.org/10.1038/nature14001

Yamazaki, T., Hannani, D., Poirier-Colame, V., Ladoire, S., Locher, C., Sistigu, A., Prada, N., Adjemian, S., Catani, J. P., Freudenberg, M., Galanos, C., Andre, F., Kroemer, G., & Zitvogel, L. (2014, Jan). Defective immunogenic cell death of HMGB1-deficient tumors: compensatory therapy with TLR4 agonists. *Cell Death Differ, 21*(1), 69-78. https://doi.org/10.1038/cdd.2013.72

Yang, C., Li, J., Yu, L., Zhang, Z., Xu, F., Jiang, L., Zhou, X., & He, S. (2017, Oct 5). Regulation of RIP3 by the transcription factor Sp1 and the epigenetic regulator UHRF1 modulates cancer cell necroptosis. *Cell Death Dis, 8*(10), e3084. https://doi.org/10.1038/cddis.2017.483

Yang, Z., Xu, J., Li, L., Li, R., Wang, Y., Tian, Y., Guo, W., Wang, Z., Tan, F., Ying, J., Jiao, Y., Gao, S., Wang, J., Gao, Y., & He, J. (2020, Sep 28). Integrated molecular characterization reveals potential therapeutic strategies for pulmonary sarcomatoid carcinoma. *Nat Commun, 11*(1), 4878. https://doi.org/10.1038/s41467-020-18702-3

Yatim, N., Jusforgues-Saklani, H., Orozco, S., Schulz, O., Barreira da Silva, R., Reis e Sousa, C., Green, D. R., Oberst, A., & Albert, M. L. (2015, Oct 16). RIPK1 and NF-kappaB signaling in dying cells determines cross-priming of CD8(+) T cells. *Science, 350*(6258), 328-334. https://doi.org/10.1126/science.aad0395

Yun, C. H., Boggon, T. J., Li, Y., Woo, M. S., Greulich, H., Meyerson, M., & Eck, M. J. (2007, Mar). Structures of lung cancer-derived EGFR mutants and inhibitor complexes: mechanism of activation and insights into differential inhibitor sensitivity. *Cancer Cell, 11*(3), 217-227. https://doi.org/10.1016/j.ccr.2006.12.017

Zeelenberg, I. S., Ostrowski, M., Krumeich, S., Bobrie, A., Jancic, C., Boissonnas, A., Delcayre, A., Le Pecq, J. B., Combadiere, B., Amigorena, S., & Thery, C. (2008, Feb 15). Targeting tumor antigens to secreted membrane vesicles in vivo induces efficient antitumor immune responses. *Cancer Res, 68*(4), 1228-1235. https://doi.org/10.1158/0008-5472.CAN-07-3163

Zhang, B., Yao, G., Zhang, Y., Gao, J., Yang, B., Rao, Z., & Gao, J. (2011). M2-polarized tumor-associated macrophages are associated with poor prognoses resulting from accelerated lymphangiogenesis in lung adenocarcinoma. *Clinics (Sao Paulo), 66*(11), 1879-1886. https://doi.org/10.1590/s1807-59322011001100006

Zhang, L., Liu, S., Liu, H., Yang, C., Jiang, A., Wei, H., Sun, D., Cai, Z., & Zheng, Y. (2020, Jul). Versatile cationic liposomes for RIP3 overexpression in colon cancer therapy and RIP3 downregulation in acute pancreatitis therapy. *J Drug Target, 28*(6), 627-642. https://doi.org/10.1080/1061186X.2019.1708370

Zhao, Q., Guo, J., Cheng, X., Liao, Y., Bi, Y., Gong, Y., Zhang, X., Guo, Y., Wang, X., Yu, W., Jin, S., Tan, Y., & Yu, X. (2021). RIPK3 Suppresses the Progression of Spontaneous Intestinal Tumorigenesis. *Front Oncol, 11*, 664927. https://doi.org/10.3389/fonc.2021.664927

Zhao, Q., Yu, X., Zhang, H., Liu, Y., Zhang, X., Wu, X., Xie, Q., Li, M., Ying, H., & Zhang, H. (2017, Apr 25). RIPK3 Mediates Necroptosis during Embryonic Development and Postnatal Inflammation in Fadd-Deficient Mice. *Cell Rep, 19*(4), 798-808. https://doi.org/10.1016/j.celrep.2017.04.011

Zhou, C., Wu, Y. L., Chen, G., Feng, J., Liu, X. Q., Wang, C., Zhang, S., Wang, J., Zhou, S., Ren, S., Lu, S., Zhang, L., Hu, C., Hu, C., Luo, Y., Chen, L., Ye, M., Huang, J., Zhi, X., Zhang, Y., Xiu, Q., Ma, J., Zhang, L., & You, C. (2011, Aug). Erlotinib versus chemotherapy as first-line treatment for patients with advanced EGFR mutation-positive non-small-cell lung cancer (OPTIMAL, CTONG-0802): a multicentre, open-label, randomised, phase 3 study. *Lancet Oncol, 12*(8), 735-742. https://doi.org/10.1016/S1470-2045(11)70184-X

Zhu, J., Powis de Tenbossche, C. G., Cane, S., Colau, D., van Baren, N., Lurquin, C., Schmitt-Verhulst, A. M., Liljestrom, P., Uyttenhove, C., & Van den Eynde, B. J. (2017, Nov 10). Resistance to cancer immunotherapy mediated by apoptosis of tumor-infiltrating lymphocytes. *Nat Commun, 8*(1), 1404. https://doi.org/10.1038/s41467-017-00784-1

Zuccolo, J., Deng, L., Unruh, T. L., Sanyal, R., Bau, J. A., Storek, J., Demetrick, D. J., Luider, J. M., Auer-Grzesiak, I. A., Mansoor, A., & Deans, J. P. (2013). Expression of MS4A and TMEM176 Genes in Human B Lymphocytes. *Front Immunol, 4*, 195. https://doi.org/10.3389/fimmu.2013.00195

Publications

Original Publications

Deepti Agrawal, Michelle Dietzen, Fabian Allmendinger, Xin Wang, Magda Spella, Enkhtsetseg Munkhbaatar, Martina Anton, Eva C. Keller, Moritz Jesinghaus, Patrina S.P. Poh, Anna-Lena Meinhardt, Ulrike Höckendorf, Anne Jacob, Verena Haefner, Tobias Stoeger, Martijn van Griensven, Katja Steiger, Julia Slotta-Huspenina, Wilko Weichert, Georgios T. Stathopoulos, Adam Wahida, Nicholas McGranahan, Sebastian Vosberg, Philipp J. Jost
Aberrant methylation limits anit-tumoral inflammation in lung adenocarcinoma by restricting RIPK3 expression
(Manuscript submitted to Cancer Cell, 2022)

Oral presentations

F. Allmendinger, D. Agrawal, M. Dietzen, S. Vosberg, E. Munkhbaatar, N. McGranahan, P.J. Jost
RIPK3: A novel tumor suppressor in lung adenocarcinoma
Munich Medical Student Science Conference, Munich, Germany, 2021

F. Allmendinger, D. Agrawal, M. Dietzen, S. Vosberg, E. Munkhbaatar, N. McGranahan, P.J. Jost
RIPK3 dependent necroptosis acts as tumor suppressor in lung adenocarcinoma
5th MD-Symposium, German Cancer Aid, Bonn, Germany, 2021

F. Allmendinger, D. Agrawal, M. Dietzen, S. Vosberg, E. Munkhbaatar, N. McGranahan, P.J. Jost
RIPK3 downregulation in lung cancer alters the tumor immune microenvironment supporting tumor progression
Annual Meeting of the German, Austrian, and Swiss Society of Hematology and Oncology, Berlin, Germany, 2021

Poster presentations

F. Allmendinger, D. Agrawal, M. Dietzen, S. Vosberg, E. Munkhbaatar, N. McGranahan, P.J. Jost
Necroptosis establishes an inflammatory tumor immune microenvironment acting as tumor suppressor in lung adenocarcinoma
ESMO Congress 2021, Paris, France, 2021

Fabian Allmendinger, Deepti Agrawal, Michelle Dietzen, Enkhtsetseg Munkhbaatar, Nicholas McGranahan, Sebastian Vosberg, Philipp J. Jost
RIPK3 acts tumor suppressive in lung adenocarcinoma by facilitating a diverse immune environment
Annual Meeting of the German Society of internal medicine, Wiesbaden, Germany, 2022

Awards

Best Talk Award: Munich Medical Student Science Conference, Munich, Germany, 2021
Lecture Price: 5th MD-Symposium, German Cancer Aid, Bonn, Germany, 2021
Young Investigator Award: Annual Meeting of the German, Austrian, and Swiss Society of Hematology and Oncology, Berlin, Germany, 2021

Collaborations

Presented bioinformatic analysis were performed by Dr. Nicholas McGranahan and Dr. Michelle Dietzen form the UK Lung Cancer Center of Excellence, University College London (United Kingdom). Dr. Nicholas McGranahan and Dr. Michelle Dietzen kindly reviewed and agreed to include analyzed datasets and figures 5, 6 and 18 in this thesis as the result of our collaboration on elucidating the role RIPK3 dependent necroptosis in human LUAD samples received from The Cancer Genome Atlas Project (TCGA).

Acknowledgements

I want to thank Professor Florian Bassermann for allowing me to make my doctorate at his department for internal Medicine III: hematology and oncology, Klinikum rechts der Isar of the TU Munich.

Foremost, I would like to express my sincere thanks to Professor Philipp Jost for the great opportunity to make my doctorate in his laboratory of molecular oncology and cell death as well as offering me such an interesting research project. I am very grateful for all his exceptional support not only introducing me to the field of cancer science but moreover mentoring my early steps in the academic field.

Also, I want to express my gratitude and appreciation for Dr. Caterina Branca and Dr. Deepti Agrawal, who mentored my work in the laboratory and supported me throughout this doctoral thesis, as well as PD. Dr. Melissa Schlitter, who constantly supported me with great advice and assistance during this research project.

I want to thank Ulrike Höckendorf for her great support by performing FACS experiments and Dr. Nicholas McGranahan and Dr. Michelle Dietzen for performing bioinformatic analysis to calculate the presented immune scores.

I am grateful for the German Cancer Aid, providing me a scholarship for performing my doctoral thesis within the Mildred-Scheel Program.

Last but not least, I want to thank my family for all their endless support and time.